ALMA MATER STUDIORUM · UNIVERSITÀ DI BOLOGNA

**Scuola di Scienze**
**Dipartimento di Fisica e Astronomia**
**Corso di Laurea Magistrale in Fisica**

# Strangeness enhancement with multiplicity and effective energy in pp collisions at $\sqrt{s} = 13$ TeV with the ALICE detector at the LHC

**Relatore:**
**Prof.ssa Luisa Cifarelli**

**Correlatore:**
**Dott. Francesco Noferini**

**Presentata da:**
**Francesca Ercolessi**

Anno Accademico 2018/2019

## Sommario

L'esperimento ALICE nasce con lo scopo di studiare la materia nelle condizioni di energia estreme prodotte in collisioni tra ioni pesanti, alla ricerca di prove sperimentali del Quark Gluon Plasma (QGP). Tuttavia, negli ultimi anni, uno sguardo più attento alle interazioni tra adroni ha mostrato che anche eventi di collisione pp presentano caratteristiche simili a quelle tra ioni. Una di queste è l'aumento di stranezza, una delle prove sperimentali a favore dell'esistenza del QGP in collisioni A-A, che è stata recentemente osservata anche in collisioni pp ad alta molteplicità. Questa tesi presenta uno studio sull'aumento di stranezza in collisioni pp a $\sqrt{s} = 13$ TeV in funzione della molteplicità prodotta nello stato finale e dell'energia effettivamente disponibile per la produzione di particelle nella fase iniziale dell'interazione (energia effettiva). L'energia effettiva in collisioni tra protoni non coincide infatti con l'energia del centro di massa, ma risulta ridotta a causa del cosiddetto effetto *leading*. Data la correlazione, dimostrata sperimentalmente, tra molteplicità ed energia effettiva, l'aumento di stranezza osservato può essere relazionato ad un effetto di stato finale o ad un effetto di stato iniziale. Al fine di risolvere questa ambiguità, questa tesi introduce una variabile sperimentale che consente di stimare l'energia effettiva evento per evento, sfruttando le capacità dei calorimetri a zero gradi di ALICE. Ciò permette di studiare, per la prima volta, la dipendenza della produzione di particelle strane dall'energia effettiva. L'aumento di stranezza è inoltre analizzato in funzione della molteplicità, estendendo il range della ricerca a valori superiori rispetto ai precedenti risultati sperimentali. Una volta stabilita la dipendenza del fenomeno dalle due quantità, attraverso uno studio doppio-differenziale, questa tesi permette di concludere che l'aumento di stranezza osservato in collisioni pp è legato ad un effetto di stato finale.

**Abstract**

ALICE is a dedicated heavy-ion detector, located along the Large Hadron Collider (LHC) at CERN. It was built to focus on physics of strongly interacting matter at extreme energy densities, where the formation of a new phase of matter is expected: the Quark Gluon Plasma (QGP). However in the last years of LHC activity a deeper look into hadron interactions showed that also pp high-multiplicity events exhibit some features similar to Pb-Pb, opening new scenarios to search for medium effects in smaller systems. One of the first signatures of QGP was strangeness enhancement in A-A collisions, which consists in an increased production of strange hadrons in the interaction, which would be strongly suppressed in absence of plasma. This thesis presents a study on strangeness enhancement in pp collisions at $\sqrt{s} = 13$ TeV as a function of the charged particle multiplicity produced in the final state and of the energy effectively available for particle production in the initial phase of the interaction. The effective energy in pp collisions is smaller than the center of mass energy due to the so-called leading effect, related to the quantum number flow conservation. Given the strong relation between these two quantities the strangeness enhancement observed in pp may be related either to the initial phase of the collision or to a final state effect. This analysis introduces for the first time a variable which allows to estimate the effective energy event-by-event, exploiting the ability of ALICE Zero Degree Calorimeters to cover candidates of leading baryons. Through this estimator this thesis allows to study the dependence of the strange particles production on the effective energy, showing an enhanced trend in particular when increasing the strangeness content in baryon composition. The strangeness enhancement is also studied as a function of multiplicity and the increased center of mass energy selected for this analysis, with respect to previous results, makes possible to explore higher multiplicity values. This study confirms that the enhanced trend of strange particles production continues even at higher multiplicities, being compatible with the previous results in the respective multiplicity regions. Once established the dependence of this phenomenon with multiplicity and effective energy, through a double differential study this thesis allowed to conclude that the strangeness enhancement visible in pp interactions is related to a final state effect. Considering the correlation between the effective energy and the final charged particle multiplicity produced in the event, the observed increased strangeness production as a function of the available energy can be expected.

# Contents

# Introduction

ALICE (A Large Ion Collider Experiment) is one of the four main experiments born along the Large Hadron Collider (LHC) at CERN. It was built to exploit the unique physics potential of Pb-Pb interactions and aims to study the physics of strongly interacting matter at extreme energy densities, where the formation of a new phase of matter is expected: the Quark Gluon Plasma (QGP). The existence of such a phase and its properties are important issues in Quantum Cromo Dynamics (QCD) for the understanding of confinement and chiral symmetry restoration. One of the first signatures of QGP was strangeness enhancement in A-A collisions, which consists in an increased production of strange hadrons in the interaction. In absence of QGP strange quarks ($s$ and $\bar{s}$) production would be strongly suppressed due to their large mass, if compared with the lighter $u$ and $d$ quarks.

Besides focusing on heavy ion collisions, ALICE is also interested in studying pp interactions since the comparison between the two collision systems is crucial to distinguish QCD properties with and without medium effects. In a recent paper the ALICE Collaboration published some interesting results regarding strangeness production in pp and p-Pb collision systems at a center of mass energy ($\sqrt{s}$) of 7 TeV [1]. This work showed that in hadronic interactions strangeness production increases with the event multiplicity with a similar trend to Pb-Pb data, although in absence of possible QGP effects. The article opens a large discussion around the possible origin of this phenomenon and concludes that it must be related to the final system created in the collision, since the particle multiplicity dependence on the center of mass energy is characteristic of the final state of an interaction.

Nevertheless, in pp collisions the charged particle multiplicity at a fixed center of mass energy is observed to be systematically lower than what can be inferred for instance in $e^+e^-$ data at the same $\sqrt{s}$. In fact while in $e^+e^-$ interactions the energy available for particle production coincides with the center of mass energy, in pp collisions it is reduced

with respect to $\sqrt{s}$ due to the so-called leading effect. This phenomenon is related to the quantum number flow conservation and it consists in a high probability to emit a forward baryon with large longitudinal momentum along the direction of the beams, which carries away a fraction of the incident energy.

Many results from previous experiments show that if the leading effect is taken into account the effective energy available for particle production can be measured event-by-event and it is strongly correlated with event multiplicity. Given the strong relation between these two quantities it is not straightforward to conclude whether the strangeness enhancement observed is related to the initial phase of the collision, i.e. to the effective energy available, or to a final state effect, i.e. to the multiplicity of particles produced.

This thesis aims to resolve the ambiguity regarding the origin of the strangeness enhancement observed in [1] with an exploratory study on its dependence on both multiplicity and effective energy. To reach this goal it proposes a double-differential analysis studying the strange particles production in different effective energy and multiplicity ranges. In order to perform such a study it is necessary to estimate the effective energy event-by-event through the ALICE detector. The subdetectors able to cover the most forward rapidity particles, candidates for leading baryons, are the Zero Degree Calorimeters (ZDC), two for protons (ZP) and two for neutrons (ZN), placed along the beam direction. The analysis is performed on pp collision data at $\sqrt{s} = 13$ TeV collected in 2015, 2016, 2017 and 2018 with the ALICE experiment in which the run conditions were optimal for ZDC data taking. The full sample consists of 75 runs with a total of about $4.6 \cdot 10^8$ events.

This thesis is organized in four chapters, the first one is dedicated to the physics goals of the ALICE experiment, with particular interest in the strangeness enhancement as signature of QGP. The second one focuses on the concept of leading effect and effective energy, presenting some results from previous experiments on different observables which shed light on the role of this phenomenon in pp collisions. The third chapter presents a detailed description of the ALICE detector with particular emphasis on the Zero Degree Calorimeters, crucial elements in this analysis. The fourth and last chapter describes the analysis carried out in this thesis and presents the conclusions reached.

# Chapter 1

# The Quark-Gluon Plasma and heavy-ion collisions

The Standard Model (SM) is currently the most detailed description of the building blocks of our universe. This model describes matter in terms of fermions, particles with half-integer spin, and bosons, particles with integer spin. The fermion group contains six quarks, six leptons and their anti-particles. The bosons are the mediators of the fundamental forces: electromagnetic, weak and strong force. The strong force is responsible for binding the quarks inside the hadrons, a phenomenon called *confinement*, and is described by the Quantum Chromo Dynamics (QCD). At high temperature and energy density QCD predicts a phase transition from the hadronic matter, where quarks and gluons are confined inside hadrons, to a deconfined state of matter, the so-called Quark-Gluon Plasma (QGP). This QCD phase transition can be investigated in laboratory through ultra-relativistic heavy-ion collisions by reproducing the temperature, pressure and energy density conditions that lead to the QGP formation. The product of the collision is a "fireball" in local thermal equilibrium that rapidly expands and cools down. The development of the fireball produced in heavy-ion collisions is believed to reproduce the evolution stages of the early Universe, when the partonic deconfined matter turned into confined hadrons, nearly 1 $\mu s$ after the Big Bang. Because of this analogy, heavy-ion collisions are often referred to as the "Little Bang".

## 1.1 QCD

As briefly mentioned, Quantum Chromo Dynamics is a non-abelian gauge theory which describes the strong interaction, the force that acts between quarks and gluons within nuclei. QCD is based on the colour $SU(3)_c$ symmetry group and is formulated in terms of the Quark Model with colour interaction mediated by 8 massless coloured gauge bosons, the gluons. Quarks have colour charge, similar to the electrical charges in the lepton sector, which takes one of three values known as red, blue, and green (as well as anti-colours). In QCD the gauge bosons (gluons) carry colour and in particular are bi-coloured; therefore they can interact with each other via the strong interaction. Such a thing is prohibited, for instance, in Quantum Electrodynamics (QED), where the intermediary bosons, photons, do not carry electric charge and thus cannot interact. As a consequence the strong interactions not only have Feynman diagrams with quark loops, which lead to "charge screening", making the force weaker at large distances, but also gluon loops, which lead to "charge anti-screening", dominant in QCD, causing a stronger force at short distances. These diagrams are shown in Fig. 1.1.
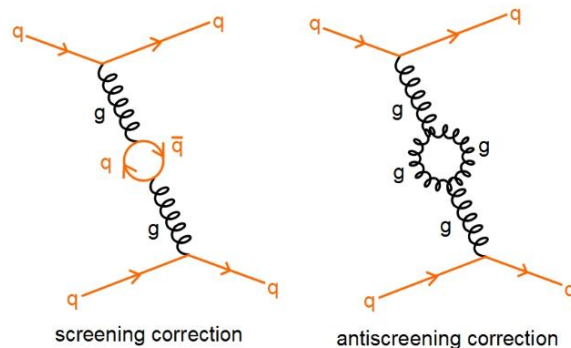


Figure 1.1: Feynman diagrams of the strong interaction with quark loops ("charge screening") and gluon loops ("charge anti-screening").

A fundamental consequence is that the QCD coupling constant $\alpha_S$ evolves with the transferred momentum $Q$ (running coupling constant). In particular at increasing $Q$, and decreasing distances, $\alpha_S$ asymptotically reaches 0 as shown in Fig. 1.2.

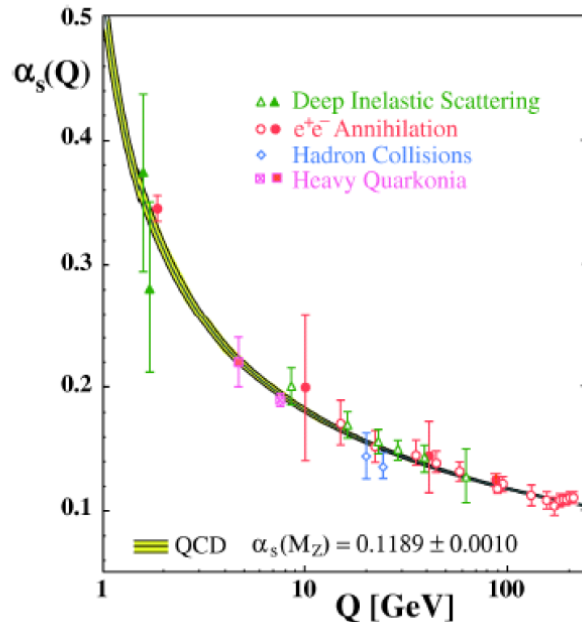$$\lim_{Q \to \infty} \alpha_S = 0 \tag{1.1}$$

4

Figure 1.2: Summary of the experimental values measured for the $\alpha_S$ coupling as a function of the process transferred momentum [2].

It is possible to distinguish two different regimes in the strong interaction, at large and at short distances, known respectively as confinement and asymptotic freedom. In the large momentum transfer region, the weak coupling allows to use perturbative methods to study QCD; however, perturbation theory cannot be used in the low-$Q$ regions, where the coupling becomes stronger. In this case the necessary tool to carry out such calculations is Lattice Quantum Chromodynamics (LQCD).

### 1.1.1 The QCD phase transition: QGP

Strongly interacting matter can exist in different phases characterized by given temperatures and densities, as summarised by the phase diagram of QCD as a function of temperature (T) and baryo-chemical potential[1] ($\mu_B$) in Fig. 1.3. As briefly mentioned, as a result of the running of the strong coupling, two regimes can be defined in the

---

[1]The baryo-chemical potential is defined as the energy needed to increase of one unity the total number of baryons in a system ($N_B$): $\mu_B = \partial E / \partial N_B$.

strong interaction: a large distance regime (low-$Q$) referred to as confinement, and a short distance regime (high-$Q$) called asymptotic freedom.
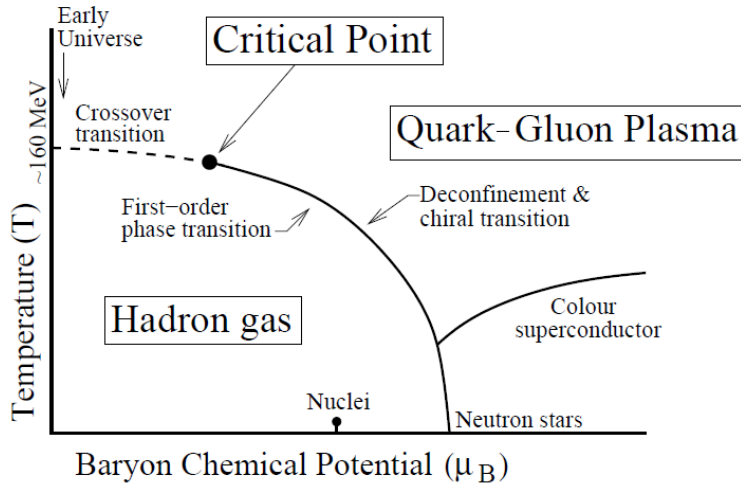


Figure 1.3: QCD phase diagram.

The core concept of asymptotic freedom is that the interaction strength of the strong force drops in the region of high momentum transfer (or at very small distances) and therefore at very high energy densities, the colour force acting between quarks and gluons should become weak enough to form a weakly interacting gas. Instead of the usual quark confinement, one could expect a new state of matter consisting of deconfined quarks and gluons, called Quark-Gluon Plasma (QGP).

In order to describe this phase transition, one could consider a simplified thermodynamical approach based on the so-called *bag model*, a theory describing confinement which compares partons inside hadrons as trapped objects inside a bag. Using this approach it is possible to analise the QCD phase diagram as a function of temperature and baryo-chemical potential shown in Fig. 1.3. Low temperatures and low baryo-chemical potential values in the diagram correspond to the ordinary nuclear matter. By moving towards higher temperature the diagram reaches a phase of hadronic gas (HG) where nucleons interact and form hadrons. The deconfined phase of Quark-Gluon Plasma is reached by further increasing temperature and energy density. During the hadronic

phase the pressure of the hadron gas can be written using the Stefan-Boltzmann law as a function of the temperature $T$:

$$P_H = d_H \frac{\pi^2}{90} T^4$$

where $d_H$ is a factor that accounts for the degeneration of the system degrees of freedom. In the deconfined Quark Gluon Plasma phase, the pressure is given by:

$$P_{QGP} = d_{QGP} \frac{\pi^2}{90} T^4 - B$$

where $d_{QGP}$ is the degeneration factor of QGP and $B$ is called *bag constant*. Knowing these constants it is possible to obtain the critical temperature $T_c$ at which the transformation takes place with the condition $\mu_B = 0$ by requiring

$$P_{QGP} = P_H,$$

which leads to:

$$T_c^4 = \frac{90}{\pi^2} \frac{B}{d_{QGP} - d_H}.$$

Using the value $B^{1/4} \sim 220$ MeV [5], a first estimate of $T_c$ is:

$$T_c \sim 160 \text{ MeV [5]}.$$

Even though quite accurate, this approach is still simplified and as already mentioned, in the short distance regime, the best tool to perform such calculations is Lattice Quantum Chromodynamics (LQCD). Lattice QCD calculations predict that the critical temperature at which a transition from hadronic gas to QGP can occur is $T_c \sim 175$ MeV, corresponding to a critical energy density epsilon $\varepsilon \sim (0.3\text{-}1.3)$ MeV/fm$^3$ [4].

Besides the macroscopic (thermodynamical) approach, the phase transition can also be characterized at the microscopic level by changes in the symmetry of the system. A crucial role in this case is made by chiral symmetry, which is a symmetry of QCD in the limit of vanishing quark masses. However, it is known that current quark masses are finite, even though small compared with the hadronic scales in the case of the two lightest quarks, up and down. The chiral symmetry breaking due to the finite light quarks

masses is the responsible for the non zero mass of pions (Goldstone bosons for this symmetry). Chiral symmetry breaking is most apparent in the mass generation of nucleons from elementary light quarks, accounting for approximately 99% of their combined mass as baryons. In particular in the transition between the hadronic phase of matter and the deconfined state of plasma, the chiral symmetry should be restored. As quarks become deconfined, the light quark masses go back to their bare values, an effect usually referred to as "partial restoration of chiral symmetry" [3].

## 1.2  Heavy-ion collisions

The formation of the Quark-Gluon Plasma can be investigated in laboratory through ultra-relativistic heavy-ion collisions. Such relativistic nuclei are Lorentz contracted while travelling along the beam axis and therefore their transverse dimension is larger than their longitudinal dimension, so that their collision can be considered as the superposition of binary nucleon-nucleon collisions. The energy carried by the individual nucleons is deposited within a very small region in space and short duration of time. By generating in the collision such an incredibly hot and dense "fireball" of fundamental particles, the conditions for the formation of Quark-Gluon Plasma can be reached. A schematic picture of a heavy-ion collision is shown in Fig. 1.4.
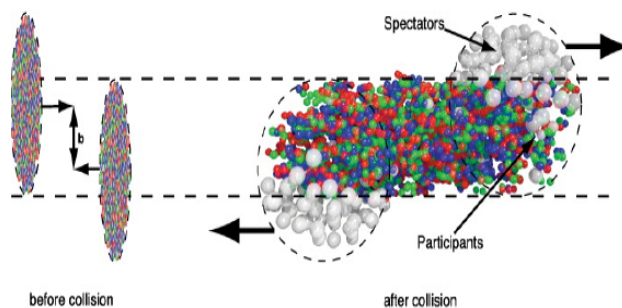


Figure 1.4: Representation of an ultra-relativistic heavy ions collision. The two nuclei are Lorentz contracted before the collision. After the collision, a region containing the participating nucleons with high temperature and density is created (fireball), while the spectators continue their motion in the beam direction.

8

Since nuclei are extended objects, the volume of the interacting region depends on the impact parameter ($b$) of the collision, defined as the distance between the centers of the two colliding nuclei in the plane transverse to the beam axis. It is customary in the field of heavy-ion physics to introduce the concept of the centrality of the collision, which is directly related to the impact parameter. In the so-called central collisions, the two nuclei collide almost head-on and almost all nucleons within the nucleus participate in the collision. This kind of collision is characterized by a small impact parameter and the largest particle multiplicity production. On the contrary, a peripheral collision has large impact parameter and only few nucleons participate in the collision. The nucleons that participate in the collision are called "participants" while those that do not interact are called "spectators". Centrality is usually measured in two main ways:

- from the number of charged particles produced in the collision (average charged-particle multiplicity $N_{ch}$);

- from the number of spectator nucleons that are not involved in the collision.

In fact, neither the impact parameter nor geometrical quantities, such as the number of participants and spectators, $N_{part}$ and $N_{spec} = 2A - N_{part}$, where $A$ is the mass number, and the number of binary collisions $N_{coll}$, are directly measurable. The two experimental observables related to the collision geometry are the average charged-particle multiplicity $N_{ch}$ and the energy carried by particles close to the beam direction. The average charged-particle multiplicity is assumed to decrease monotonically with increasing impact parameter, while the monotonic relationship between the energy deposit in the forward region and $b$ is valid only for relatively central events (small $b$).

The first method used to measure the centrality of the collision relies on the choice of a geometrical model for the hadronic processes. The purely geometrical Glauber model [7], which is typically used in this context, treats a nuclear collision as a superposition of binary nucleon-nucleon interactions. The second method exploits the energy measurement of the spectator nucleons in the forward region. Commonly in ALICE, centrality classes are defined in terms of percentiles of the nucleus-nucleus hadronic cross section [6]. When measuring particle production in the final state of the collision, the definition of

rapidity and pseudorapidity variables is crucial. The rapidity is defined as:

$$y = \frac{1}{2} \ln \left( \frac{E + p_L}{E - p_L} \right)$$

where $E$ represents the energy and $p_L$ the longitudinal momentum component. In the ultrarelativistic limit rapidity may be approximated by pseudorapidity, which is defined as:

$$\eta = \frac{1}{2} \ln \left( \frac{p + p_L}{p - p_L} \right) = -\ln \left( \tan \left( \frac{\theta}{2} \right) \right)$$

where $\theta$ is the angle between the momentum of the particle and the beam axis.

## 1.2.1   Time evolution

The evolution of the strong interacting system created when two ultrarelativistic atomic nuclei collide and the characterisation of its properties in the different phases is one of the main goal of heavy ion experiments. Figure 1.5 summarises the current knowledge of the key phases of relativistic heavy ion collisions, which include:

- *Pre-equilibrium*
  In the early collision stages, hard processes occur between partons, and particles with either a large mass or large transverse momenta are created. This process involves large momentum transfer $Q$ and therefore the production of these particles can be calculated with perturbative QCD. Moreover this phase expects production of direct photons, real or virtual. Since direct photons are generated in this first stage of the interaction, they can be used to reconstruct the momentum distribution of the quarks from which they were produced, although to decouple them from the other photons produced in the later stages of the collision may be quite difficult. The typical time scale for such processes is 0.1 fm/$c$.

- *Thermalization, expansion and hadronization*
  The particles produced in the primary collisions continue to mutually interact, giving rise to a region of high matter and energy density at the thermal equilibrium from which the QGP can be produced in less than 0.1-0.3 fm/$c$. This stage is referred to as *thermalization*.
  The relative abundance of gluons, up, down and strange quarks changes in this

phase. In particular, due to chiral symmetry restoration at QGP formation energies, the strange quark mass reduces to its running mass ($m_s \sim 104$ MeV/$c^2$), which is smaller compared to its constituent mass $m_s \sim 450$ MeV/$c^2$. As a consequence the production of strange hadrons in heavy-ion collisions should increase with respect to proton-proton interactions. At this stage, due to the internal pressure, the thermalized system expands and the energy density decreases. The rapid expansion of the QGP is usually modelled using the relativistic hydrodynamics [8] which provides useful insights to interpret the experimental data.



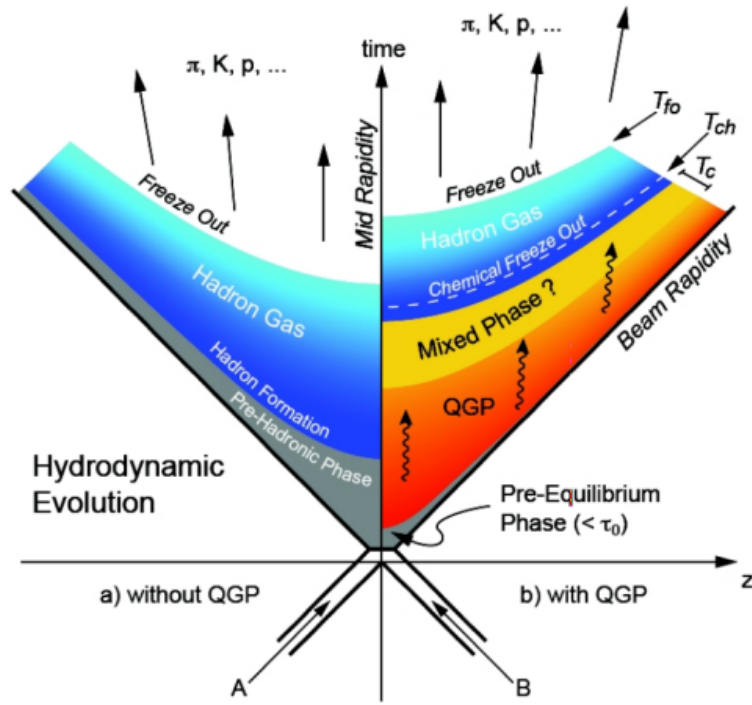Figure 1.5: Schematic view of the time evolution of A-A collisions.

When the critical density between the two phases is reached ($\varepsilon_c \sim 1$ GeV/fm$^3$), hadronization starts and the system gradually evolves into an interacting hadron resonance gas. In this phase, the expansion and contextual cooling of the system continue, as well as the elastic and inelastic interactions among the hadrons within the system.

- *Chemical and kinetical freeze-out*
  The relative abundance of hadron species can change until the hadron gas is able to interact inelastically. When the energy of the collisions becomes too small the abundances are fixed and the so-called chemical freeze-out is reached. At this stage elastic interactions are still present and continue to modify the kinetic properties of the hadrons. When the distances between hadrons are larger than the range of the interaction, elastic collisions stop and the so-called kinetical freeze-out is reached. At this stage also the kinematical distributions of the hadrons are fixed.

## 1.2.2 Experimental aspects of heavy-ion collisions

Since the QGP produced in heavy-ion collisions lasts for $\sim 10$ fm/$c$, or $\sim 10^{-23}$ s, it can not be studied directly. Therefore, theoretical models predict some properties of the final state of the collision which can be studied as signatures of the production of the Quark-Gluon Plasma. Depending on the phase of the collision in which they are produced, these signatures are referred to as hard and soft probes. The former are signals produced in the first stages of the collision by the interaction of high momentum partons, while the latter are produced in the later stages of the collision and keep indirect information on the properties of the phase transition.

The purpose of this section is not to give a detailed description of the all QGP signatures but just to report about the most recent results obtained by the ALICE experiment.

**Charged-particle multiplicity density**

Global observables, such as the charged-particle multiplicity, are crucial properties in heavy-ion collisions being related to the initial geometry and energy density produced in the interaction. The dependence of the charged-particle multiplicity (or pseudorapidity density) $dN_{ch}/d\eta$ on energy and system size, reflects the interplay between parton-parton scattering processes for particle production.

Over the last years, the ALICE Collaboration has provided results of charged-particle production in various collision energies and systems. Previous measurements of $dN_{ch}/d\eta$ for A-A collisions were also performed at the LHC by ATLAS [9], and CMS [10] at $\sqrt{s_{NN}}$ = 2.76 TeV, and at lower energies (in the range $\sqrt{s_{NN}}$ = 9-200 GeV) by experiments at the Super Proton Synchrotron (SPS) and Relativistic Heavy Ion Collider (RHIC) [11]. All the results show an increase of charged multiplicity with energy steeper in A-A

compared to pp collisions. Measurements of charged particle multiplicity density as a function energy $\sqrt{s_{NN}}$ and number of participants collected by different experiments for Pb-Pb and Au-Au are shown in Fig.1.6 (a). The value of $\frac{2}{<N_{part}>} < dN_{ch}/d\eta >$ shown in
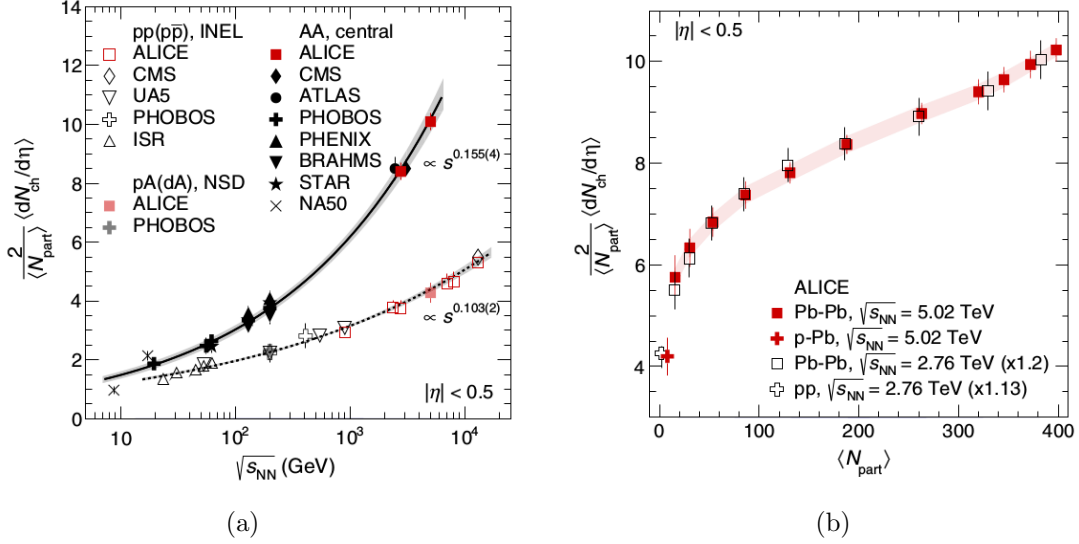


Figure 1.6: (a) Charged particle multiplicity density as a function of energy $\sqrt{s_{NN}}$ collected by different experiments for Pb-Pb and Au-Au collisions. Measurements of inelastic pp and $p\bar{p}$ collisions are also shown along with those from nonsingle diffractive p-A and d-A collisions. The dependence of the charged multiplicity on the center of mass energy is fitted with a power law [12]. (b) Charged particle multiplicity density as a function of the mean number of participants $< N_{part} >$ in pp, p-Pb, Pb-Pb collisions, measured by ALICE [12].

Fig. 1.6 (a) is increasing with rising energy and number of participants. Measurements of inelastic pp and $p\bar{p}$ collisions are also shown along with those from non-single diffractive p-A and d-A collisions. The dependence of the charged multiplicity with the center of mass energy is fitted with a power law as $as^b$ and the fitting parameters are plotted with their uncertainties shown as shaded bands. The centrality dependence of $\frac{2}{<N_{part}>} < dN_{ch}/d\eta >$ for for Pb-Pb collisions at $\sqrt{s_{NN}} = 5.02$ TeV is shown in Fig.1.6 (b). The data are plotted as a function of $< N_{part} >$ and a strong dependence is observed, with the charged multiplicity decreasing by a factor of $\sim 1.8$ from the most central collisions. Results from non-single diffractive p-Pb collisions at the same center of mass energy and data from lower-energy (2.76 TeV) Pb-Pb and pp collisions are also shown for comparison [12].

### $p_\mathrm{T}$ spectra and particles ratios

The energies available at the LHC open up the possibility for detailed measurements in a wide $p_\mathrm{T}$ range. In particular low momentum hadrons, usually defined *soft hadrons*, represent the majority of the particles produced in a heavy ion collision ($\sim 95\%$ for $p_\mathrm{T} < 1.5$ GeV/$c$). The study of the low momentum spectra of identified particles gives important insights about the characteristics of the medium at the kinetic freeze-out, while the study of high momentum spectra can give important hints on production processes in the early stages of the collision and the propagation of particles in the QGP. The RHIC experiments reported that hadron production at high transverse momentum in central Au-Au collisions is suppressed compared to the expectations from an independent superposition of nucleon-nucleon collisions. The dominant production process for high $p_\mathrm{T}$ hadrons is the fragmentation of high $p_\mathrm{T}$ partons that originate in hard scattering in the early stage of the nuclear collision. Therefore, the observed suppression at RHIC is generally attributed to the energy loss of the partons as they propagate through the QGP. To quantify this effect, the so-called nuclear modification factor $R_{AA}$ is used. It is defined as the ratio of the charged particle yield in Pb-Pb to that observed in pp collisions, scaled by the number of binary nucleon-nucleon collisions $< N_{coll} >$:

$$R_{AA} = \frac{\left(\frac{d^3N}{dp^3}\right)_{AA}}{\left(\frac{d^3N}{dp^3}\right)_{pp} < N_{coll} >} \quad .$$

If no production of QGP is expected, $R_{AA}$ should tend to unity. Figure 1.7 shows the nuclear modification factors $R_{p-Pb}$ and $R_{A-A}$ as a function of tranverse momentum. The nuclear modification factor in p-Pb collisions is consistent with unity at high $p_\mathrm{T}$, showing that the strong suppression observed in Pb-Pb is due to final state partonic energy loss in the hot and dense QGP created in Pb-Pb collisions. This suppression is weak in peripheral collisions and increases with centrality indicating an increasing parton energy loss with centrality [13].

### Elliptic flow

When two nuclei collide with a non-zero impact parameter (non-central collisions), the overlapping region is asymmetrical and this can produce anisotropies in particle emis-
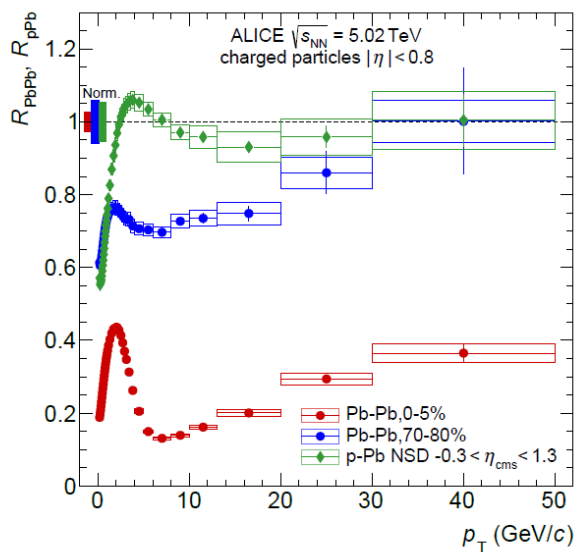
Figure 1.7: Nuclear modification factors measured by ALICE in central (0-5%) and peripheral (70-80%) Pb–Pb collisions and in p–Pb collisions at $\sqrt{s_{NN}} = 5.02$ TeV [13].

sion and momentum distribution. Since these anisotropies are generated before matter reaches the critical temperature and the hadronization phase, the elliptic flow is sensitive to the early and hot strongly interacting phase of the evolution of Quark-Gluon Plasma. The final azimuthal distribution of emitted particles can be written in terms of the azimuthal Fourier coefficients of the transverse momentum spectrum:

$$E\frac{d^3N}{d^3p} = \frac{d^3N}{p_T dp_T dy d\phi} = \frac{d^2N}{p_T dp_T dy}\frac{1}{2\pi}\left[1 + \sum_{n=1}^{\infty} 2\upsilon_n \cos n(\phi - \Phi_R)\right], \qquad (1.2)$$

where $p_T$ is the tranverse momentum, $y$ the rapidity, $\phi$ the azimuthal angle of the particle momentum and $\Phi_R$ the angle of the reaction plane, known using the tranverse distribution of particles in the final state. The coefficients $\upsilon_n$ are in general $p_T$ and $y$ dependent and are referred to as differential flow. In particular the first coefficient $\upsilon_1$ is called direct flow. In a central collision (zero impact parameter) the final azimuthal distribution is isotropic and therefore the coefficient $\upsilon_n$ are equal to zero. In a non central collision the typical almond shape of the overlap region between the colliding nuclei generates a pressure gradient along the reaction plane. This collective motion is called elliptic flow and it contributes to the $\upsilon_2$ coefficient of Eq.(1.2). Thus the measurements of these

$v_n$ coefficients is extremely important since they are related with the initial geometric condition and inhomogeneities through the properties of the medium. Figure 1.8 shows the $v_n$ coefficients measured by the ALICE experiment at different energies in Pb-Pb collisions. The value are compared with hydrodynamical models, which combine the initial spatial anisotropy and the hydrodynamical response [14].
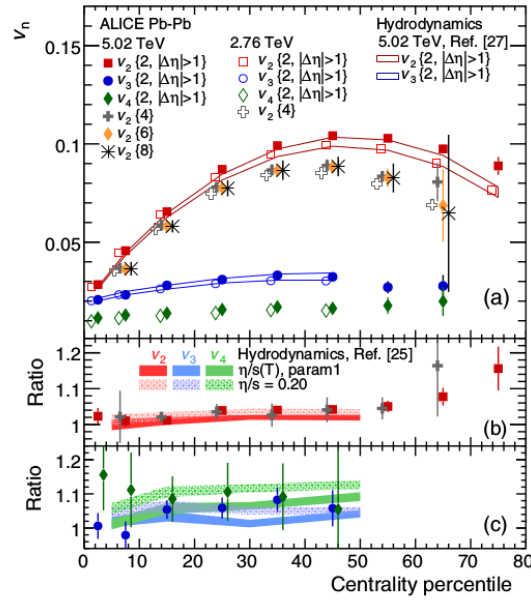


Figure 1.8: Panel (a): $v_n$ coefficients up to fourth order measured by the ALICE experiment at different energies as a function of the centrality percentile [14]. Panels (b) and (c): ratios between the measurements at 5.02 TeV and those at 2.76 TeV show good agreement with the unity. This suggests that the medium characteristics and the thermalisation dynamics do not change between the two energies [14].

### 1.2.3  Strangeness enhancement

In the Standard Model, quarks, the building blocks of hadrons, are classified in six types: down (d), up (u), strange (s), charm (c), bottom (or beauty, b) and top (t). The first three are known as "light quarks", while the latter three are called "heavy quarks". Fig. 1.9 shows a summary of quarks properties. Each elementary particle is described by a set of quantum numbers such as mass, spin, hypercharge, baryon number, strangeness etc...

Figure 1.9: Quarks in the Standard Model.

Among quantum numbers, the so-called strangeness of a particle is defined as:

$$S = -(n_s - n_{\bar{s}}) \tag{1.3}$$

where $n_s$ represents the number of strange quarks ($s$) and $n_{\bar{s}}$ represents the number of strange antiquarks ($\bar{s}$) present in the particle. Therefore, among the six flavors of quarks, only the strange quark has a nonzero strangeness, in particular -1 for $s$ and +1 for $\bar{s}$.

This quantum number was postulated in 1953, by M. Gell-Mann, T. Nakano and K. Nishijima, each working independently and the next year was clearly demonstrated experimentally. Strangeness is conserved in strong and electromagnetic interactions, but not in the weak ones. Consequently, the lightest particles containing a strange quark cannot decay by the strong interaction, and must instead decay via the much slower weak interaction. In most cases these decays change the value of the strangeness by one unit.

Among the hadrons, a special family of particles which contain at least one strange quark but not heavier quarks (like charm or bottom), are called hyperons. These are: the $\Lambda$(uds), the triplet $\Sigma^+$(uus), $\Sigma^0$(uds), $\Sigma^-$(dds), the doublet $\Xi^-$(dss), $\Xi^0$(uss) and the $\Omega$(sss), and the corresponding antiparticles. $\Xi$ and $\Omega$ are the only hyperons containing more than one strange quark and therefore are called multi-strange baryons.

In the following section, a general overview of the crucial role of the strange quark within the QGP study in heavy-ion collisions is given. First of all, unlike up and down, strange quarks are not present as valence quarks in the initial state and they need to be produced during the collision. Therefore the s quark plays an interesting role in the study of particle production. Other observations can be made looking at the bare mass of the

quarks, reported in Fig. 1.9. As can be seen, the strange is the third lightest quark, with a mass value that is half-way between the two lighter and the three heavier quarks. This means a relatively low production energy cost, which ensures an abundant production of strange hadrons among the produced particles.

**Strangeness as a signature of QGP**

Strangeness is of great interest in the context of QGP since 1982, when Johann Rafelski and Berndt Müller [15] suggested an increased production of strange hadrons as a possible signature for the formation of QGP in a heavy-ion collision. At a fixed collision energy, the production mechanisms of the strange quark is different within pp and A-A colliding systems. The former produces a Hadron Gas (HG), where the degrees of freedom are the hadronic ones, as quarks and gluons are confined. The latter forms the QGP, where the degrees of freedom are at partonic level, with free quarks and gluons. The energy needed to produce strange mesons or baryons in a thermally equilibrated HG is significantly higher than in the case of a QGP.

The great abundance of pions in the HG suggests to consider the production of strange particles from reaction between these light mesons. Direct production ($\pi + \pi \to \pi + \pi +$ strange hadron + antiparticle) is penalized because of the strange number conservation, which would require to produce strange particles and antiparticles jointly. In this case the reaction threshold corresponds to two times the rest mass of the strange hadrons. On the other hand, indirect production mechanisms have lower thresholds, but are still quite penalized. In this case, one would have two reactions in a sequence, starting with the production of lighter hadrons ($\pi + N \to K + \Lambda$) followed by a reaction of these intermediate products to produce the heavier hadrons.

In the case of production of QGP, the strangeness conservation needs to be satisfied only globally and the high gluon density allows to have new dominant production mechanisms such as gluon fusion processes. In the early stages of high-energy heavy-ions collisions, strangeness is produced in hard partonic scattering processes by flavour creation ($gg \to s\bar{s}$, $q\bar{q} \to s\bar{s}$) and flavour excitation ($gs \to gs$, $qs \to qs$). Strangeness is also created during the partonic evolution via gluon splittings ($g \to s\bar{s}$). The Feynman diagrams corresponding to the dominant strangeness production processes are shown in Fig. 1.10. In these reactions the energy threshold for the production of a $s\bar{s}$ pair reduces from twice the mass of the constituent strange quark ($\sim 900$ MeV) to twice the intrinsic mass of

the quarks ($\sim 300$ MeV), due to the partial chiral symmetry restoration [16].



Figure 1.10: Feynman diagrams for production of strange quarks in the QGP.

Therefore production of multi-strange hadrons in HG would be much more difficult than in the QGP. The signature of the formation of QGP proposed by Rafelski and Muller, known as strangeness enhancement, lies exactly on the overabundance of strangeness production in a QGP scenario (A–A collisions) with respect to a HG scenario (pp collisions).

**ALICE recent results on strangeness enhancement**

During the years, strangeness enhancement as a signature of the QGP was observed at SPS [17], RHIC [18] and LHC [19]. This effect has been found to increase with centrality and strangeness content of the hadron and decrease with the energy of the colliding system. At SPS and RHIC the strangeness enhancement was studied by measuring the ratio of the yield in AA collisions and the yield in pp collision at the same energy, normalized to the number of participants nucleons. Nevertheless the charged-particles multiplicity does not scale linearly with the number of participants and therefore this method is not ideal. A better observable would be the ratio of the yield of the studied particle to the pion yield.

ALICE has measured hyperons in different collision systems (pp, p-Pb and Pb-Pb) to investigate the production mechanism as a function of the system size. Strange and multi-strange hadrons are reconstructed via their characteristic weak decay topologies, decaying into two and three charged particles. Charged particle tracks are reconstructed and combined in an invariant mass analysis to reconstruct weak decay candidates which are required to fulfil selection criteria based on geometric (topological) and kinematic quantities. Figure 1.11 shows the ratio of the yield of strange particles to the pion yield. One can observe a smooth evolution across different colliding systems (pp, p-Pb and Pb-Pb) and no significant dependence on collision energy. For single-strange particles ($K_S^0$

and $\Lambda$), there is an indication of an increasing trend with increasing multiplicity in small systems, while for multi-strange particles ($\Xi$ and $\Omega$), the increase is significant. Figure 1.11 shows that the predictions of statistical hadronization models using a chemical freezeout temperature of 156 MeV are comparable with the measured values in Pb-Pb collisions. In this statistical picture, the lower production of strangeness in small systems (pp collisions) is the consequence of the small phase-space volume available (HG).

An example of measurement of transverse momentum spectra for $K^0_S$ and $\Lambda$ is shown in Fig. 1.13. For all particles considered, going from peripheral to central collisions, a more steep spectral shape is observed. The hardening is more pronounced for heavier particles. This behaviour is also consistent with similar observations for other light-flavour hadrons [20].
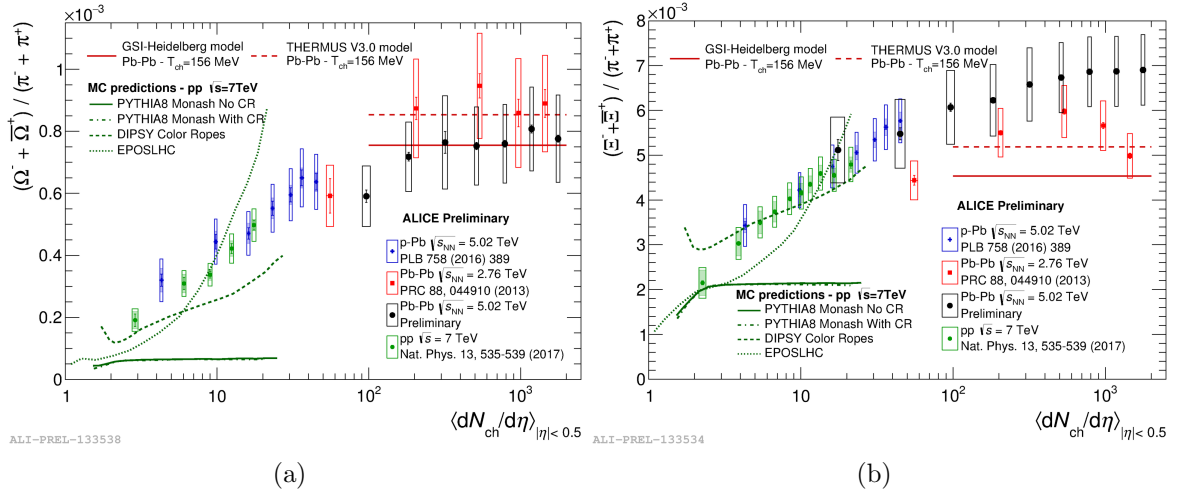


(a)                                                       (b)

Figure 1.11: Ratio of $\Xi$ and $\Omega$ yields to pion yield as a function of charged particle multiplicity density at mid pseudo-rapidity. Data from pp collisions at 7 TeV (small circles), p-Pb collisions at 5.02 TeV (crosses), Pb-Pb collisions at 2.76 TeV (squares), Pb-Pb collisions at 5.02 TeV (big circles) and comparisons to statistical hadronization models are shown. The open boxes represent the total systematic uncertainties and the shaded boxes show the component of the systematic uncertainties that is uncorrelated over multiplicity [20].
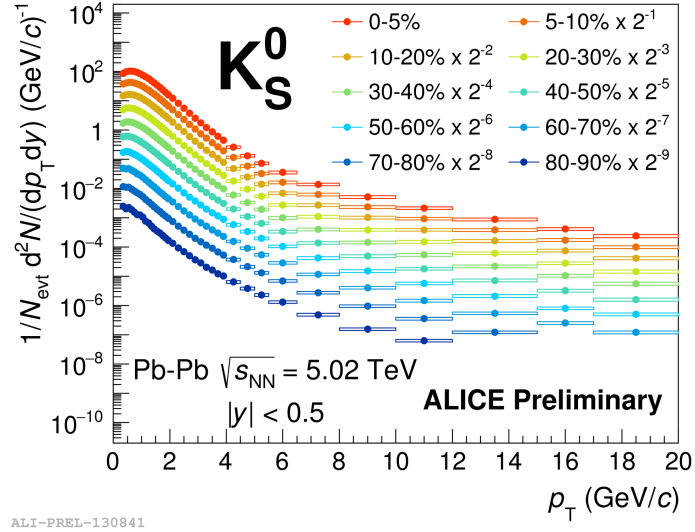
Figure 1.12: Transverse momentum spectra of $K^0_S$ for different centrality intervals in Pb-Pb collisions at $\sqrt{s_{NN}} = 5.02$ TeV [20].
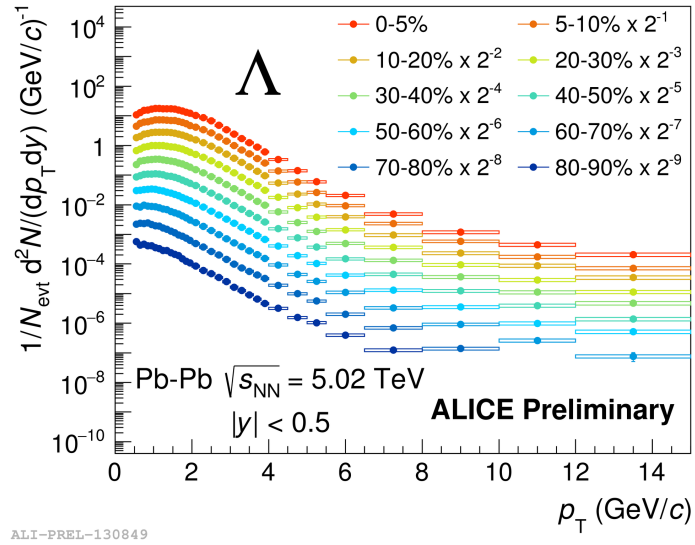


Figure 1.13: Transverse momentum spectra of $\Lambda$ for different centrality intervals in Pb-Pb collisions at $\sqrt{s_{NN}} = 5.02$ TeV [20].

# Chapter 2

# Multiplicity Studies and Effective Energy

As already mentioned in the previous chapter, ALICE was built to focus on physics of strongly interacting matter at extreme energy densities, where the formation of QGP is expected. To reach such conditions, ALICE exploits the unique physics potential of heavy-ion collisions (A-A) at very high energies, using Pb ions. This collision system releases a high amount of energy in a volume of thousands fm$^3$, reaching particle multiplicities much larger than in pp interactions. However, in the last years of LHC activity a deeper look into hadron interactions showed that also p-Pb and high-multiplicity pp events exhibit some features similar to that of Pb-Pb, opening new scenarios to search for medium effects in smaller systems. The understanding of particle production in pp interactions is one the key ingredient to separate genuine QGP signatures from cold nuclear matter effects in Pb-Pb, but it is also interesting on its own when looking at possible hints for medium effects in small systems.

## 2.1 Multiplicity in pp collisions

Global observables such as the charged particle multiplicity are of crucial relevance in high-energy particle collisions, being characteristic of the final state of the interaction but also related to the initial geometry and energy density produced in the collision. These observables provide important information on the dynamics of the interaction, in particular the dependence of the charged particle multiplicity $\mathrm{d}N_{ch}/\mathrm{d}\eta$ on energy and

system size reflects the interplay between parton-parton scattering processes for particle production.

The average charged particle multiplicity has been measured in many different collision systems (e$^+$e$^-$, pp (p$\bar{\text{p}}$), A-A collisions etc.) and over a wide range of center of mass energies. In fact the study of analogies and differences between multiparticle hadronic states produced in different collision systems is of crucial importance for understanding the underlying dynamics of particle production in these interactions. At first sight there is no universality in the final state hadrons produced in various high energy collision systems at fixed center-of-mass energy. In particular, it does make a difference if the reaction involves in the initial state just leptons (for instance e$^+$e$^-$) or two hadrons (for instance pp) suggesting the possibility of a different multiparticle production mechanism in the two interacting systems. For a long time this difference was attributed to the nature of the interaction, strong in the case of pp and electromagnetic in e$^+$e$^-$. These differences can be found in various properties such as charged-particle multiplicity, longitudinal and transverse momentum distributions, the ratio of "charged" to total energy of the multiparticle hadronic system produced, the event planarity etc. Among these, the most popular one is the average number of charged particles, being the most surprising effect of all. Along the years some very interesting results regarding this problem were obtained by a Collaboration including the University of Bologna, CERN and LNF (National Laboratory of Frascati) (which will be referred to as BCF Collaboration) working on data collected at the CERN ISR (Intersecting Storage Rings)[1] collider using a large volume magnet, the so-called Split Field Magnet (SFM)[2]. The main goal was to establish the similarities and the differences between pp and e$^+$e$^-$ colliding systems and to evaluate for each pp interaction the correct energy available for particle production [21].

### 2.1.1 Results from previous experiments

The average charged particle multiplicity in pure electromagnetic interactions has been studied over the years by many experiments exploiting e$^+$e$^-$ collisions, reaching a large energy interval until the highest energies at LEP [22, 29] and DESY (Deutsches Elektronen-

---

[1]The ISR was the world's first hadron collider, running at CERN from 1971 to 1984. The maximum center of mass energy reached was 62 GeV.

[2]The Split Field Magnet (SFM) was the largest spectrometer for particles from beam-beam collisions in the ISR. It could determine particle momenta in a large solid angle, but was designed mainly for the analysis of forward travelling particles.

Synchrotron) [30]. The high cross section for annihilation processes of e$^+$e$^-$ interactions makes it possible to study global observables in events where the energy available for particle production is the total center-of-mass energy $\sqrt{s}$. It is known that the average charged multiplicity in e$^+$e$^-$ collisions follows a logarithmic dependence on the center-of-mass energy $\sqrt{s}$, as shown in Fig. 2.1 by the results collected at DESY by different experiments. However when considering pp collision systems, many results show that the average charged multiplicity is characterized by a significantly different dependence and in particular is observed to be systematically lower than e$^+$e$^-$ [31, 35]. This behaviour is shown in Fig. 2.2 with a collection of measures from different experiments of the average charged multiplicity in e$^+$e$^-$ (full black symbols) and pp($\bar{\text{p}}$) (open symbols) collision systems.
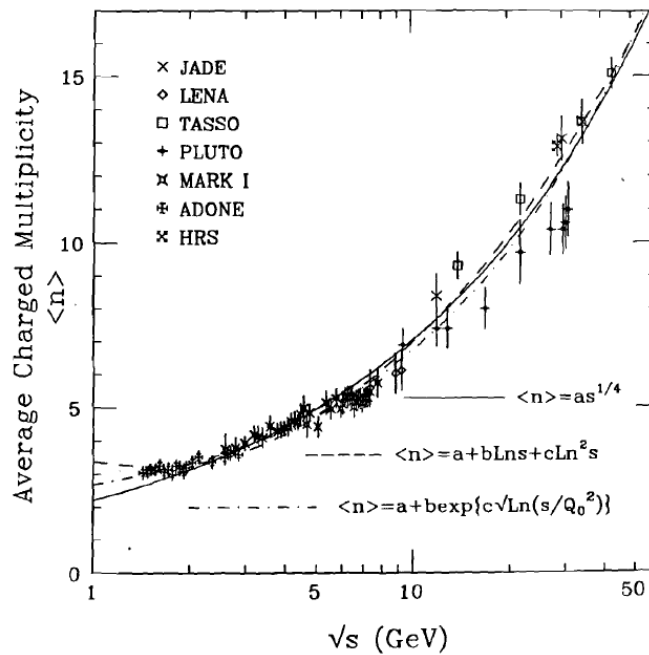


Figure 2.1: The average charged multiplicity as a function of center-of-mass energy from different experiments at DESY [30].

As already mentioned, some interesting results regarding this problem were obtained at ISR for different collision energies, $(\sqrt{s})_{pp} = 30,\ 33,\ 62$ GeV, by the BCF group [36, 39]. The key point of their analysis was to explain this behaviour considering that, while in $e^+e^-$ collisions the energy available for particle production coincides with the full center-of-mass energy, in $pp(\bar{p})$ collisions this energy is reduced with respect to $\sqrt{s}$ due to the so-called "leading effect".
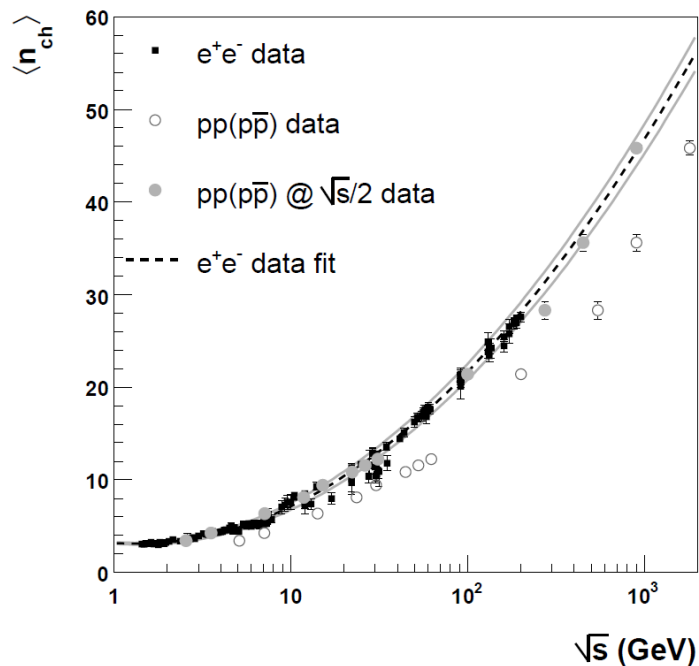


Figure 2.2: Average charged particle multiplicity measured in $e^+e^-$ (full black symbols) and pp(p) (open symbols) collisions. A logarithmic fit to the $e^+e^-$ data is also shown as the dashed line [40]. The compilation of data is made by results from many $e^+e^-$ experiments [41, 47].

The leading effect is related to the quantum number flow conservation and consists in a high probability to emit a forward baryon with large longitudinal momentum along the direction of the incident beams. This forward emitted particle carries away a fraction of the incident primary energy and therefore reduces the "effective" energy available for particle production. When considering the leading effect, defining new variables to estimate the effective energy available for particle production, common universal features

can be found in the two interaction systems. According to the experimental results obtained up to the highest energies studied so far, e⁺e⁻ collisions do not produce hadronic systems with leading hadrons. As a matter of fact the leading effect holds true in strong, electromagnetic and weak interactions provided a hadron is present in the initial state, regardless if the hadron transforms into another hadron or not. In general the production of leading particles (protons and neutrons in pp collisions) is related to the necessity of quantum number flow conservation in an interaction. In pp collisions the proton beams carry a baryon number flux which must be conserved in the interaction and therefore in these collision systems leading protons and neutrons are produced [48].

Figure 2.3 shows a schematic comparison of e⁺e⁻ and pp collision phenomenology. The jets produced in annihilation e⁺e⁻ processes have the same energy and opposite direction. In pp collisions the production of leading nucleons is not correlated in the two hemispheres and therefore jets will have different energies and uncorrelated directions.
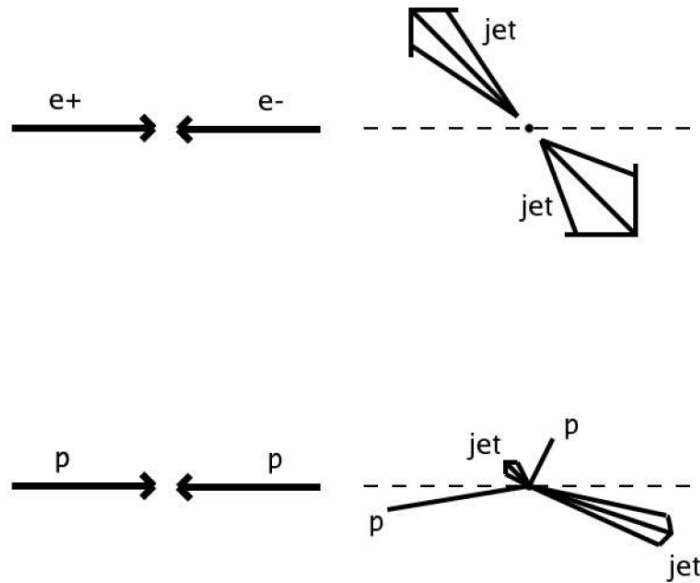


Figure 2.3: Schematic explanation of e⁺e⁻ and pp collisions phenomenology. While in e⁺e⁻ interactions the produced jets have the same energy and opposite direction, in pp collisions they have different energies and uncorrelated directions.

## 2.2   Effective Energy

As a consequence of the leading effect, in pp collisions the energy available for particle production is reduced with respect to the total center-of-mass energy as shown in Fig. 2.2. If the leading effect is taken into account, one could define the *effective energy* available for particle production in pp collisions, $E_{eff}$, and consider the dependence of global observables as a function of this new variable instead of $\sqrt{s}$. In this scenario one could expect common universal features in the two different interaction systems, $e^+e^-$ and $pp(\bar{p})$. One way of estimating the effective energy could be on an event-by-event basis by measuring the energy of the leading baryon ($E_{leading}$) in each event hemisphere[3] $i$:

$$(E_{eff})_i = \sqrt{s}/2 - (E_{leading})_i \quad \text{for } i = 1, 2 \quad . \tag{2.1}$$

If one could demonstrate the independence of the two event hemispheres with respect to the leading effect, the total effective energy $E_{eff}$ available for particle production in the event could be derived from the measurement of only one leading particle per event by:

$$E_{eff} = 2(E_{eff})_i = \sqrt{s} - 2(E_{leading})_i \quad \text{for } i = 1 \text{ or } 2. \tag{2.2}$$

The average total charged multiplicity would then be:

$$< n_{ch} > = 2 < n_{ch} >_i \quad \text{for } i = 1 \text{ or } 2. \tag{2.3}$$

The independence of the two event hemispheres with respect to the emission of leading baryons was actually experimentally observed at ISR by the BCF group [49], studying the Feynman-$x$ ($x_{\mathrm{F}}$) distribution of emitted leading baryons in the two hemispheres. In fact, the most convenient way of studying the leading effect is to use fractional energy or momentum variables such as $x_{\mathrm{F}}$. The Feynman-$x$ of a leading baryon in a hemisphere $i$ can be written as:

$$x_{\mathrm{F}} = 2p_{\mathrm{L}i}/\sqrt{s} \quad \text{for } i = 1 \text{ or } 2, \tag{2.4}$$

where $p_{\mathrm{L}}$ is the longitudinal momentum of the leading particle. The variable $x_{\mathrm{F}}$ ranges from 0 to 1. The results are presented in Fig. 2.4 as a scatter plot in terms of the quantities $x_1^{lead}$ and $x_2^{lead}$, representing the Feynman-$x$ of leading protons in the two

---

[3]The hemispheres are defined with respect to a plane transverse to the direction of the incident beams in the center-of-mass system.

hemispheres. Each point in the scatter plot represents an event. The uniformity of the events in the plot is the proof that there is no correlation between the two leading protons emitted. A more quantitative analysis of the same data is reported in Fig. 2.5 where a range of $x_1^{leading}$ is shown in the abscissa and the average value of $x_2^{leading}$ is plotted in the ordinate.
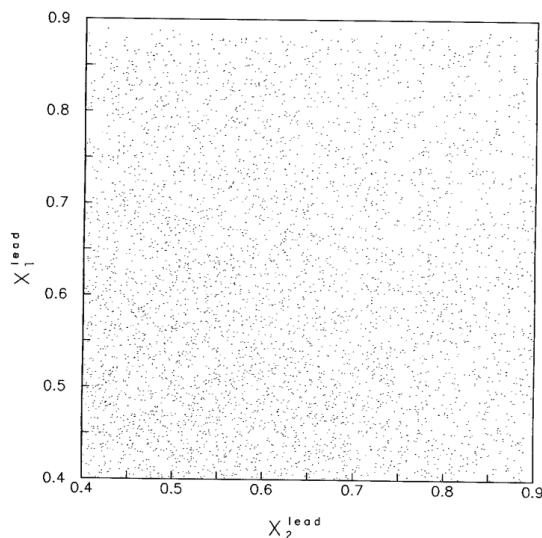


Figure 2.4: Scatter plot in terms of the quantities $\mathrm{x}_1^{lead}$ and $\mathrm{x}_1^{lead}$, representing the Feynman-$x$ of leading protons in the two hemispheres. Each point $(\mathrm{x}_1^{lead}, \mathrm{x}_2^{lead})$ in the scatter plot represents one event [49].

An alternative method to Eq. 2.2 to measure $E_{eff}$, in those events where a leading particle can be measured in both hemispheres, is the relation:

$$E_{eff} = \sqrt{s[1 - (x_\mathrm{F})_1][1 - (x_\mathrm{F})_2]} \quad . \tag{2.5}$$

The two methods of defining the effective energy in the event have been proved to be equivalent, however the first one has the advantage of making optimal use of the data in terms of the collected event statistics. This is due to the much larger acceptance and efficiency of single with respect to double leading particle detection.
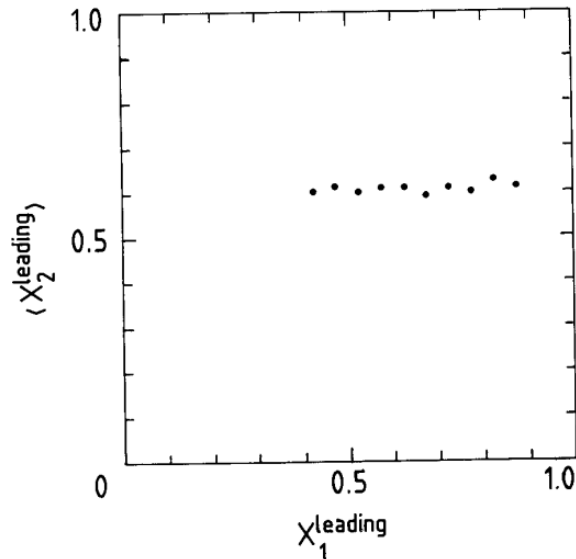
29

Figure 2.5: Quantitative plot showing one Feynman-$x$ of leading proton is not dependent on the Feynman-$x$ of the other leading protons [49].

As mentioned before, after taking into account the leading effect, the study of correlations between charged particle multiplicity and effective energy instead of center-of-mass energy shows a very good agreement between $e^+e^-$ and pp collisions, as shown in Fig. 2.6. The pp data in this figure refer to a "minimum bias[4]", with leading protons in the range $0.3 < x_F < 0.8$, collected by the SFM experiment at the CERN ISR. The data from $e^+e^-$ experiments are also shown [50].

## 2.3 Experimental results on the leading effect

As already mentioned, at first sight there is no universality in the final state hadrons produced in $e^+e^-$ and pp collision systems at fixed $\sqrt{s}$, but one expects common universal features when taking into account the leading effect. Besides charged particle multiplicity, other observables were considered by the BCF group in order to study this phenomenon, among which the longitudinal and transverse momentum distributions,

---

[4]Events collected with a trigger that applies the most possible unbiased selection are referred to as minimum bias events (MB).
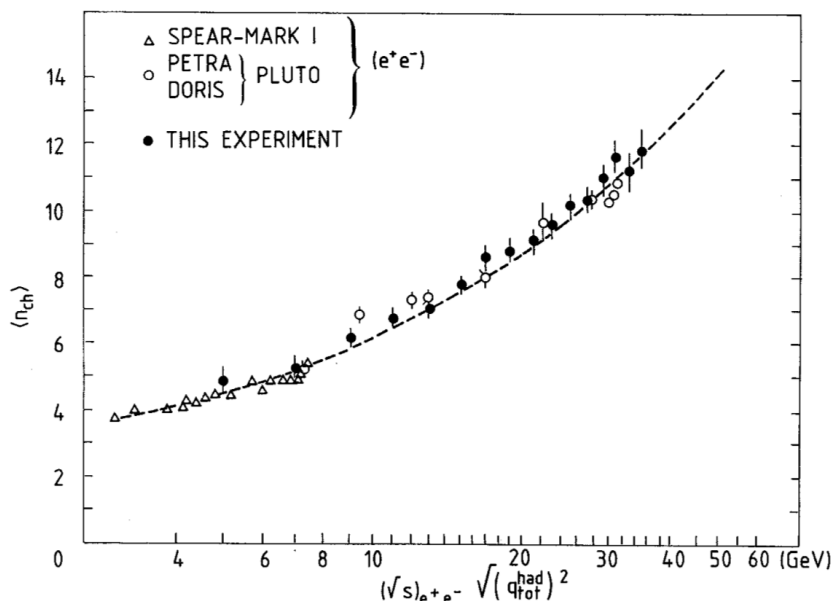
Figure 2.6: Average charged multiplicity as a function of the effective energy $E_{eff}$, here indicated as $\sqrt{(q_{had}^{tot})^2}$. The data were measured in minimum bias pp collisions collected by the SFM experiment at the CERN ISR (full circles). The data from other $e^+e^-$ experiments are also shown (open circles and triangles) in terms of $\sqrt{s}$ [50].

the ratio of "charged" to total energy of the multiparticle hadronic system produced, the event planarity etc. As mentioned above, the first evidence for universality features between $e^+e^-$ and pp data was found using pp interactions at the "nominal" ISR energy, $(\sqrt{s})_{pp} = 62$ GeV. As reported in Fig. 2.7 this fixed energy corresponds to a set of "effective energies", available for particle production, which goes from few GeV up to about 40 GeV. In this plot three scenarios of incident energies are considered: $E_{inc} = 31$ GeV, $E_{inc} = 22$ GeV and $E_{inc} = 15$ GeV, using collected data at three ISR energies, $(\sqrt{s})_{pp}$ = 30, 44, and 62 GeV. It was a crucial point for the BCF group analysis to show that the multiparticle hadronic systems produced in pp interactions, with the same values of $2E_{had}$[5] but different values of $E_{inc}$, had the same properties in terms of the observables mentioned above. Let's consider for instance the inclusive momentum distribution of the particles produced in pp. This observable is usually expressed as a function of the fractional variable $x_{\mathrm{R}}^*$:

$$x_{\mathrm{R}}^* = p/E_{had} \quad , \tag{2.6}$$

---

[5]The variable $E_{had}$ is equivalent to $E_{eff}$ in this context.

31

obtained by dividing the momentum $p$ of the particle by the energy of the hadronic system rather than by the energy of the beams.
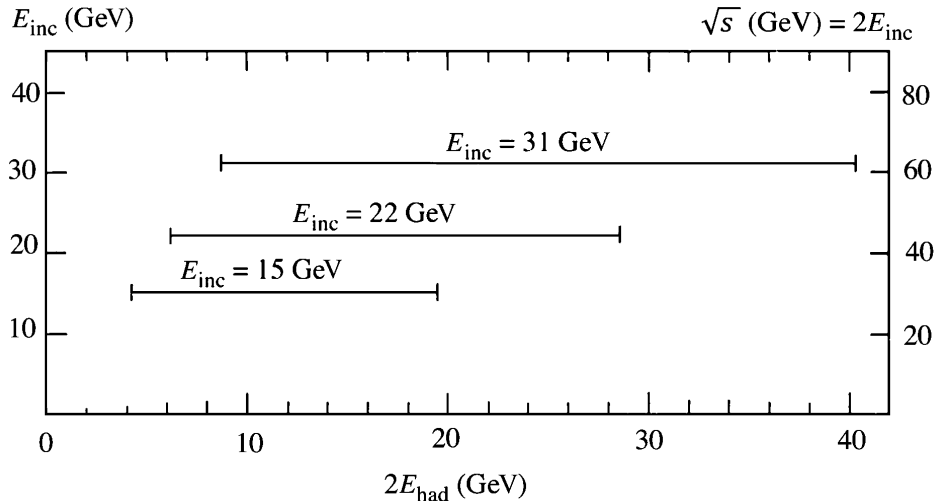


Figure 2.7: On the left vertical axis the plot shows the beam energy $E_{inc}$ and on the right the center of mass energy $\sqrt{s}$. The abscissa shows the effective hadronic energy $2E_{had}$ available for particle production [55].

Figures 2.8(a) and (b) show the momentum distribution, $\mathrm{d}\sigma/\mathrm{d}x_{\mathrm{R}}^*$, at the nominal center of mass energy of $\sqrt{s} = 62$ GeV for different values of effective hadronic energy available for particle production. High values of $E_{had}$ means less leading proton effect. The $e^+e^-$ data at the equivalent energies are also shown and the overall agreement between the two collision systems is good [51].

When considering the leading effect another interesting property of the multiparticle hadronic systems produced in pp interaction is the inclusive transverse momentum distribution. Figure 2.9 shows the BCF results obtained at $\sqrt{s} = 30$ GeV selecting a sample of events in the hadronic energy range $(11 \leq 2E_{had} \leq 13)$ GeV, compared with $e^+e^-$ data at $(\sqrt{s})_{e^+e^-} = 12$ GeV, showing an excellent agreement [53][54].
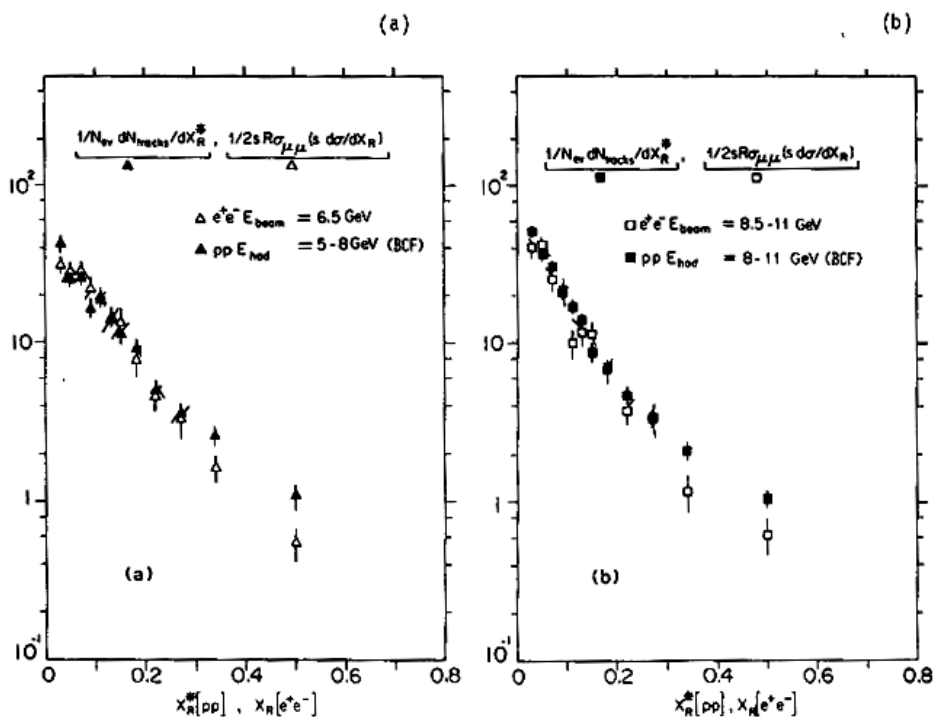
Figure 2.8: Inclusive momentum distribution of the particles produced in pp, $d\sigma/dx_R^*$, at the nominal center of mass energy of $\sqrt{s} = 62$ GeV for different values of effective hadronic energy available for particle production, $5 \leq E_{had} \leq 8$ GeV and $8 \leq E_{had} \leq 11$ GeV [51]. The plots also show the e$^+$e$^-$ data at the equivalent energies collected at PETRA (TASSO) [52].

Another impressive set of results comes from studying some very interesting properties of the leading effect. Among these an impressive study shows the leading effect is flavour independent, i.e. is the same for baryons containing different types of quarks. In order to reach such result, the search is extended to all heavy flavours. The experimental results in Fig 2.10 prove that the same leading baryon effect is present in $\Lambda_b^0$, $\Lambda_c^+$, and $\Lambda_s^0$ production mechanisms, despite the large mass difference between strange, charm and bottom quarks. These results allow to conclude that the leading effect is flavour independent and there is no mass dependence in this phenomenon [55].
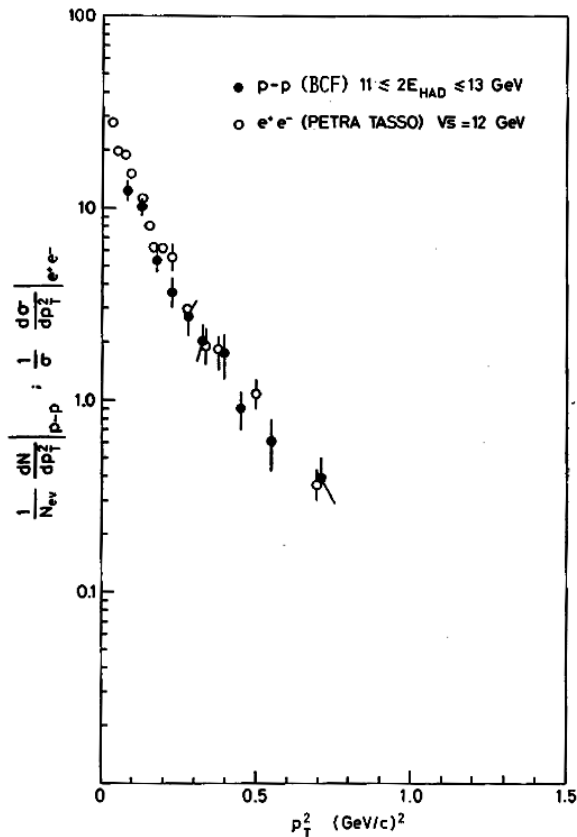
Figure 2.9: The inclusive trasverse momentum squared distribution measured by the BCF collaboraton at ISR for $(11 \leq 2E_{had} \leq 13)$ GeV [54]. This is compared with e$^+$e$^-$ data at $(\sqrt{s})_{\mathrm{e^+e^-}} = 12$ GeV measured at PETRA (TASSO) [53].

## 2.3.1 Leading effect in A-A collisions

In pp/$\bar{\mathrm{p}}$p collisions, a single constituent (or dressed) quark from each nucleon takes part in a collision and the rest are considered as spectators. Thus, the effective energy for the production of secondary particles is the energy carried by a single quark pair (i.e. 1/3) of the entire nucleon energy. In head-on heavy-ion collisions described by the Glauber model each participating nucleon is typically struck 3 - 6 times on average as it passes through the oncoming nucleus in a central event (the exact value of this number is determined by the energy-dependent nucleon-nucleon inelastic cross section, $\sigma_{NN}(s)$). This makes much more energy of the colliding nucleons (participants) available for secondary particle production.
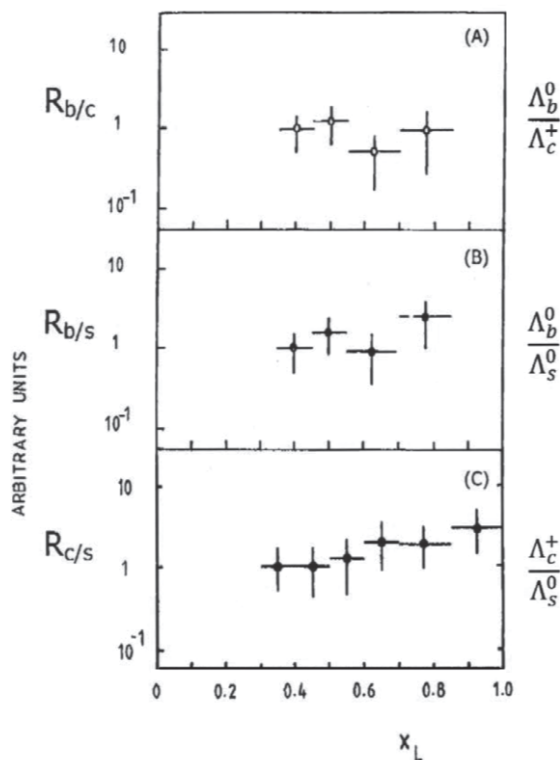
34

Figure 2.10: Production distributions vs. $x_L$ of heavy flavour states $\Lambda_b^0$ and $\Lambda_c^+$ compared with the lightest flavour state $\Lambda_s^0$ (B) and (C). The data in (A) also show $\Lambda_b^0$ with respect to $\Lambda_c^+$ [55].

In Fig. 2.11 data on $N_{ch}$ from pp, $\bar{p}p$, $e^+e^-$ and central heavy ion collisions (scaled by $N_{part}/2$) are shown as a function of $\sqrt{s}$. Heavy ion data are shown for central Au-Au events at RHIC [56], Au-Au events from E895 at the AGS ($\sqrt{s_{NN}} = 2.6$ - 4.3 GeV) [57] and Pb-Pb events from NA49 at the SPS ($\sqrt{s_{NN}} = 8.6$, 12.2 and 17.3 GeV) [58]. The figure shows that the heavy-ion data does not follow exactly the $e^+e^-$ trend over the whole energy range. They lie below the pp data at AGS energies and join the $e^+e^-$ data above the top SPS energy. Thus, at high energies, the multiplicity measured per participant pair in Au-Au collisions scales in a similar way as $e^+e^-$ data at the same $\sqrt{s}$. If we understand the lower effective energy available in pp collisions as a consequence of the "leading particle effect", the Au-Au data suggest a substantially reduced leading particle effect in central collisions of heavy nuclei at high energy [56].
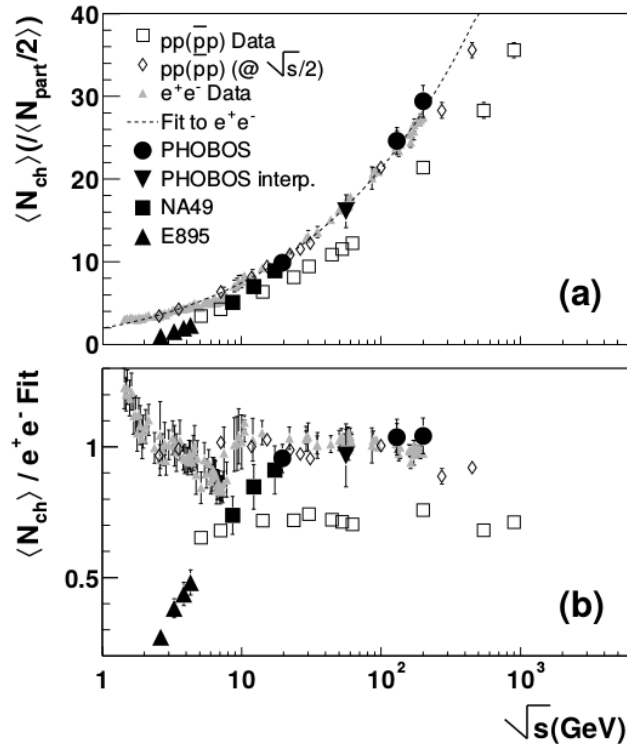
35

Figure 2.11: (a) Charged multiplicity $< N_{ch} >$ in pp, $\bar{p}p$, $e^+e^-$ and central Au-Au events as a function of center-of-mass energy. The Au-Au data are normalized by $N_{part}/2$. The dotted line is a perturbative QCD expression fit to the $e^+e^-$ data. (b) The data in (a) are divided by the $e^+e^-$ fit, to allow direct comparison of different data at the same $\sqrt{s}$ [56].

## 2.3.2 Leading effect at the LHC

A similar analysis to that performed at the ISR can be reproduced using pp collisions data collected at the LHC. We mentioned that one way of estimating the effective energy could be on an event-by-event basis by measuring the energy of the leading baryon ($E_{leading}$) in each event hemisphere (Eq. (2.1)), but this kind of analysis requires a detector able to measure particles with large longitudinal momenta. In particular, as it will be shown in the next chapter, the ALICE experiment at CERN has a very good capability for this kind of measurement thanks to its Zero-Degree Calorimeters, which, even though optimized for Pb-Pb collisions, have a sufficient energy resolution in the forward region to make possible a pp data analysis in terms of "effective energy". As already mentioned,

the understanding of particle production in pp interactions, the most elementary system studied at the LHC, is one of the key ingredients to separate genuine QGP signatures from cold nuclear matter effects in Pb-Pb, but it is also interesting on its own when looking at possible hints for medium effects in small systems. In this respect, the characterization of strangeness production with the ZDC activity would be crucial to distinguish initial and final state effects of pp collisions. In particular, this thesis proposes to shed light on the nature of the similarities observed in pp, p-Pb and Pb-Pb collisions in terms of strangeness production [1] in relation to the information available from the ALICE forward calorimeters on effective energy. This kind of study could be crucial to improve our understanding on the underlying QCD mechanisms in hadron interactions.

# Chapter 3

# A Large Ion Collider Experiment

ALICE (A Large Ion Collider Experiment) is a dedicated heavy-ion detector, located along the Large Hadron Collider (LHC) at CERN. It was built to exploit the unique physics potential of Pb-Pb interactions and aims to study the physics of strongly interacting matter at extreme energy densities where the QGP is formed. By the time the LHC and ALICE became operative in 2010, it was established that the QGP had indeed been observed by the experiments at RHIC. Therefore, ALICE main goals during its first physics program were to study its characteristics, to explore the phase diagram of strongly-interacting matter and to study the phase transition between hadronic matter and the QGP. Nevertheless, besides focusing on heavy ion collisions, ALICE is also interested in studying pp and p-Pb interactions. Indeed the comparison between the three collision systems is crucial to distinguish QCD properties with and without medium effects.

## 3.1   The Large Hadron Collider LHC

The Large Hadron Collider (LHC) [19] is one of the largest circular colliders ever built, located at the European Organization for Nuclear Research (CERN), near Geneva, positioned underground between 50 m and 175 m depth. Inside the LHC ring of circumference 26.7 km, two beams of protons or heavy ions circulate in opposite directions. The full accelerator complex of CERN is shown in Fig. 3.1. The full LHC ring has ∼1200 dipole magnets for bending the beams and ∼400 quadrupole magnets for focusing the beam.
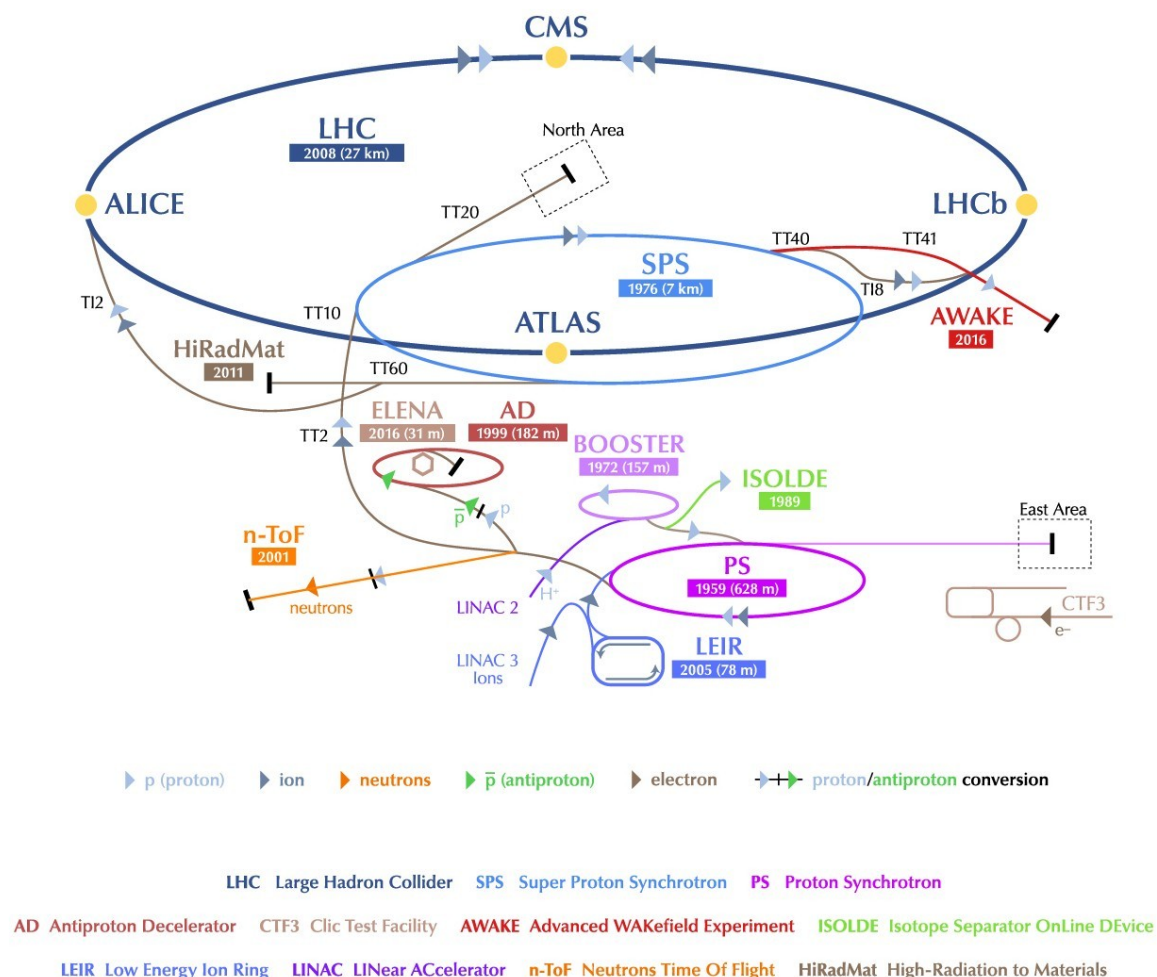
Figure 3.1: Schematic view of CERN accelerator complex with its main components and its four main experiments (ALICE, ATLAS, CMS and LHCb) highlighted.

In order to create a proton beam, hydrogen atoms are stripped off electrons by applying an electric field. These protons are then injected from a linear accelerator (LINAC-2) into the Proton Synchrotron Booster (PSB) where the proton energy is increased. Afterwards the beams pass to the Proton Synchrotron (PS) for further acceleration and then are sent to Super Proton Synchrotron (SPS) before the injection into the LHC. Each interaction point along the LHC ring is covered by large detector system, each of which has its unique physical goals and research objectives. CMS (Compact Muon Solenoid)

and ATLAS (A Toroidal LHC ApparatuS) were conceived to study the creation and the properties of the Higgs boson and to explore the physics beyond the Standard Model. The main purpose of LHCb (Large Hadron Collider beauty) experiment is to study the CP violation in physics of heavy quarks and ALICE physics goals were discussed in the previous chapter, and will be described in details in the following sections.

## 3.2    The ALICE detectors

ALICE is a 26 m long, 16 m high, and 16 m wide detector, mainly addressed to study the Quark Gluon Plasma produced in heavy-ion collisions at the LHC. The detector has been designed to cope with the high particle multiplicity environment expected in such collision systems and to provide unique Particle IDentification (PID) performance that allows a comprehensive study of particles produced in the collision, down to very low transverse momentum (0.1 GeV/$c$). The ALICE detector setup is shown in Fig. 3.2.
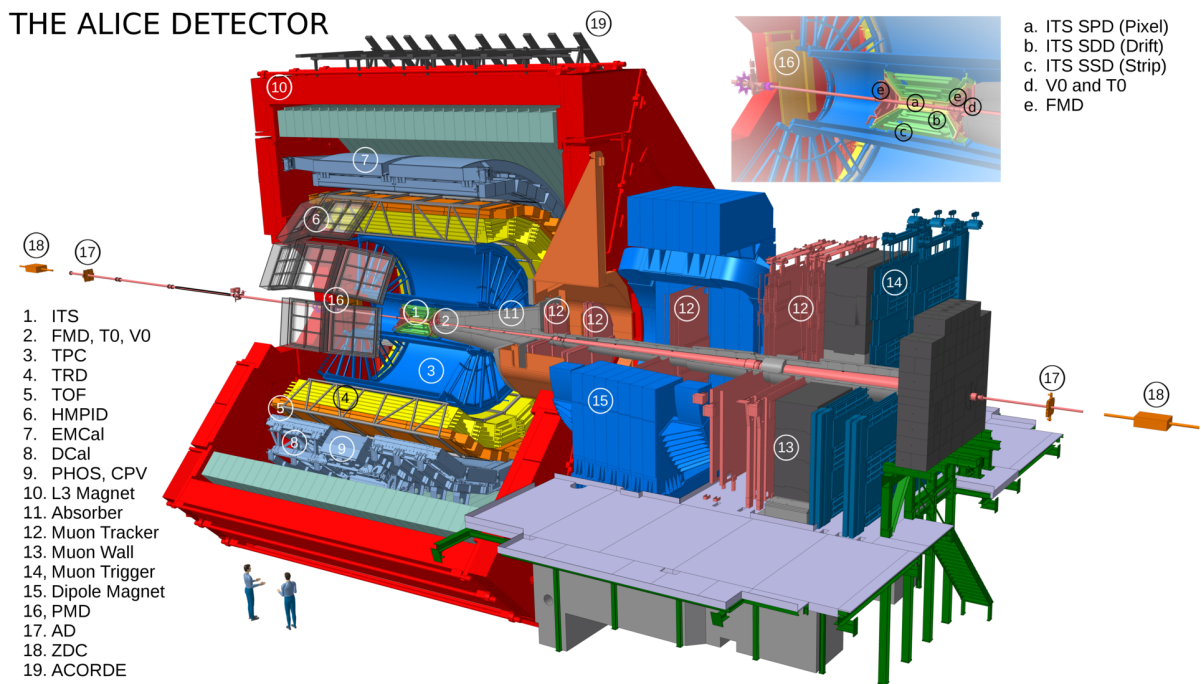


Figure 3.2: Schematic view of the ALICE detector.

The detectors can be classified in three groups:

- **The central barrel detectors**, which include, starting from the interaction region and going outward:

  - Inner Tracking System (ITS);
  - Time Projection Chamber (TPC);
  - Transition Radiation Detector (TRD);
  - Time of Flight (TOF);

  This group of subsystems have full azimuthal ($0 \leq \phi \leq 2\pi$) coverage with rapidity acceptance $|\eta| < 0.9$ and is enclosed in the L3 solenoid magnet which provides a 0.5 T nominal magnetic field. They are mainly dedicated to the vertex reconstruction, tracking, particle identification and momentum measurement. In the mid-rapidity region there are also some detectors with limited acceptance:

  - High-Momentum Particle Identification Detector (HMPID);
  - PHOton Spectrometer (PHOS);
  - ElectroMagnetic CALorimeter (EMCAL) and Di-jet Calorimeter (DCal).

- **Muon spectrometer**, which is placed in the forward pseudorapidity region (-4.0 $\leq \eta \leq$ -2.5). This detector consists of a dipole magnet, tracking and trigger chambers; it is optimized to reconstruct heavy quark resonances through their $\mu^+\mu^-$ decay channel and single muons.

- **Forward detectors**, which are placed in the high pseudorapidity region with different acceptances. These detectors are specialized systems used for triggering or to measure global event characteristics. They include:

  - Forward Multiplicity Detector (FMD) (-3.4 $< \eta <$ 5.1);
  - Photon Multiplicity Detector (PMD) (2.3 $< \eta <$ 3.7);
  - Zero Degree Calorimeters (ZDC) ($\eta >$ 4.0);
  - V0 Detectors (2.8 $< \eta <$ 5.1 for V0A and -3.7 $< \eta <$ -1.7 for V0C) ;
  - T0 Detectors (4.61 $< \eta <$ 4.92 for T0A and -3.28 $< \eta <$ -2.97 for T0C).

Moreover, besides the detectors listed above, an array of scintillators (ACORDE) is installed on top of the L3 magnet in order to trigger on cosmic rays.

### 3.2.1 The Inner Tracking System (ITS)

The Inner Tracking System (ITS) is the innermost of the ALICE barrel detectors [59]. The detector is placed very close to the beam pipe, covering a radius that ranges from 3.9 cm to 43 cm. Starting from the beam pipe and moving radially in outward direction, the ITS is composed by a total of six layers:

- *two Silicon Pixel Detector (SPD)* layers located at 39 and 70 mm from the beam-pipe and based on hybrid silicon pixels that consist of a two dimensional matrix (called sensor ladder) of reverse-biased silicon detector diodes. The purpose of the SPD is to provide ALICE with adequate secondary vertexing capability for charm and beauty detection in such a high multiplicity environment. Therefore due to the high track density, these two innermost layers guarantee a high granularity. In particular the first layer of the SPD is used to measure the charged particle multiplicity, together with Forward Multiplicity Detectors (FMD). Each diode of the internal SPD is bumped-bound on the readout chips which provide a binary output only and therefore provides only hit information on the track and no energy loss measurement;

- *two Silicon Drift Detector (SDD)* layers, the two intermediate layers of the ITS, which, together with the two outer most layers SSD (see later), have analogue read-out and therefore can be used for Particle IDentification via dE/dx measurement for low momentum particles ($p_T < 100$ MeV/$c$). Since the momentum resolution for low-$p$ particles is dominated by multiple scattering effects, the amount of material in the active volume has been kept to a minimum. Each SDD is made of a 12.7 cm diameter and 0.3 mm thickness silicon wafer. When a particle crosses the thickness of SDD, electrons are released and they drift under the effect of an applied electric field towards an array of anodes. In this way the $y$ coordinate of the particle is given by the measurement of the drift time and the $x$ coordinate is obtained from the centroid of the electrons along the anodes;

- *two Silicon Strip Detector (SSD)* layers, which, besides providing energy loss measurements, play a crucial role in the tracking of the particles produced in the collisions connecting the tracks from the external detectors (i.e. Time Projection Chambers) to the ITS inner layers.

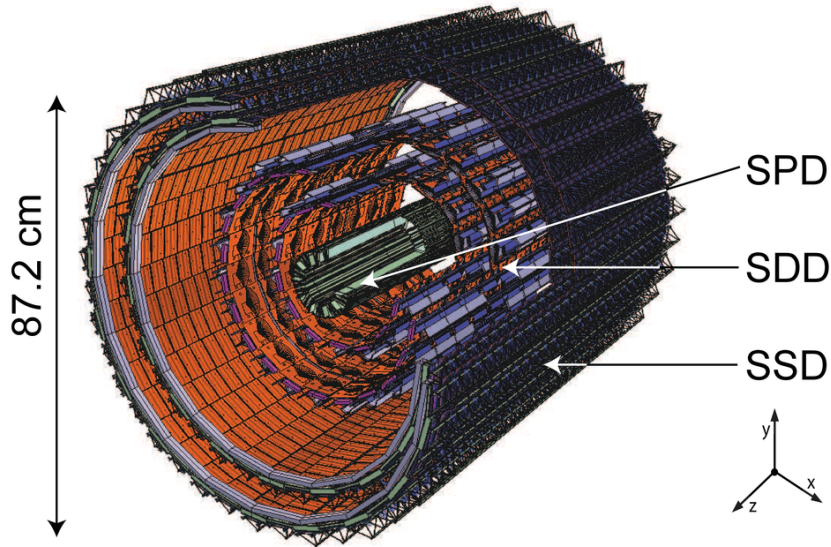A schematic view of the detector is shown in Fig. 3.3.

Figure 3.3: Schematic view of ALICE 6 layers Inner Tracking System.

### 3.2.2 Time Projection Chamber (TPC)

The Time Projection Chamber (TPC) is the main central barrel detector in ALICE [60]. Together with the ITS, TRD, and TOF, it provides charged particle momentum measurement (covering from about $p_T \sim 0.1$ GeV/$c$ up to $p_T \sim 100$ GeV/$c$), particle identification and vertex determination with sufficient momentum resolution, two track separation and dE/dx resolution for studies of hadronic and leptonic signals. The TPC is a 88 m$^3$ cylinder filled with gas and divided in two drift regions by a central electrode. During Run 1 the detector was filled with a mixture of Ne and $CO_2$ (2009-2012), while at the beginning of the LHC Run 2 (2015-2018) a mixture of Ar and $CO_2$ has been used. Charged particles traversing the TPC volume ionise the gas along their path, creating free electrons and ions, the drift field separates the two charges and the electrons drift to the end-plates. The parameters of the particle trajectory inside the known magnetic field are then used to measure the momentum of the particle. The electrons and ions produced in the ionization process are accelerated by the applied external electric field and get drifted towards the read out chambers and the Central Electrode (CE) respectively. The readout chambers consist of a system of multi-wire proportional chambers (MWPC) with

cathode pad read-out. An electron avalanche is produced in the high electric fields in the vicinity of the anode wires, and the primary ionization signal is amplified by this avalanche process. The electrical signal induced by the positive space charge onto a segmented pad plane is shaped, amplified, digitalized, processed and readout from each readout pad by the data acquisition system. A schematic view of the detector is shown in Fig. 3.4.
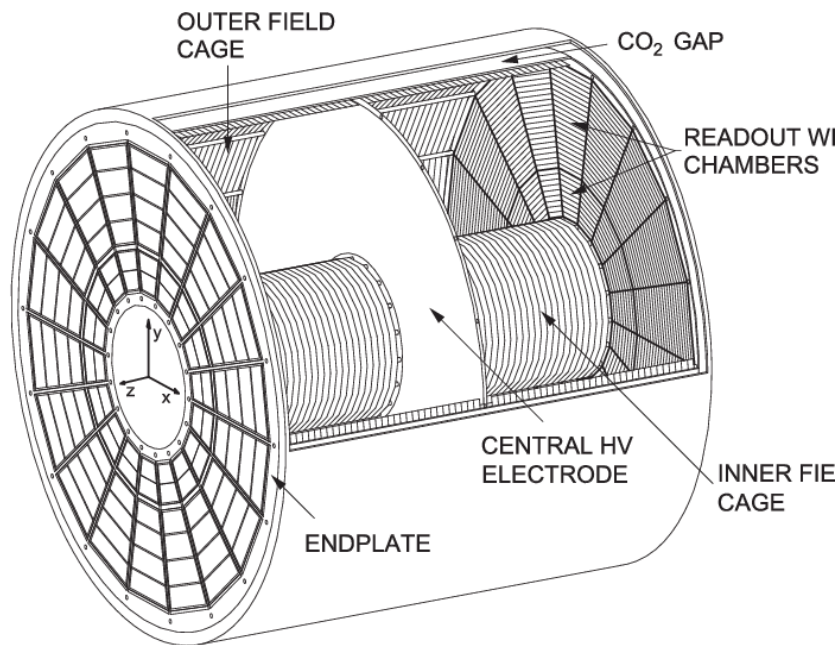


Figure 3.4: 3D view of the TPC field cage.

### 3.2.3 Transition Radiation Detector (TRD)

The Transition Radiation Detector (TRD) [61] is placed around the TPC, the radial position of the detector is in between 2.9 m and 3.7 m with pseudorapidity coverage $|\eta| < 0.84$. The main purpose of the TRD is to provide electron identification in the region of transverse impulse $p_{\mathrm{T}} > 1 \, \mathrm{GeV}/c$ (below this threshold electrons can be identified with the TPC), and pion rejection in this momentum range. The working principle of the detector is based on the so-called transition radiation produced by a relativistic electron crossing materials with different dielectric constants. The radiator releases X-ray photons

45

in the energy range 1-30 keV. Pion, being heavier than electrons, do not emit radiation below a transverse momentum of 100 GeV/$c$, and therefore, TRD has a very efficient pion rejection capability. Using also the information from the ITS and the TPC, it is possible to study the production of vector meson resonances through their lepton decay channel $e^+e^-$. Each detector element consists of a 48 mm thick radiator, a drift section of 30 mm thickness and a multi-wire proportional chamber with pad readout filled with a mixture of Xe-$CO_2$. Moreover the TRD is a part of the Level 1 trigger, and is used to derive a fast trigger for charged particles of high momentum.

### 3.2.4   Time Of Flight (TOF)

The Time of Flight (TOF) [62] detector is dedicated to charged particle identification in the pseudorapidity region $|\eta| \leq 0.9$, in the intermediate momentum range, below $\sim 2.5$ GeV/$c$ for pions and kaons, up to 4 GeV/$c$ for protons and with a separation of $\pi$/K and K/p better than $3\sigma$. The TOF measures the time needed by the particles produced in the interaction point to travel from the primary vertex to its sensitive surface. This information is combined with that of the particle momentum $p$, provided by the tracking detectors to estimate the mass $m$ of the particle. The precise determination of the event collision time, the so called $t_0$, represents an important ingredient for the TOF PID and is determined using the information from the T0 detector. The TOF is a large MRPC-array at a distance of 3.7 m from the beam line, externally to the TRD, covering the full azimuthal angle. It is made of 1638 MRPCs located in 90 gas-tight modules distributed over 18 azimuthal Super Modules. Each MRPC is composed of 96 readout pads and the whole TOF detector consists of $\sim$ 160000 readout channels each of 2.5 x 3.5 cm$^2$. Thanks to this highly segmented structure, the TOF occupancy can be kept low while keeping a good performance also in a high multiplicity environment. A schematic view of the detector spaceframe is shown in Fig. 3.5. During collisions, the time resolution of the TOF was measured to be about 56 ps [63], which is very close to the performance obtained on test beam data.
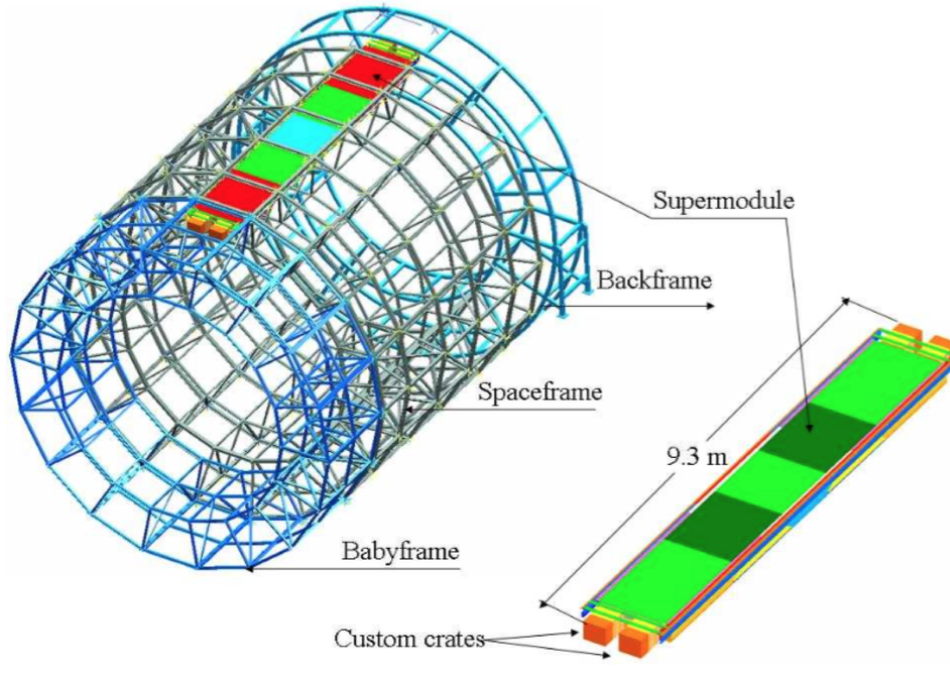
Figure 3.5: Schematic drawing of the TOF detector spaceframe highlighting one of the detector supermodule.

### 3.2.5 The Muon Spectrometer

In the framework of the ALICE physics program, the goal of the Muon spectrometer [64] is the study of open heavy flavour production and quarkonia production (J/$\psi$, $\psi'$ and $\Upsilon$(1S), $\Upsilon$(2S) and $\Upsilon$(3S)) via their muonic channel ($\mu^+\mu^-$) decays, detecting muons in the pseudorapidity region -4.0 < $\eta$ < -2.5. The spectrometer consists of a passive front absorber, a high granularity tracking system of 10 detection planes, a large dipole magnet, which produces a field of 3 T·m, a passive muon filter wall followed by four planes of trigger chambers, and an inner beam shield. The front absorber suppresses all particles coming from the interaction vertex. It is made of carbon and concrete in order to limit the multiple scattering and the energy loss of the muons. The inner beam shield is made of tungsten, lead and stainless steel to minimize the background arising from primary particles emitted in the collision and it protects the chambers from background originating from particles at small angles. The "active" detector consists of 4 plates which make up the muon triggering system. They use RPC chambers working in the streamer regime, whose aim is to select events with a $\mu^+\mu^-$ pair at high $p_\mathrm{T}$. The tracking

system is made of 10 cathode pad/strip chambers arranged in 5 stations of 2 chambers each. The spatial resolution is better than 100 $\mu$m. Four chambers are placed in front of the dipole magnet, another two inside it, and four after it. The layout of the muon spectrometer is presented on Fig. 3.6.
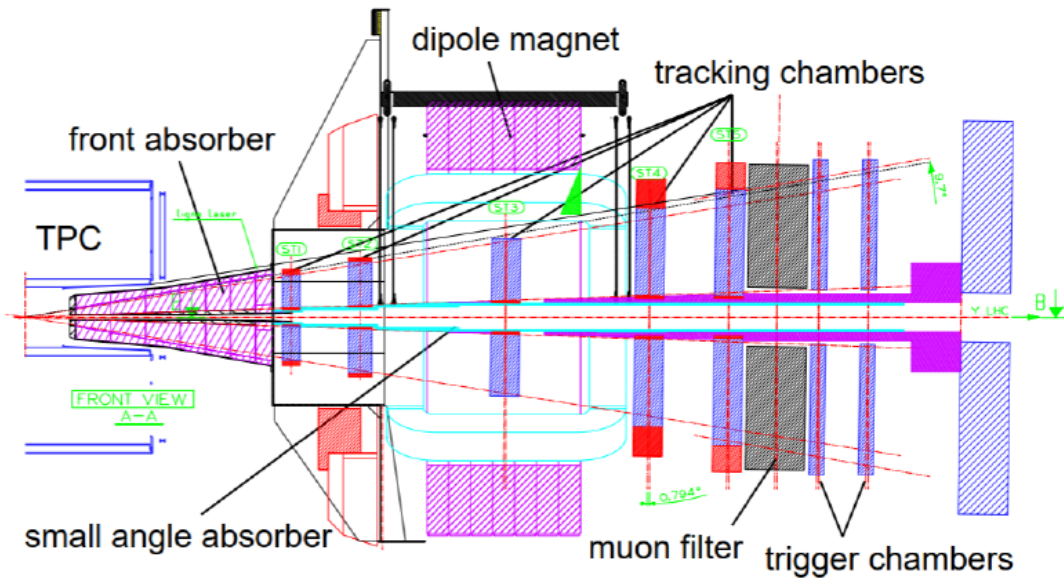


Figure 3.6: Schematic view of the ALICE Muon Spectrometer.

### 3.2.6   The forward detectors

**Forward Multiplicity Detector (FMD)**

The Forward Multiplicity Detector (FMD) [65] measures the charged particle multiplicity at a very forward rapidity region (-3.4 < $\eta$ < -1.7 and 1.7 < $\eta$ < 5.0) with full azimuthal coverage. The FMD consists of 5 rings (3 inner rings and 2 outer rings) of silicon strip detector, which count charged particles. FMD3 and FMD2 rings are located on either side of the ITS detector (at about 75 cm from the IP) while FMD1 is placed at 320 cm from the IP on the opposite side with respect to the muon spectrometer.

**T0**

The T0 detector [65] consists of two arrays of Cherenkov counters, called T0A and T0C, and is a fast timing and triggering detector, providing early trigger to TRD and the precise start signal for the TOF with a time resolution of 50 ps. T0A is located at about 3.6 m away from the IP with pseudorapidity coverage $4.5 < \eta < 5.0$. T0C is located at about 70 cm away from the IP opposite to T0A with pseudorapidity coverage $-3.3 < \eta < -2.9$.

**V0**

The V0 [65] is a forward detector consisting of two arrays of scintillator counters, called V0A and V0C. V0A is located on the positive z-direction at about 3.4 m from the ALICE vertex on the opposite side to the muon spectrometer and provides pseudorapidity coverage $2.8 < \eta < 5.1$. V0C is located on the other side of the vertex on the negative z-direction, at a distance of about 90 cm with pseudorapidity coverage $-3.7 < \eta < -1.7$. Each of the V0 arrays is segmented in four rings in the radial direction, and each ring is divided in eight sections in the azimuthal direction as shown in Fig. 3.7.
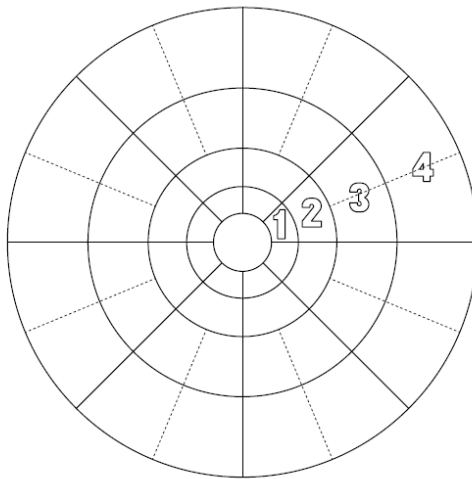


Figure 3.7: Segmentation of the V0A/V0C arrays.

This detector system has several functions, among which providing minimum-bias (MB) and high multiplicity (HM) triggers for the central barrel detectors in pp, p-Pb and

ion-ion collisions. These triggers are obtained from a large set of events with different numbers of emitted charged particles crossing this detector, detected with as large as possible efficiency. In the first data taking periods (starting from 2009), the ALICE MB trigger was built requiring a hit in the Silicon Pixel Detector (SPD) or in either of the V0 arrays (V0-A or V0-C). However in most recent data taking periods, given the increasing LHC luminosity and beam background, the trigger moved to a stricter condition using the coincidence between both V0 arrays and the LHC bunch crossing signals.

An important aspect to take under consideration is that, in both running modes (pp and Pb-Pb), a non-negligible background comes from interactions between the beams and the residual gas within the beam pipe and from interactions between the beam halo and various components of the accelerator such as collimators. However using the time of flight of particles detected by each V0 array, particles coming from collisions and particles coming from beam-gas background can be quite clearly distinguished. Another crucial role of the V0 system is that it provides a charged particle multiplicity measurement based on the energy deposited in the scintillators. The monotone dependence of the number of impinging particles on the V0 arrays from the number of primary emitted particles serves as an indicator of the centrality of the collision using the multiplicity recorded in the event as proxy. Through a detailed simulation of the apparatus, the relation between the total charge collected inside a V0 ring and the number of primary charged particles emitted into the corresponding pseudorapidity range can be extracted. Fig. 3.8 represents a typical distribution of the V0 amplitudes for all triggered Pb-Pb collisions at $\sqrt{s_{NN}} = 5.02$ TeV fitted with a Glauber Model. The shaded areas correspond to the different centrality classes used in physics analysis [66].
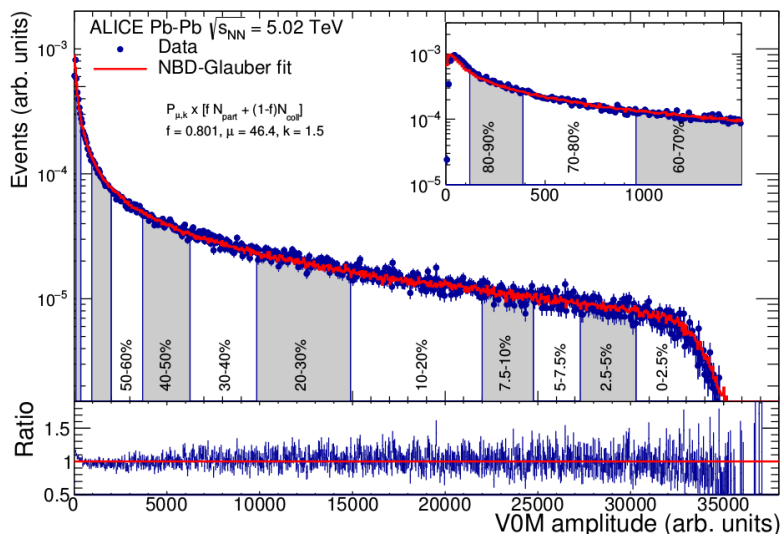
Figure 3.8: Distribution of the sum of amplitudes in the V0 scintillators for Pb–Pb collisions at $\sqrt{s_{NN}} = 5.02$ TeV. The distribution is fitted with a Glauber fit, which is shown as a line. The insert shows a zoom of the most peripheral region [66].

## 3.3 The Zero Degree Calorimeters

As already mentioned in the first chapter, since nuclei are extended objects, the volume of the interacting region depends on the impact parameter ($b$) of the collision. It is customary in the field of particle physics to introduce the concept of the centrality of the collision, which is directly related to the impact parameter. In so-called central collisions the two nuclei collide almost head-on and almost all nucleons within the nucleus participate in the collision. On the other hand, a peripheral collision has large impact parameter and only few nucleons participate in the collision. The nucleons that participate in the collision are called "participants" while those that do not interact are called "spectators". The energy $E_S$ carried away by the spectator nucleons is the measurable quantity most directly related with the centrality of the collision. It allows a direct estimate of the number of interacting (participant) nucleons $N_p$ through the simple relation:

$$N_p = A - E_S/E_A \tag{3.1}$$

where A is the mass number of the ion and $E_A$ is the beam energy per nucleon. Some simple considerations can be made to link the average number of participant nucleons

51

with the impact parameter $b$ of the collision, in the case of identical nuclei. However a more detailed calculation can be made in the framework of the Glauber theory.

At fixed-target experiments, the spectator nucleons, which typically fly away in the forward direction, are usually intercepted by means of zero degree calorimeters, usually placed close the beam axis, providing a measurement of $E_S$. This technique has been successfully adopted by several SPS heavy-ion experiments, such as WA80 [68], NA49 [67], and NA50 [69]. It has been shown that the measurement of projectile spectators in a ZDC is well correlated with other centrality estimators, such as charged hadron multiplicity. The design of devices for the detection of spectator nucleons for a ion collider experiment, like ALICE, differs significantly with respect to a fixed-target environment. In the case of LHC, the beams are deflected by means of two separation dipoles at a certain distance from the Interaction Point (IP), of the order of 50 m in ALICE, in order to reach the nominal distance of 188 mm between the beams. These magnets will also deflect the spectator protons, separating them from the spectator neutrons, which basically fly at 0 degrees. It is therefore conceptually necessary to place on the two sides of the IP a set of two devices, one positioned between the two beams to intercept the spectator neutrons, and one a little external to the outgoing beam, to collect the spectator protons [70].

### 3.3.1 Detector characteristics and detection technique of the ALICE ZDC

In ALICE, two sets of hadronic Zero Degree Calorimeters (ZDC) are located at 116 m on either side of the IP and in addition, two small electromagnetic calorimeters (ZEM) are placed at 7 m on both sides of the LHC beam pipe opposite to the muon arm [70]. As mentioned, at this distance from IP spectator protons are spatially separated from neutrons by the magnetic dipoles of the LHC beam line and therefore two distinct detectors are used. One for spectator neutrons, placed at zero degrees relative to the LHC axis, and one for spectator protons, placed externally to the outgoing beam pipe on the side where positive particles are deflected. The amount of space between the separating dipoles which could be allocated to the hadronic ZDC was quite small and therefore the transverse dimensions of the neutron device does not exceed the distance between the two beam pipes in that region ($\sim$88 mm). Fig. 3.9 and 3.10 show a schematic representation of the ZDC location in ALICE.
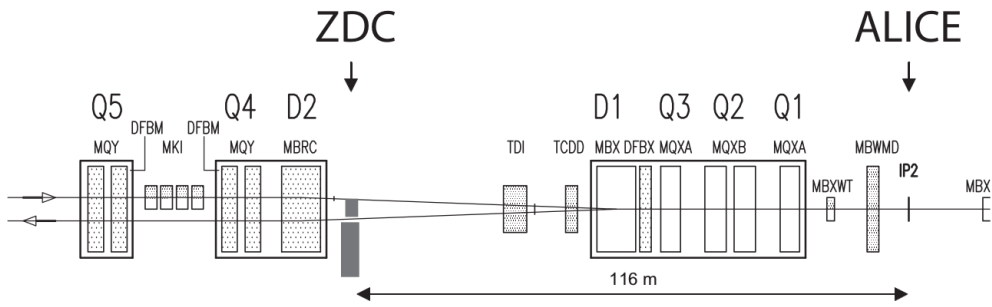
Figure 3.9: Schematic view of the beam line and the ZDC location.
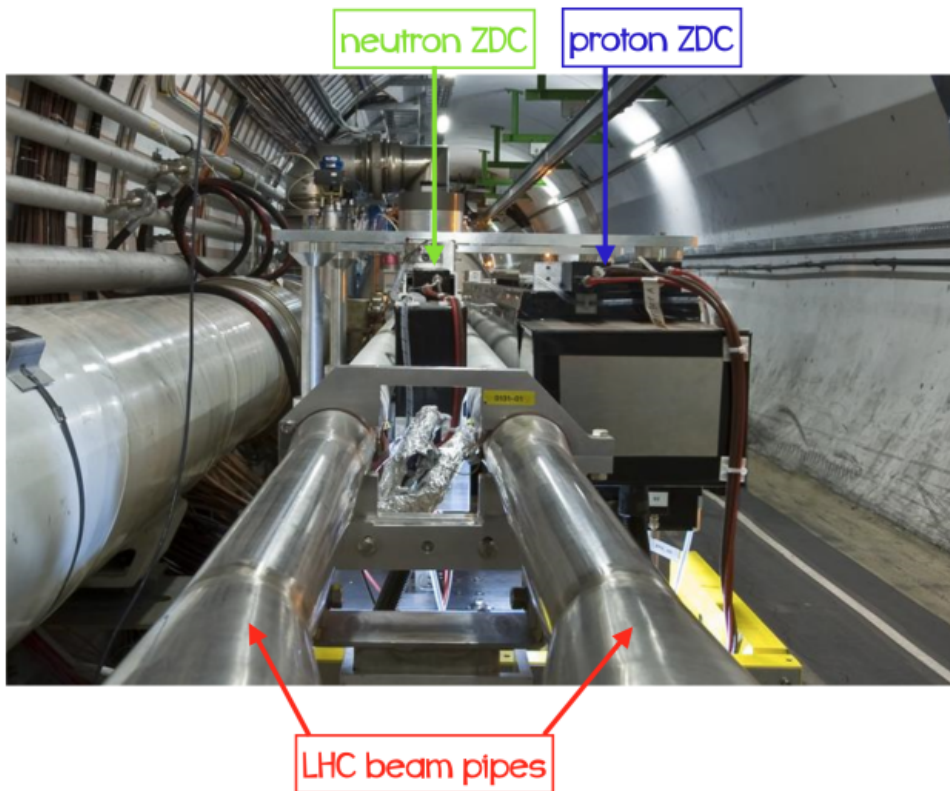


Figure 3.10: View of the ZDC location.

The detection technique adopted for the ALICE Zero Degree Calorimeters is the quartz fibres calorimetry. The shower generated by incident particles in a dense passive material produces Cherenkov radiation in quartz fibres ("active" material) embedded in the absorber. This technique has been chosen because it fulfils two fundamental requirements. First of all, due to the small amount of space available, the detectors need to be compact and therefore a very dense passive material should be used as absorber in order to contain the shower. Moreover, the ZDC operates in a very high radiation environment and radiation hardness is guaranteed by the high radiation resistance of quartz fibres. Moreover Cherenkov radiation ensures a very fast signal due to the intrinsic speed of the emission process.

**The neutron calorimeter (ZN)**

The design of the neutron calorimeter consists of heavy metal absorber plates stacked to form a parallelepiped. The quartz fibres embedded in the absorber are placed parallel with respect to the LHC axis (spaghetti calorimeter). The spectator neutrons, impinging on the front face of the detector, produce showers in the absorber/quartz matrix and the charged particles above the Cherenkov threshold produce photons that are transmitted through the quartz fibres up to the photodetectors. In order to see if the calorimeter is centred and to monitor the relative damage to the different sections, it is useful to divide the optical readout of the calorimeter into four independent towers. On the other hand, in order to make the energy calibration easier, it is also important to have the light from the whole calorimeter read by a single photodetector. To fulfil these requirements, one out of every two fibres is sent to a single photodetector (PMTc) and the remaining fibres to four different photodetectors (PMT1 to PMT4) collecting the light from the four towers. The connections of the fibres to the different photodetectors are shown in Fig. 3.11 and 3.12.

**Proton calorimeter (ZP)**

The design of the proton calorimeter is similar to that of the neutron one. The main constraint in this case comes from the need to optimize the detection of the spectator protons, which are spread over the horizontal coordinate by the separator magnet. One of the PMTs collects the light of half of the fibres uniformly distributed inside the calorimeter. With the remaining fibres four towers are defined ($5.2 \times 12$ cm$^2$ each), read

out by four PMTs. The schematic arrangement of the fibres is shown in Fig. 3.13.
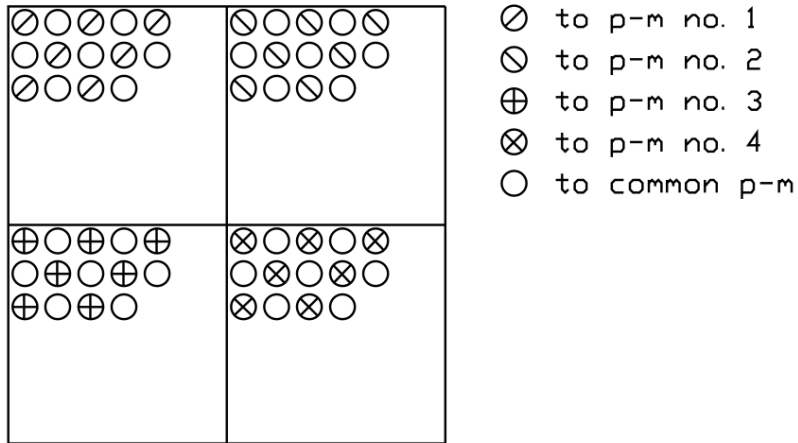


Figure 3.11: Schematic connections of the fibres to the PMTs for the neutron calorimeter.
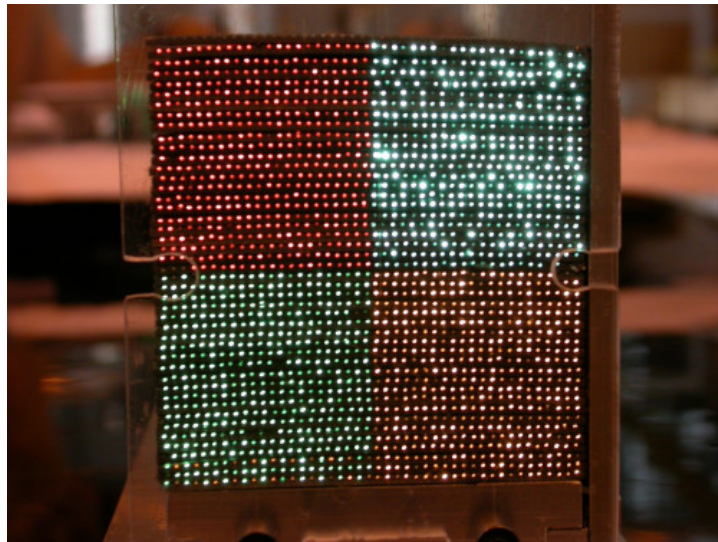


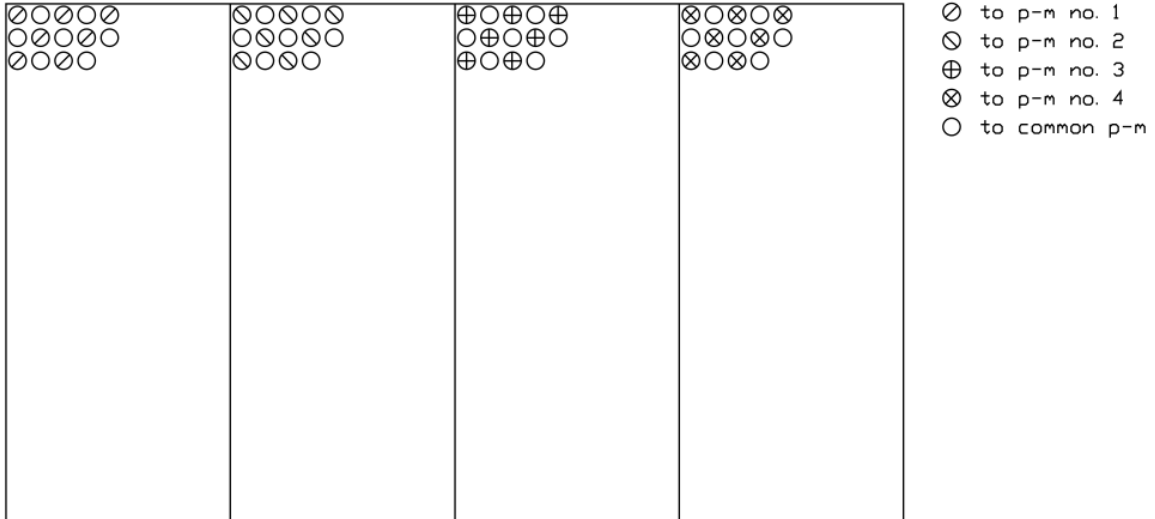Figure 3.12: Picture of a Zero Degree Calorimeter for neutrons.

Figure 3.13: Schematic connections of the fibres to the PMTs for the proton calorimeter.

**Electromagnetic Calorimeters (ZEM)**

Further information on the centrality of the collision can be provided by an electromagnetic calorimeter (ZEM), which detects, event-by-event, the energy carried by photons in the forward direction. The ZEMs are two small electromagnetic calorimeters, placed at about 7 m from the IP, on both sides of the LHC beam pipe, on the opposite side with respect to the muon spectrometer. As the other ZDC, they are quartz-fibre sampling calorimeters, with passive element absorbers. The ZEM are used in particular to discriminate between events with different centrality by measuring the energy of the particles emitted at forward rapidity that increases with the collision centrality.

## 3.3.2 ZDC Performance

As we mentioned, the ZDC are born measure the energy carried away by the non-interacting nucleons (spectators) in Pb-Pb collisions, that is the measurable quantity directly related with the centrality of the collision. However, in the colliders the correlation between impact parameter and ZDC response is not exactly monotonic. In fact, unlike fixed target experiments, in central collisions a small amount of energy is deposited in the ZDC, but similarly it could be the case for very peripheral collisions,

where spectator nucleons can bound into fragments which do not get out from the beam pipe and cannot be detected from the hadronic calorimeters. In this case the information provided by the electromagnetic calorimeter ZEM is used to remove the ambiguity between central and peripheral collisions. The Fig. 3.14 shows the ZDC energy as a function of the ZEM amplitude for 4 centrality bins selected by V0 amplitude.
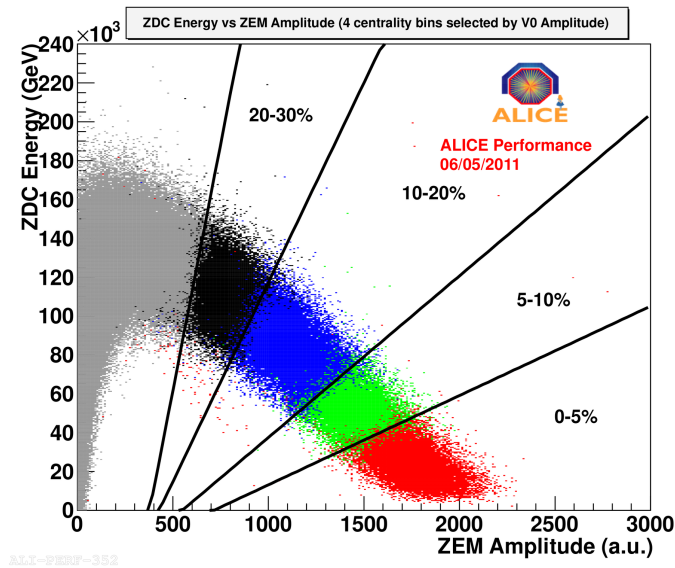


Figure 3.14: ZDC energy as a function of the ZEM amplitude for 4 centrality bins selected by V0 amplitude.

It is important to note that the resolution on the measurement of the centrality depends not only on the fluctuations in the number of spectators, but also on the precision these detectors can achieve on the energy measurement. The energy resolution on the measurement of spectators in the ZDC at a certain centrality must be at most of the same order of magnitude as the intrinsic resolution due to fluctuations on $N_S$. From the simulation of the ALICE ZDC for a single 2.7 TeV incident neutron or proton, the resolution of the calorimeters is estimated to be $\sim 11\%$ [70].

### 3.3.3 Measuring the leading effect with the ZDC

In the previous chapter the concept of leading effect was introduced. This phenomenon consists in a high probability to emit a forward baryon with large longitudinal momentum along the direction of the incident beams, which carries away a fraction of the incident primary energy and therefore reduces the "effective" energy available for particle production. We mentioned that one way of estimating the effective energy could be on an event-by-event basis by measuring the energy of the leading baryon ($E_{leading}$) in each event hemisphere (Eq. 2.2), but this kind of analysis requires a detector able to measure particles with large longitudinal momenta. ALICE has a good capability for this kind of measurement thanks to its Zero-Degree Calorimeters, which, even though optimized for Pb-Pb collisions, have a sufficient energy resolution in the forward region to make possible a pp data analysis in terms of "effective energy". Many measurements have been made in order to check if the ZDC can measure the energy of forward-going nucleons over an sufficiently extended $x_{\mathrm{F}}$ range and the conclusion is that these detectors can be used to measure leading particles in pp collisions in a wide range of energies. In particular, in the ALICE Physics Performance Report [71] it was stated that for charged particles measured in the ZP, the beam optics constraints the energy interval between 2.2 TeV and 4.5 TeV, corresponding to a Feynman-x range $0.30 < x_{\mathrm{F}} < 0.64$, with the $x_{\mathrm{F}}$ defined as in Eq. 2.4. For neutral particles, the beam optics effects are not present and the ZN accepts all particles emitted in a cone of 0.3 mrad around the beam direction [71]. In order to test the ZDC capabilities, a PYTHIA event generator was used to generate pp collisions, that were then exploited to perform a complete study of charged multiplicity and leading particle production. Figure 3.15 shows $N_{ch}$ as a function of $E_{eff}$ at generation level and after reconstruction using the ZDC. The results are consistent, indicating that the limitations related to the reconstruction of the effective energy in the ZDC and the background from other particles in the forward region do not introduce a significant bias in the measurement. The good agreement confirms that an analysis of pp events in terms of the effective energy is possible [40].
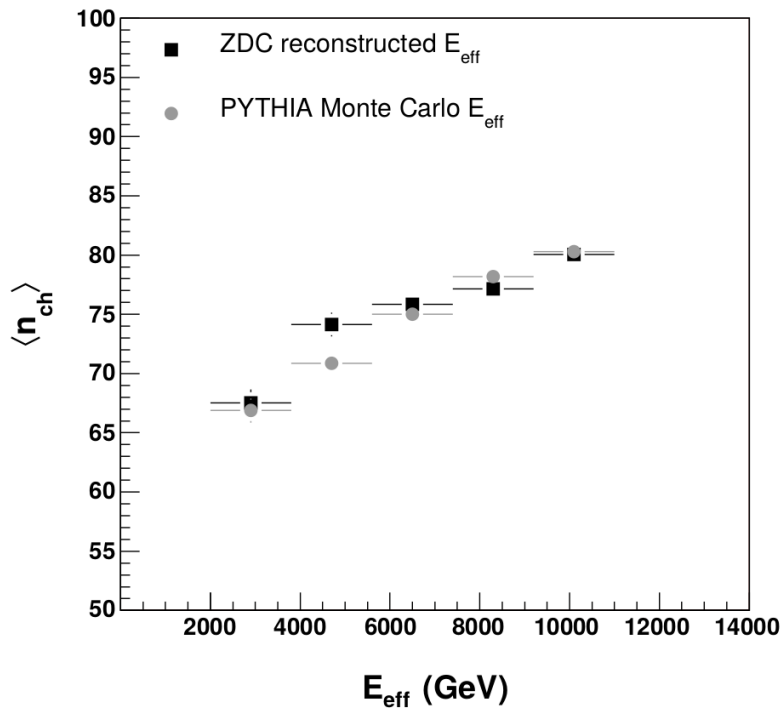
Figure 3.15: Correlation between mean charged multiplicity and mean effective energy in PYTHIA pp events, using the leading energy measurement of the ZDC calorimeter (squares). The dots are the same quantities estimated at the generator-level [40].

# Chapter 4

# Strangeness enhancement with multiplicity and effective energy

The previous chapters extensively described the ALICE experiment and its physics goals. As mentioned, this detector was built to focus on physics of strongly interacting matter at extreme energy densities, exploiting the unique physics potential of heavy-ion collisions (A-A). However in the last years of LHC activity a deeper look into hadron interactions showed that also p-Pb and pp high-multiplicity events exhibit some features similar to Pb-Pb, opening new scenarios to search for medium effects in smaller systems. In fact the understanding of particle production in pp interactions is crucial to separate genuine QGP signatures from cold nuclear matter effects in Pb-Pb and it is also interesting on its own when looking at possible hints for medium effects in small systems.

## 4.1   Motivation

In a recent paper published in 2017 [1] the ALICE Collaboration presented some interesting results regarding strangeness production in pp and p-Pb collision systems at $\sqrt{s}$ = 7 TeV and $\sqrt{s_{NN}}$ = 5.02 TeV respectively. In the first chapter it was explained how at fixed collision energy the production mechanisms of the strange quark are different between pp and A-A colliding systems. The former produces a Hadron Gas (HG), where quarks and gluons are confined, while the latter forms the QGP, where the degrees of freedom are at partonic level, with free quarks and gluons. The energy needed to produce strange mesons or baryons in a thermally equilibrated HG is significantly higher than in

the case of QGP and therefore the production of these hadrons in HG would be much more difficult. The signature of the formation of QGP known as strangeness enhancement lies exactly on the overabundance of strangeness production in a QGP scenario (A-A collisions) with respect to a HG scenario (pp collisions). The results mentioned above (ref. [1]) presented a study on strangeness production in pp and p-Pb collision systems and compared the results with Pb-Pb interactions data. The results show how the strangeness production in these collision systems increases with the event multiplicity with a similar trend to Pb-Pb data, in particular when increasing the strangeness content in baryon composition (i.e. it is larger for $\Omega$ than for $\Lambda$), as clearly visible in Figure 4.1.



ALI-PUB-106886
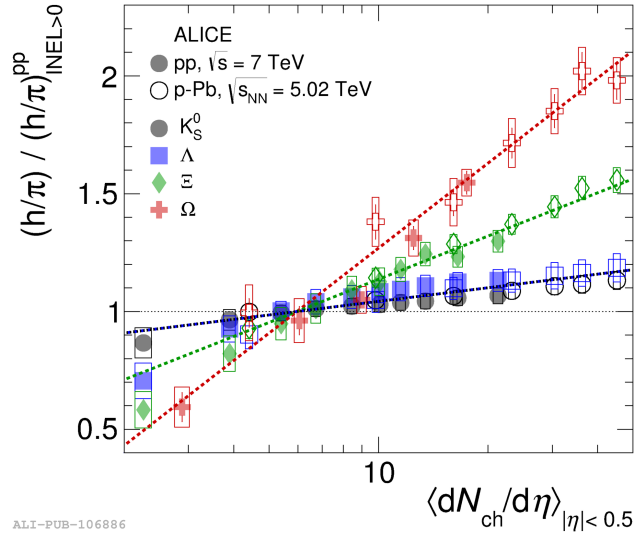
Figure 4.1: Particle yield ratios to pions normalized to the values measured in the inclusive INEL>0 pp sample, i.e. inelastic events with at least one particle track in the central barrel. The results are shown for pp and p-Pb collisions, both normalised to the inclusive INEL>0 pp sample [1].

The observed strangeness enhancement might point out some universal QCD properties and opens a large discussion on the origin of such observations. As a matter of fact this result offers a great chance to investigate possible hints for medium effects in small systems in order to improve our understanding of the underlying QCD mechanisms in hadron interactions. One of the main conclusions reported in the abstract of [1] is that

the unexpected phenomenon should be related to the final system created in the collision, i.e. to the charged particle multiplicity produced. The dependence of this variable on the center of mass energy is in fact characteristic of the final state of an interaction. However, such a statement may not be straightforward when taking into account the considerations presented in the second chapter of this thesis. Many results were introduced showing how the charged particle multiplicity in pp collisions is strongly correlated with the initial effective energy available for the interaction, which is reduced with respect to $\sqrt{s}$ due to the so-called "leading effect". Given the strong relation between these two quantities, the origin of the strangeness enhancement with multiplicity in smaller systems may be related either to the final state of the system or to the initial phase of the collision, i.e. to the energy available for particle production. The purpose of this thesis is to resolve this ambiguity regarding the origin of the enhanced production of strange particles observed in pp interactions [1], exploiting the ability of ALICE ZDC to cover the most forward rapidity particles, candidates for leading baryons. The main goal of this analysis is therefore to compare the dependence of strange particle production on multiplicity and effective energy, proposing a double-differential analysis in order to study the strangeness enhancement in different energy and multiplicity ranges.

## 4.1.1 Analysis strategy

The analysis will be organized in the following steps:

- **Event selection, multiplicity and effective energy estimation**: the first step will be to find on which data sample from pp collisions at $\sqrt{s} = 13$ TeV focus this analysis. Such samples must contain good quality information from the ZDC. Then in order to study the enhancement as a function of charged-particle multiplicity and effective energy one must define the corresponding estimators through the information available from ALICE subdetectors.

- **Track selection and signal extraction**: the following phase will be to select, among the reconstructed charged particles, the candidates for strange baryons ($\Lambda$) and multi-strange baryons ($\Xi^-$ and $\Omega^-$) and the corresponding antiparticles. Such selections will allow to extract the invariant mass of the hadron candidates from their weak decay products and to study such distributions as a function of $p_T$ in different effective energy and multiplicity ranges, obtaining the so-called raw $p_T$ spectra.

- **Efficiency correction**: the raw spectra obtained as described above are still subject to all the inefficiencies and the acceptance limitations of the detector and must therefore be corrected for these effects and normalized to the number of events, obtaining the so-called corrected spectra.

- **Integrated yields and single-differential analysis**: the $p_{\mathrm{T}}$ integrated yields will be computed from the corrected spectra in the measured ranges and using a fit extrapolation for the unmeasured regions. Then it will possible to analyse the dependence of strange particle production on the effective energy and on the charged particle multiplicity singularly.

- **Double-differential analysis**: in order to conclude whether the strangeness enhancement observed is due to an initial or final state effect, the strange particle production will be studied as a function of multiplicity in different energy ranges, and as a function of effective energy in different multiplicity ranges.

## 4.2 Data analysis

### 4.2.1 Data sample and event selection

The analysis was performed on pp collision data at $\sqrt{s} = 13$ TeV collected in 2015, 2016, 2017 and 2018 with the ALICE experiment. In order to efficiently exploit the information on the effective energy given by the ZDC, it was necessary to perform a quality check on the possible useful runs performed during these years. On top of all, it was mandatory to require the Zero Degree Calorimeters to be active during the data taking. The full sample, found to fulfil the requirements on ZDC needed for this analysis, consists of 75 runs for a total statistic of $4.6 \cdot 10^8$ events. The data were collected using a minimum-bias trigger requiring a hit in either the V0 scintillators or in the SPD detector, in coincidence with the arrival of proton bunches from both directions. The events selected are further required to have a reconstructed primary vertex (PV) within $|z| < 10$ cm to ensure good rapidity coverage and uniformity for the particle reconstruction efficiency in the ITS and TPC tracking volume. Further off-line selections are applied, some of which based on pile-up rejection. Monte Carlo productions have also been considered in order to be able to correct the real data for efficiencies. The productions used simulations generated

with PYTHIA8, anchored to 69 runs[1] from real data inside our sample, with particle transport performed via a GEANT3 simulation of the ALICE detector.

## 4.2.2 Multiplicity estimators

A crucial role in this analysis is played by charged-particle multiplicity and its dependence on effective energy and strange particle production. In particular, in this thesis the multiplicity was extracted exploiting two estimators:

- Reference multiplicity: calculated using the information of the reconstructed charged particles in the central barrel, at mid-rapidity. As a first step, the global tracks reconstructed by ITS + TPC are considered, then complementary tracks found with ITS only information are included. The last step includes all the so-called *tracklets*[2], found between the SPD layers, that are not matched to tracks counted in the previous steps (complementary tracklets).

- V0 multiplicity: provided by the V0 detectors (V0C and V0A). As mentioned in the previous chapter, one of the most important roles of the V0 system is in fact to provide a charged particle multiplicity measurement based on the energy deposited in its scintillators. Using a detailed simulation of the apparatus, the relation between the total charge collected inside a V0 ring and the number of primary charged particles collected in the central barrel in the corresponding pseudorapidity range can be extracted. The distribution of the V0 amplitudes, as a sum of V0C and V0A contributions, can then be grouped in percentiles of the selected events: this allows to classify the events in multiplicity classes.

## 4.2.3 Effective energy estimators

As we stated, the purpose of this thesis is to study the enhanced production of strange particles observed in pp interactions, as a function of multiplicity and effective energy. This analysis exploits the ability of ALICE ZDC to cover the candidates for leading baryons and therefore to estimate the energy effectively available for particle production through the energy deposits in the calorimeters. Chapter 3 analysed in detail the functions and the structure of the Zero Degree Calorimeters. As mentioned, one neutron

---

[1]For 6 runs out of the whole sample of 75, it was not possible to find a Monte Carlo simulation.

[2]Tracklets are defined as pairs of hits in the two SPD layers aligned with the primary vertex.

(ZN) and one proton calorimeter (ZP) are placed in the forward region on both sides of the interaction point (each side is referred to respectively as anticlock-wise A and clock-wise C). The optical readout of each calorimeter is divided into four independent towers each connected to a photodetector (single channels). However the light is also read through a global signal such that one out of every two scintillator fibres is sent to a single photodetector (common channel). This set-up is useful both to monitor the possible relative damage to the different sections of the detector and to make the calibration easier. In this configuration, if the calorimeters are calibrated, the sum of the signal from the 4 towers of each detector (referred to as *ZDC Channels Sum*) should equal the signal from the common photodetector ($ZDC_{common}$) (as visible in Fig 4.2).



(a) $ZP^C$ calorimeter.

(b) $ZP^A$ calorimeter.
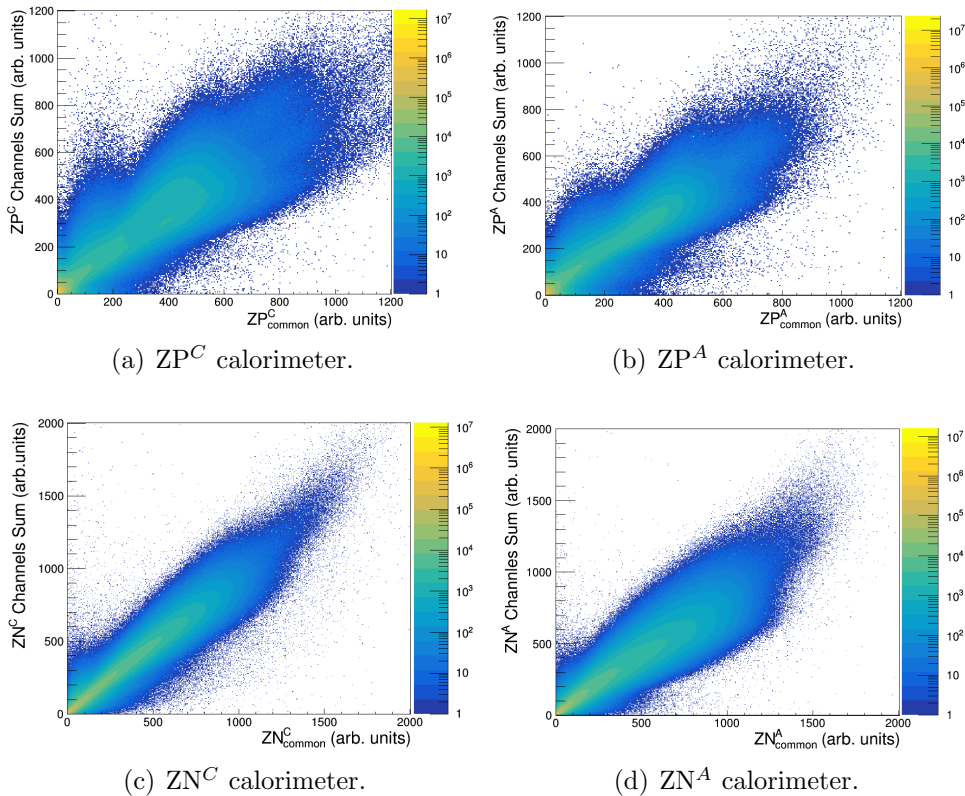
(c) $ZN^C$ calorimeter.

(d) $ZN^A$ calorimeter.

Figure 4.2: Correlation between the sum of the signal from the 4 towers of each calorimeter (referred to as *ZDC Channels Sum*) and the signal from the common photodetector ($ZDC_{common}$) for all 4 hadron calorimeters: $ZP^C$ (a) $ZP^A$ (b) $ZN^C$ (c) $ZN^A$ (d).

Some quality check on the ZDC signal were performed before starting the analysis in order to make sure the events selected contained good quality information from the forward

calorimeters. The variable used to classify the events as a function of effective energy will be referred to as *ZDC Energy Sum* and corresponds to the sum of the energies collected by all hadron Zero Degree Calorimeters in the common channel:

$$ZDC\ Energy\ Sum = ZN^{C}_{common} + ZN^{A}_{common} + ZP^{C}_{common} + ZP^{A}_{common} \quad . \qquad (4.1)$$

Figures 4.3 (a) and (b) show the correlation between $V0\ amplitude$ and $ZDC\ Energy\ Sum$, confirming the correlation expected from previous results.
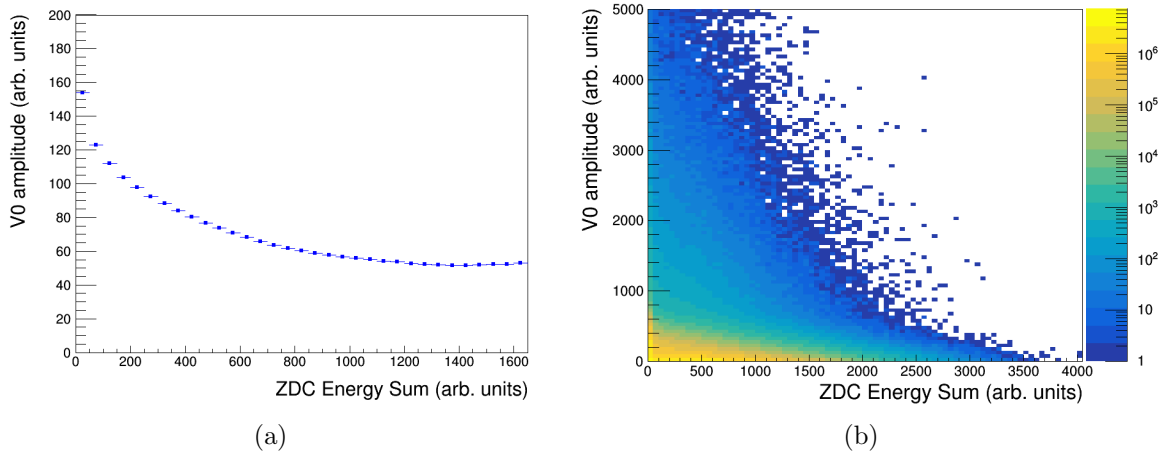


(a)                    (b)

Figure 4.3: Correlation between charged particle multiplicity, estimated using ALICE V0 detectors, and the energy deposit in the ZDC.

In order to classify the events in ZDC energy classes similar to that obtained for multiplicity using the V0 detector one must first consider how the *ZDC Energy Sum* is related to the effective energy and the multiplicity of the event. A high energy deposit in the calorimeters means a strong contribution of the leading effect and therefore low effective energy and particle multiplicity production. On the other hand a low energy deposit in the ZDC is related to a high particle production in the event and effective energy registered. The distribution of the *ZDC Energy Sum* variable on the full statistic is shown in Fig. 4.4. The events are grouped in percentile classes which reflect the fraction of events in each region over the total events.

In order to obtain the percentile classes displayed in Fig 4.4 one must consider the fraction of entries in each bin of the distribution over the total number of events. This fraction is summed recursively in order to produce a cumulative distribution, as shown

in Fig. 4.5 (a). Given the cumulative it is possible to interpolate the ZDC energy deposit in each event and associate it with a ZDC value in percentiles. The distribution of ZDC percentiles on the complete statistic is visible in Fig 4.5 (b), showing a homogeneous distribution over the total events. Such a variable is presented for the first time in this thesis and it will be crucial even in future analyses in order to study particle production in pp collisions as a function of effective energy under the leading effect hypothesis.
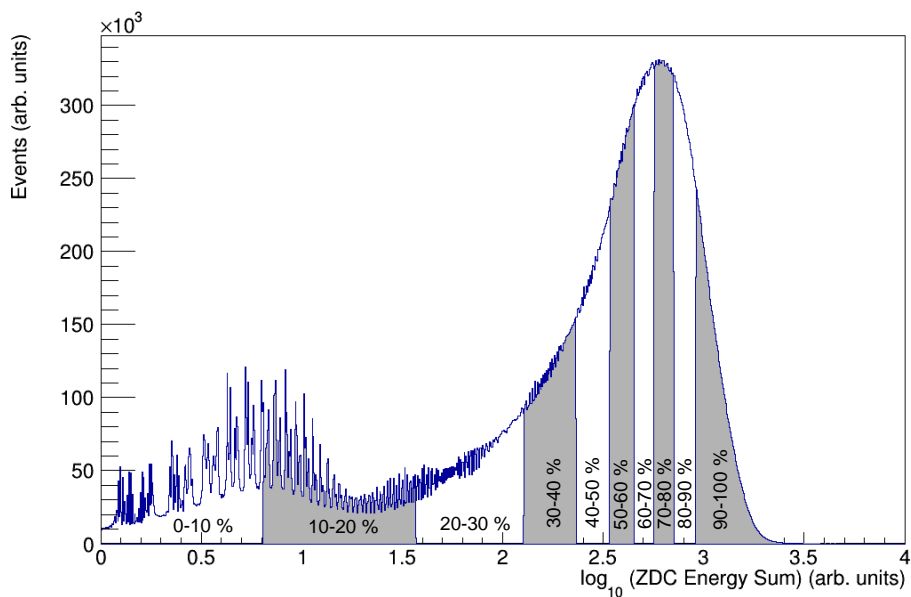


Figure 4.4: Distribution of the *ZDC Energy Sum* variable for the total event sample analysed in this thesis. The events are grouped in percentile classes which reflect the fraction of events in each region over the total number. The pseudo-peaks visible in the region marked as 0-20 %, are fluctuations on the small energy deposit in the ZDC, which are almost empty in that range.

The effective energy estimator *ZDC percentile* and the multiplicity estimator *V0 percentile* will be used in this analysis in order to group the events in classes. The definitions of these estimators are built such as low *ZDC percentile* and *V0 percentile* values correspond to high energy available for particle production and high charged-particle multiplicity.
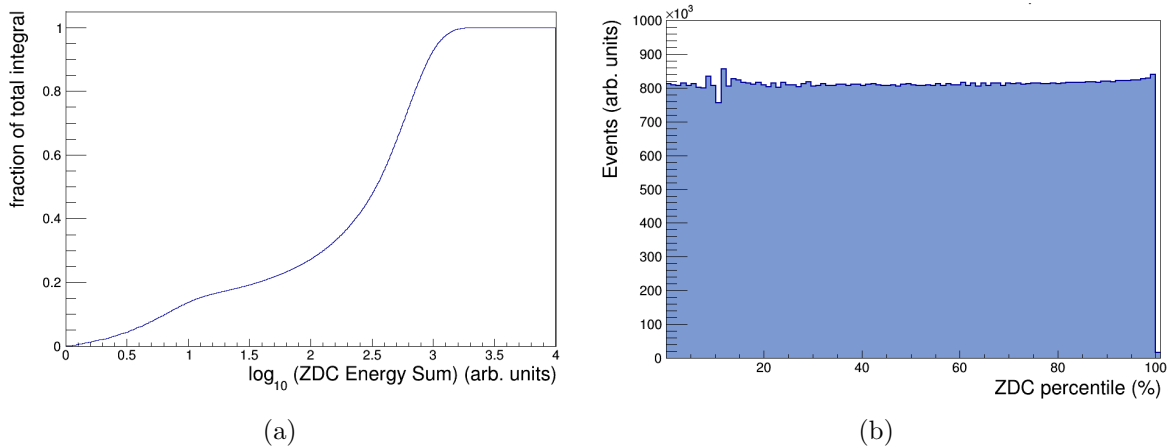
Figure 4.5: (a) Cumulative distribution of the fraction of events in each bin of the distribution in Fig. 4.4 over the total number of entries. (b) ZDC percentile variable distribution for all events.

## 4.2.4 Track selection

ALICE is able to identify particles with momenta from $0.1 \, \mathrm{GeV}/c$ up to a several $\mathrm{GeV}/c$. To accomplish that, the experiment exploits different techniques using its PID detectors, invariant mass distributions and topological methods. The ITS, TPC, TRD, TOF and HMPID are crucial detectors for particle identification in ALICE. They make use of different PID techniques to provide charged particle identification over a set of complementary $p_\mathrm{T}$ ranges. In this analysis we are especially interested in strange and multi-strange baryons containing one, two or three strange quarks such as $\Lambda$(uds), $\Xi^-$(dss), $\Omega$(sss) and the corresponding antiparticles. As described in Chapter 3, only charged particles can be tracked and identified using the ALICE detector, as a consequence the $\Xi^0$(uss) baryon, (whose most probable decay channel is $\Xi^0 \to \Lambda + \pi^0$), and the corresponding antiparticle, cannot be directly identified. The main characteristics of the $\Xi$ and $\Omega$ charged hyperons, the $\Lambda$ baryon and their charge conjugate are reported in Table 4.1.

In this analysis, the identification of these particles is accomplished at mid-rapidity ($|y| < 0.5$) via *topological reconstruction* of their weak decay inside the restricted volume of the tracking detectors, i.e. the particle association is based on geometrical and kinematical criteria. It is customary to divide these objects into two main topological classes:

- V0 topology: such as $\Lambda$ and $\mathrm{K}^0_S$, characterized by their V-shaped decay topology.

69

- Cascade topology: such as $\Xi$ and $\Omega$, which decay into a charged meson (*bachelor*) and a $\Lambda$, which further decays into a proton and a pion.
  Since the reconstruction requires the detection of the three charged daughter tracks, these are known as cascades.

| Particle | Mass (MeV/$c^2$) | Decay channel | B.R.(%) | $c\tau$ (cm) |
|:---:|:---:|:---:|:---:|:---:|
| $\Lambda$ (uds) | $1115.683 \pm 0.006$ | $\Lambda \rightarrow p + \pi^-$ | $63.9 \pm 0.5$ | 7.89 |
| $\bar{\Lambda}$ ($\bar{u}d\bar{s}$) | $1115.683 \pm 0.006$ | $\bar{\Lambda} \rightarrow \bar{p} + \pi^+$ | $63.9 \pm 0.5$ | 7.89 |
| $\Xi^-$ (dss) | $1321.71 \pm 0.07$ | $\Xi^- \rightarrow \Lambda + \pi^-$ | $99.887 \pm 0.035$ | 4.91 |
| $\bar{\Xi}^+$ ($\bar{d}\bar{s}\bar{s}$) | $1321.71 \pm 0.07$ | $\bar{\Xi}^+ \rightarrow \bar{\Lambda} + \pi^+$ | $99.887 \pm 0.035$ | 4.91 |
| $\Omega^-$ (sss) | $1672.45 \pm 0.29$ | $\Omega^- \rightarrow \Lambda + K^-$ | $67.8 \pm 0.7$ | 2.46 |
| $\bar{\Omega}^+$ ($\bar{s}\bar{s}\bar{s}$) | $1672.45 \pm 0.29$ | $\bar{\Omega}^+ \rightarrow \bar{\Lambda} + K^+$ | $67.8 \pm 0.7$ | 2.46 |

Table 4.1: Properties of the $\Lambda$ baryons and the $\Xi$ and $\Omega$ multi-strange baryons. The valence quark content, the mass, the main decay channel, together with their branching ratio (B.R.) and $c\tau$ are listed with the respective errors. The values are taken from [72].

The V0 finding procedure for $\Lambda$ and $\bar{\Lambda}$ starts with the selection of secondary tracks, i.e. tracks having a sufficiently large impact parameter with respect to the primary vertex. All possible combinations between two secondary tracks of opposite charge are then considered and they are accepted as V0 candidates only if the Distance of Closest Approach (DCA) between them is smaller than a selected value. Charged particles, compatible with kaon, pion and proton hypotheses, are identified using their energy loss in the TPC. The V0 vertex position is defined as the point where the two tracks have the closest approach. Once their position is determined, only the V0 candidates located inside a given fiducial volume are kept[3]. Finally, the V0 finding procedure checks whether the particle momentum ($p$) associated with the V0 candidate points back to the primary vertex by applying a cut on the cosine of the angle between $p$ and a vector connecting the primary vertex and the V0 position (pointing angle $\theta_p$). The invariant mass of these candidates can then be calculated either under the p($\bar{p}$) and $\pi^-$ ($\pi^+$) hypotheses.

---

[3]Further information on the specific values selected are given in Appendix A.

After finding V0 candidates, the search for the cascade decays is performed and it consists of a V-shaped decay of the daughter Λ plus a negatively or positively charged track (*bachelor*). A V0-bachelor association is performed if the DCA between the bachelor track and the V0 trajectory is less than a fixed value. Finally, this cascade candidate is selected if its reconstructed momentum points back to the primary vertex using the cosine of cascade pointing angle. The cascade finding is limited to the fiducial region used for V0 reconstruction. The search for secondary vertices from particle decays is performed as shown in Fig. 4.6 with $K_S^0$ and $\Xi^-$ decays shown as an example. More details regarding track reconstruction can be found in [73].
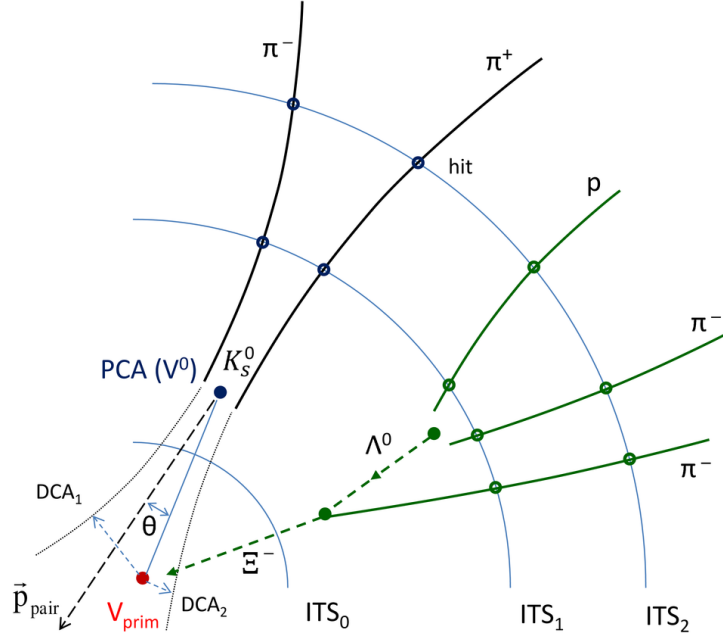


Figure 4.6: Secondary vertex reconstruction principle, with $K_S^0$ and $\Xi^-$ decays shown as an example. The solid lines represent the reconstructed charged particle tracks, extrapolated to the secondary vertex candidates. Extrapolations to the primary vertex and auxiliary vectors are shown with dashed lines.

The restrictions on the topology of V0s and Cascades decays chosen to select candidates in this analysis are summarized in Tables A.1 and A.2 (appendix A) , together with few more general selections. For V0s, in order to ensure that only high-quality candidates are selected, a set of track quality requirements on the TPC detector is applied together with an additional set of geometrical requirements to ensure that the tracks are configured in space consistently with the expected V0 decay topology. Also the Cascade candidates

selected for the analysis must comply with a number of track quality and topological selections in order to make sure that the geometrical characteristics of the tracks are consistent with the expected cascade decay topology. The variables used for topological cuts are displayed in Fig. 4.7 for a visual representation of the selections in Tables A.1 and A.2 (appendix A).
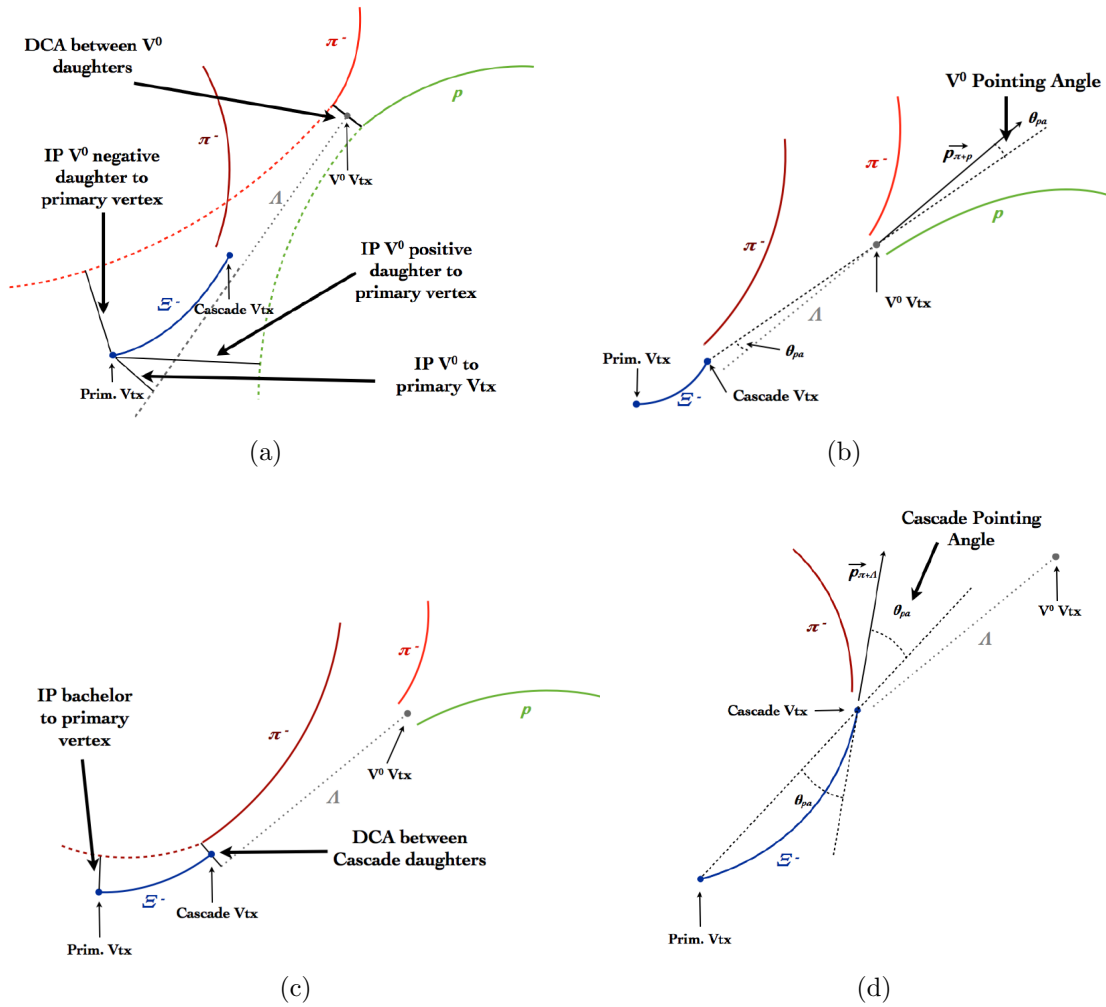


Figure 4.7: Pictorial representation of the topological variables used to identify the cascade, similarly defined for the V0.

## 4.2.5 Signal extraction and background evaluation

After the reconstruction, the invariant mass of each candidate can be calculated under the V0-daughters or V0-daughters+bachelor hypothesis, through the TPC PID information on energy and momentum of the particle. In order to extract the yields of strange and multi-strange baryons the invariant mass of each candidate is studied as a function of the transverse momentum ($p_T$) in different multiplicity and ZDC energy classes. In each selected $p_T$ range, the invariant mass distribution is first approximated by a Gaussian with a second order polynomial shaped background for both V0 candidates and Cascades. The resulting invariant mass distributions for both topological class hypotheses are shown in Fig. 4.8 for one exemplary range in $p_T$.

The invariant mass peak is fitted in a selected mass range and the background is later subtracted obtaining the particles yields by integrating the Gaussian peak. Once the signal extraction and background subtraction are done, the so-called raw spectra can be obtained as a function of $p_T$. The yields in each $p_T$ range are divided by the bin width and normalized to the rapidity interval $|y| < 0.5$ to obtain the raw $p_T$ spectra: $d^2 N^{raw}/dy dp_T$ ($p_T$). Through this method, different raw spectra for each multiplicity and ZDC energy classes are produced. These are still subject to all the inefficiencies and the acceptance limitations of the detector and must therefore be corrected for these effects and normalized to the number of events.

## 4.2.6 Efficiency corrections

The efficiencies corrections can be inferred by analysing Monte Carlo (MC) events using the same topological cuts as for real data, with the only exception that in MC V0s and Cascades candidates are further checked to match a "true" primary particle of the same type. In general, the acceptance and efficiency depend on both $y$ and $p_T$, therefore we choose the $y$ interval ($|y| < 0.5$) such that the dependence would only be related to the transverse momentum. The efficiency correction factor is computed by taking the ratio of the reconstructed V0 (Cascade) and the generated primary V0 (Cascade) in each $p_T$ interval:

$$\varepsilon = \frac{N^{part}_{reconstructed}(p_T)}{N^{part}_{generated}(p_T)} \quad . \tag{4.2}$$

The efficiencies used for this analysis are computed on all the Minimum Bias data sample. However since the analysis is performed in multiplicity intervals, an important consider-

ation is whether the detection efficiency of V0s and Cascades changes with multiplicity and this study is currently in progress. The Minimum Bias efficiencies for each particle and corresponding antiparticle are shown in Fig. 4.9, 4.10 and 4.11 as a function of $p_T$.
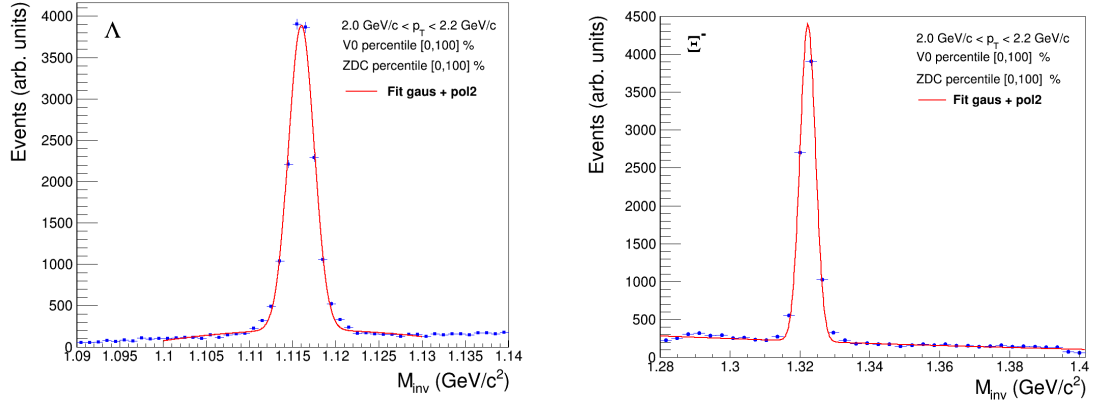


(a) $\Lambda$ invariant mass from recostructed p and $\pi^-$. Fit range (1.10-1.13) GeV/$c^2$.

(b) $\Xi^-$ invariant mass from recostructed $\Lambda$ and $\pi^-$. Fit range (1.28-1.4) GeV/$c^2$.
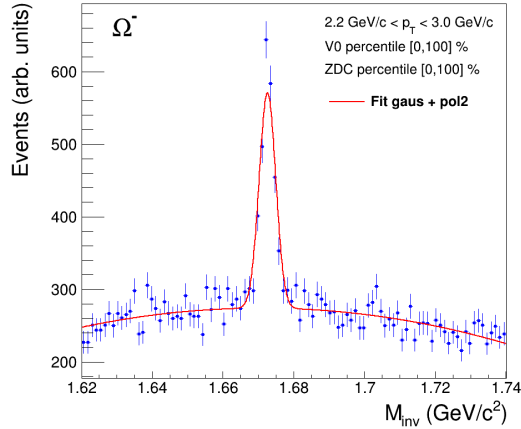


(c) $\Omega^-$ invariant mass from recostructed $\Lambda$ and K$^-$. Fit range (1.62-1.74) GeV/$c^2$.

Figure 4.8: Invariant mass distribution for $\Lambda$, $\Xi^-$ and $\Omega^-$ in different $p_T$ ranges, keeping V0 and ZDC percentile in the range [0-100]% (MB collisions).

(a)  (b)
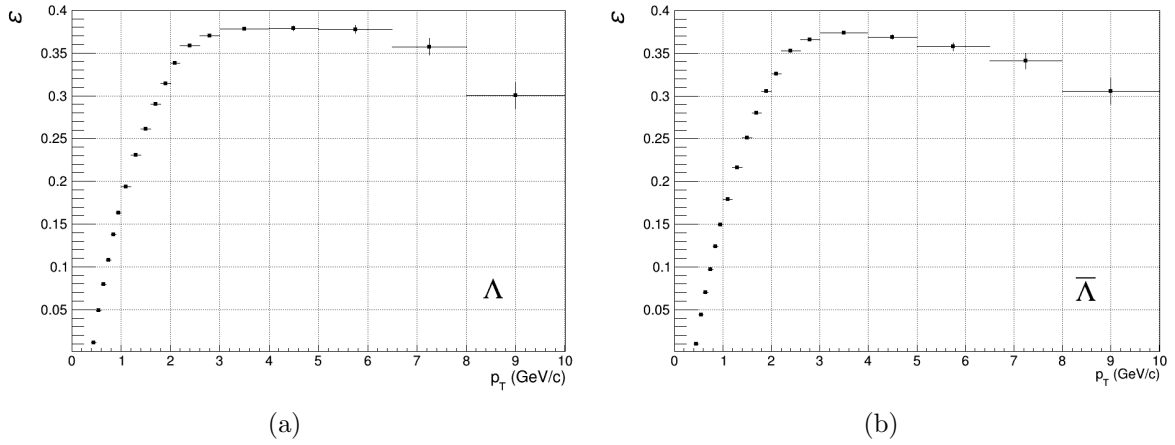
Figure 4.9: Efficiencies for $\Lambda$ (a) and $\bar{\Lambda}$ (b) computed on all the Minimum Bias data sample as a function of $p_T$.
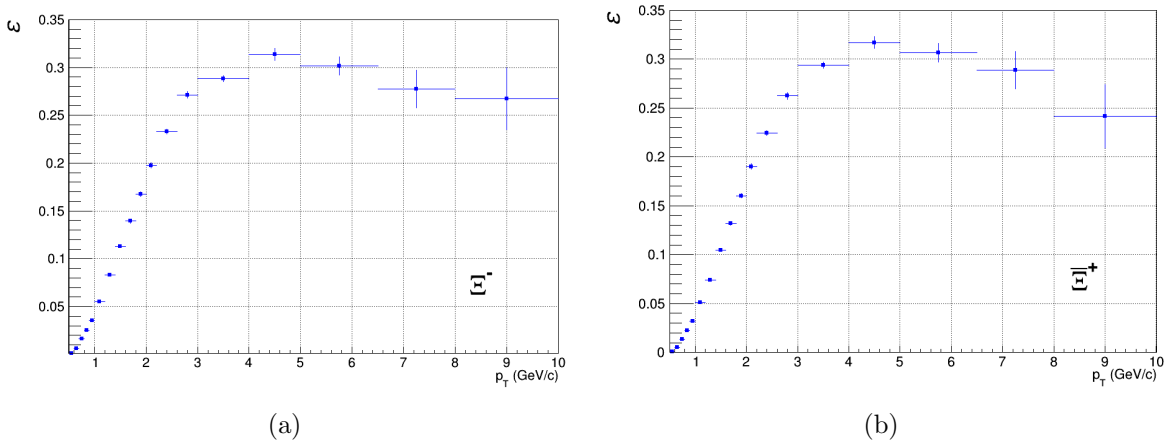


(a)  (b)

Figure 4.10: Efficiencies for $\Xi^-$ (a) and $\bar{\Xi}^+$ (b) computed on all the Minimum Bias data sample as a function of $p_T$.
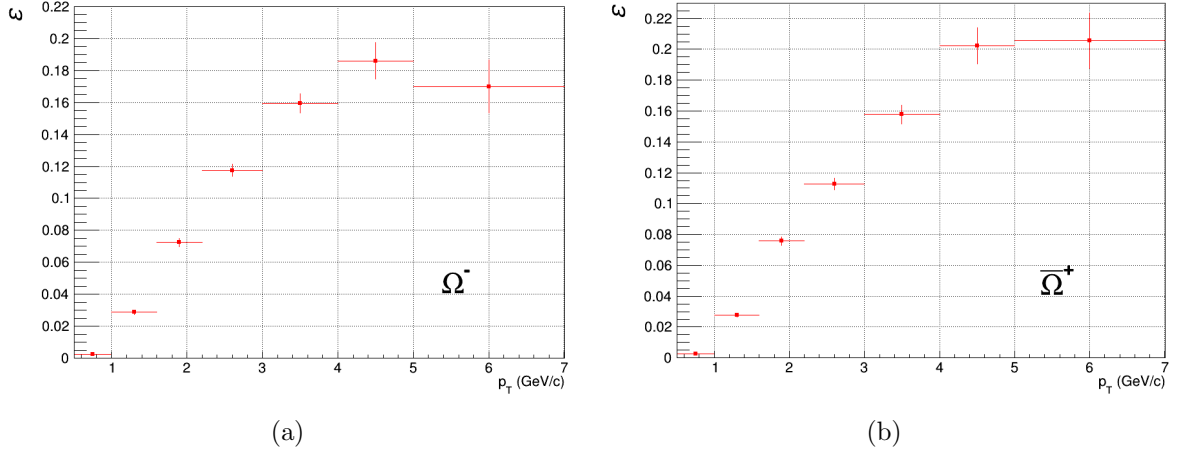
(a)                                 (b)

Figure 4.11: Efficiencies for $\Omega^-$ (a) and $\bar{\Omega}^+$ (b) computed on all the Minimum Bias data sample as a function of $p_{\mathrm{T}}$.

## 4.3 Results

### 4.3.1 Single-differential analysis

**Corrected spectra**

The raw yields obtained as described in the previous section have been corrected for the minimum bias efficiencies and normalized by the number of events. The final spectra per $p_{\mathrm{T}}$ bin per rapidity unit are then defined as:

$$1/N_{evt}\frac{d^2N}{dp_{\mathrm{T}}dy} = \frac{1}{N_{events}} \cdot \frac{d^2N^{raw}}{dp_{\mathrm{T}}dy} \cdot \frac{1}{\varepsilon_{MB}} \cdot \frac{1}{B.R.} \quad . \tag{4.3}$$

For each strange particle and antiparticle considered in this analysis the corrected spectra were computed in the V0 and ZDC percentiles classes summarised in Table 4.2.
In order to extract particle yields integrated over the full $p_{\mathrm{T}}$ range (expecially at low and very high $p_{\mathrm{T}}$), the spectra are fitted using the parametrization of the Lévy-Tsallis function[4], which gives the best description of the individual spectra for all particles and all event classes over the full $p_{\mathrm{T}}$ range:

---

[4]More details on the Lévy Tsallis function can be found in [74].

| Baryon | V0 *percentile* **classes** (%) |
|--------|------------------------------------------------|
| Λ | [0-1], [1-5], [5-10], [10-15], [15-20], [20-30], [30-40], [40-50], [50-70], [70-100] |
| Ξ | [0-5], [5-10], [10-15], [15-30], [30-50], [50-70], [70-100] |
| Ω | [0-5], [5-15], [15-50], [50-100] |
| **Baryon** | ***ZDC percentile* classes** (%) |
| Λ and Ξ | [0-10], [10-20], [20-30],[30-40], [40-50], [50-60], [60-70], [70-80], [80-90], [90-100] |
| Ω | [0-10], [10-30], [30-50], [50-100] |

Table 4.2: Multiplicity (V0) and effective energy (ZDC) classes used for each particle in this first part of the analysis.

$$\frac{\mathrm{d}^2 N}{\mathrm{d}y\mathrm{d}p_{\mathrm{T}}} = \frac{(n-1)(n-2)}{nT\left[nT + m_0(n-2)\right]} \times \frac{\mathrm{d}N}{\mathrm{d}y} \times p_{\mathrm{T}} \times \left(1 + \frac{m_{\mathrm{T}} - m_0}{nT}\right)^{-n} \quad , \qquad (4.4)$$

where $T$, $n$, and $dN/dy$ ($dN/dy$ representing the particle yield per rapidity unit) are fit parameters, $m_{\mathrm{T}} = \sqrt{m_0^2 + p_{\mathrm{T}}^2}$ , and $m_0$ denotes the particle mass. The corrected spectra as well as the Lévy-Tsallis parametrization fit are displayed in Fig 4.12, for different V0 *percentile* selections, and in Fig. 4.13 for *ZDC percentile* selections. For each strange particle analysed, Table 4.3 specifies the fit range selected in $p_{\mathrm{T}}$ and the extrapolation regions. The available statistics changes between V0s and Cascades and consequently also the fit ranges, which are selected to reflect the best quality parametrization observed.

| Baryon | Fit range in $p_{\mathrm{T}}$ (GeV/c) | Extrapolation range (GeV/c) |
|--------|-------------------------------|------------------------------|
| Λ | [0.6 - 10.0] | $p_{\mathrm{T}} > 10.0$, $p_{\mathrm{T}} < 0.6$ |
| Ξ | [0.6 - 8.0] | $p_{\mathrm{T}} > 8.0$, $p_{\mathrm{T}} < 0.6$ |
| Ω | [1.0 - 7.0] | $p_{\mathrm{T}} > 7.0$, $p_{\mathrm{T}} < 1.0$ |

Table 4.3: Fit range and extrapolation range for the corrected particle spectra in Fig. 4.12 and 4.13.
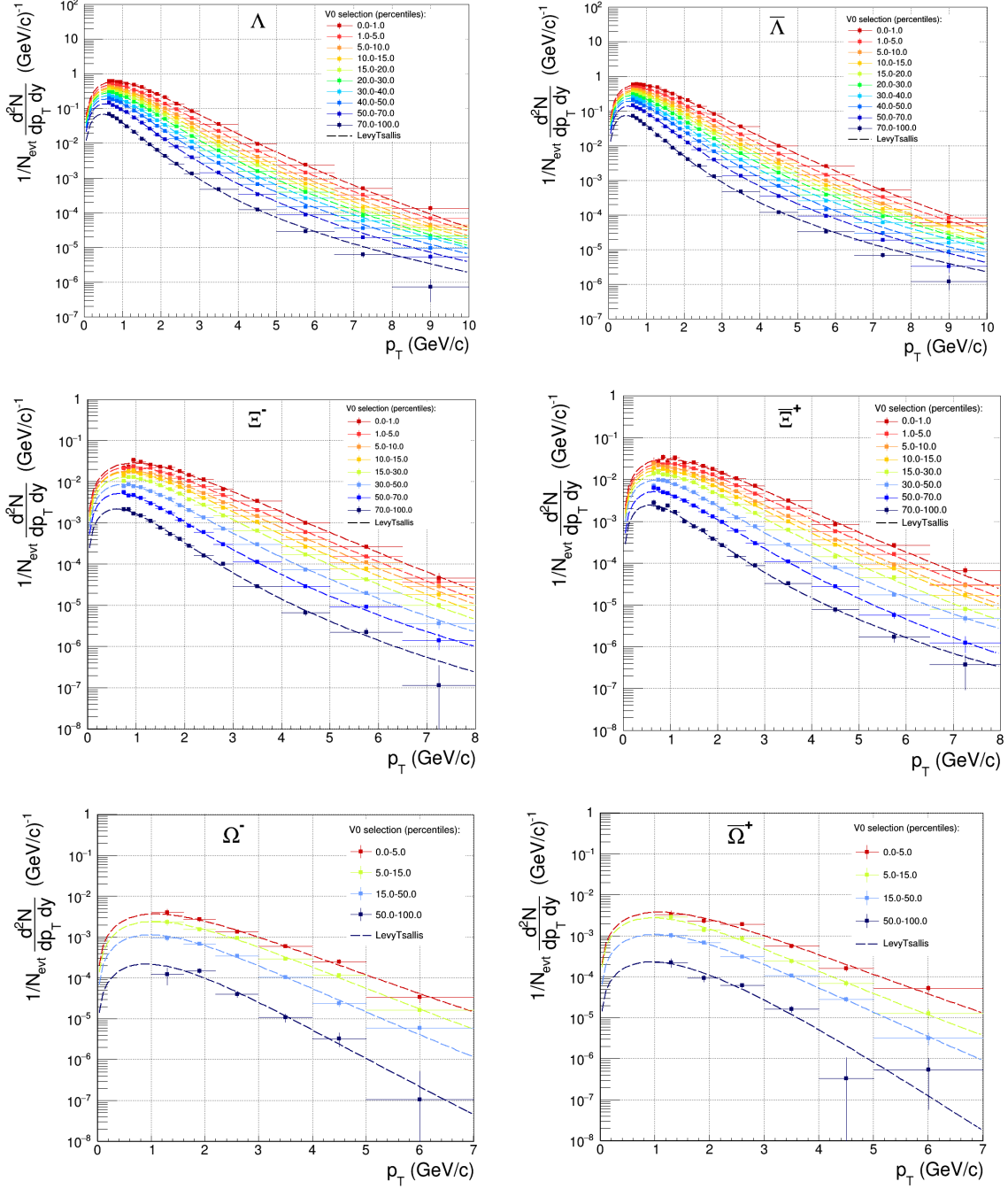
Figure 4.12: The corrected $p_T$ spectra are displayed for different $V0$ *percentile* selections showing the statistical errors. The Lévy-Tsallis parametrization fit is also displayed for each spectrum.
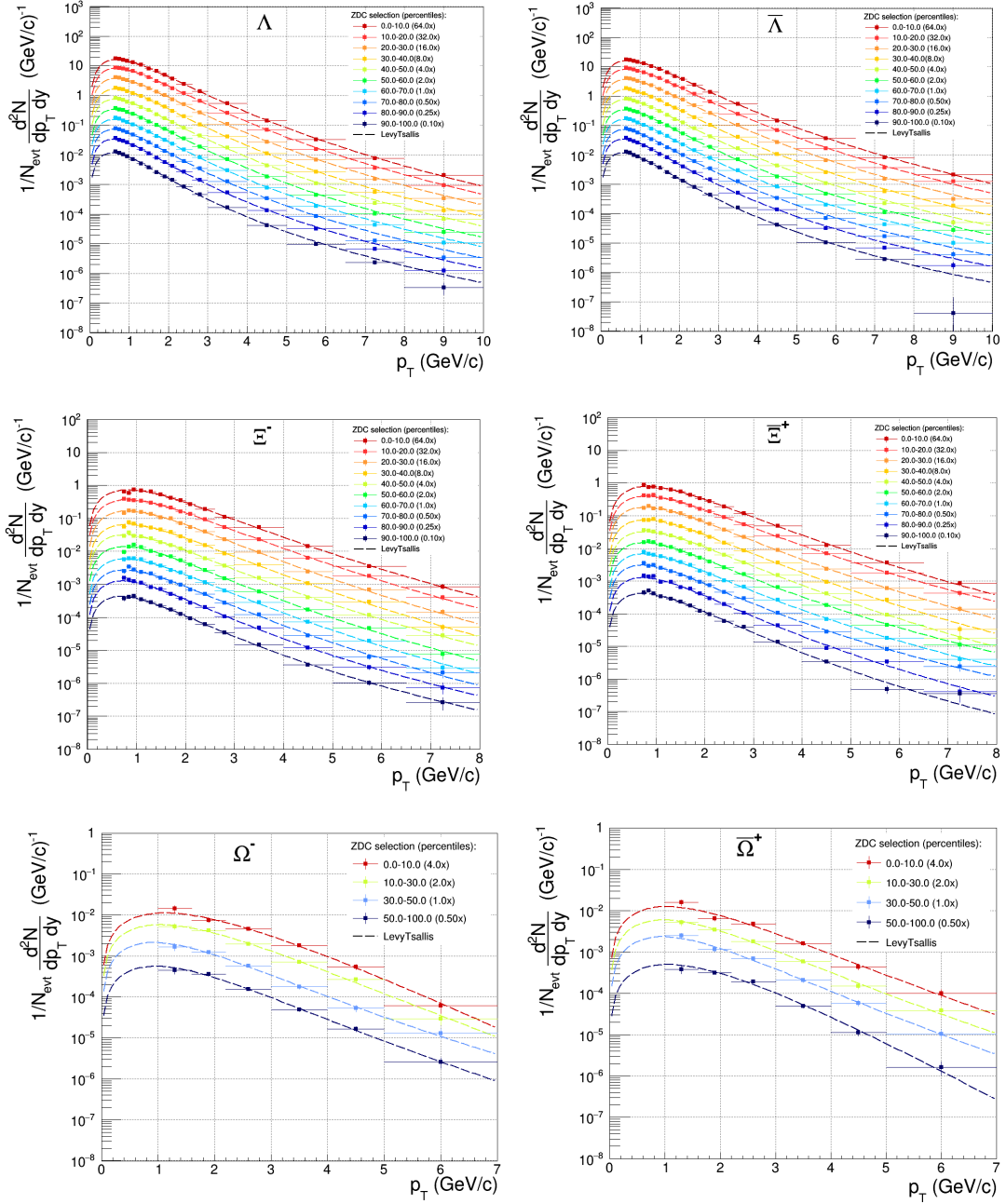
Figure 4.13: The corrected $p_T$ spectra are displayed for different *ZDC percentile* selections showing the statistical errors. The Lévy-Tsallis parametrization fit is also displayed for each spectrum.

## Multiplicity dependence of dN/dy and normalized yields

The integrated yields over the full $p_T$ range, $dN/dy$, are computed from the data in Fig. 4.12 and 4.13 in the measured ranges and using extrapolations for the unmeasured regions. The integrated yields as a function of the mean reference multiplicity $< n_{ch} >$ are shown in Fig. 4.14 and 4.15. The mean reference multiplicity is defined as the average charged-particle multiplicity measured in the central barrel, for a given V0 or ZDC selection. The error displayed are purely statistical and are calculated with the quadrature-sum method. As visible in Fig. 4.14 and 4.15 the yields of particles and antiparticles are comparable inside the statistical errors for both $ZDC$ and $V0\,percentile$ selections.
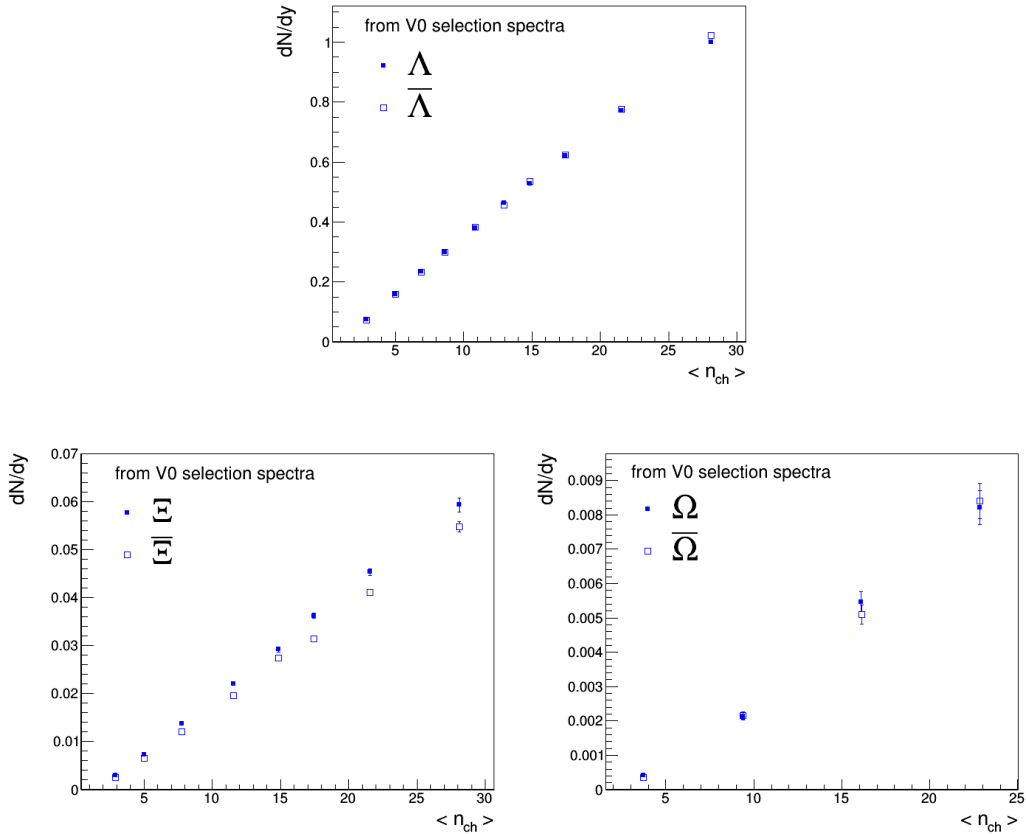


Figure 4.14: $p_T$ integrated yields, $dN/dy$, as a function of the mean reference multiplicity $< n_{ch} >$, obtained from the V0 selection spectra. The yields are computed from the data in Fig. 4.12 in the measured ranges and using extrapolations from Lévi-Tsallis parametrization fit to the unmeasured regions. The error displayed are statistical.

Figure 4.15: $p_{\rm T}$ integrated yields, $dN/dy$, as a function of the mean reference multiplicity $< n_{ch} >$, obtained from the ZDC selection spectra. The yields are computed from the data in Fig. 4.13 in the measured ranges and using extrapolations from Lévi-Tsallis parametrization fit for the unmeasured regions. The error displayed are statistical.
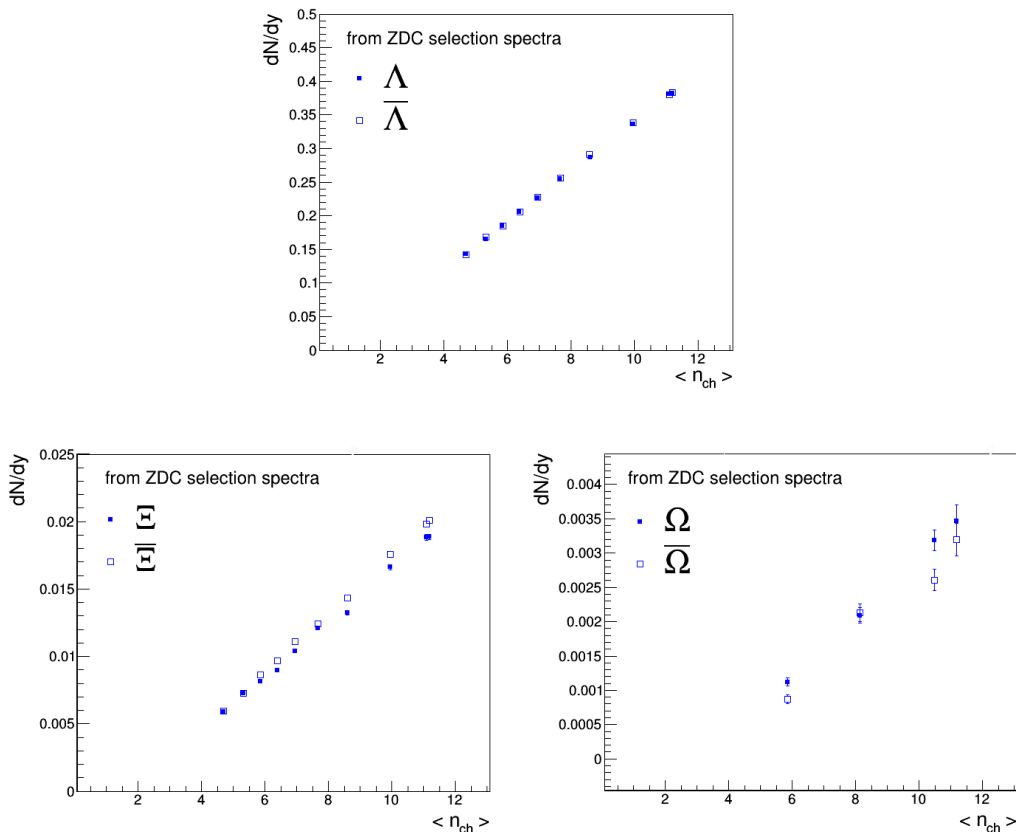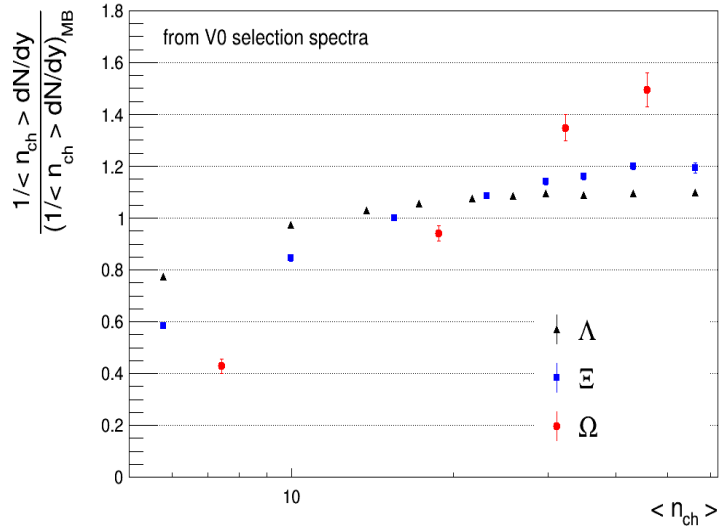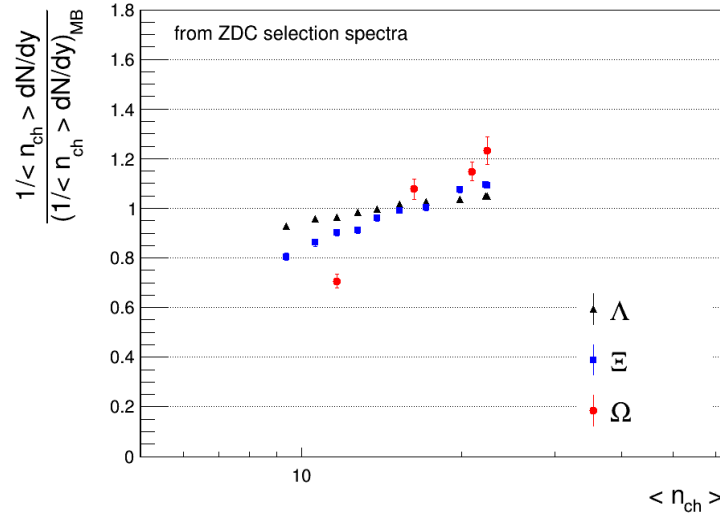
The integrated yields normalized to the Minimum Bias production and to the mean reference multiplicity ($< n_{ch} >$) are shown in Fig. 4.16 as a function of $< n_{ch} >$ for V0 (a) and ZDC (b) selection spectra. The error displayed are purely statistical and are calculated with the quadrature-sum method. Figure 4.16 (a) shows a plot similar to Fig. 4.1 from ref. [1]. Given the large statistics analysed and the higher $\sqrt{s}$ (13 TeV vs 7 TeV) this study allows to extend the explored region in multiplicity with respect to the published result. The analogous plot in Fig 4.16 (b) explores for the first time the dependence of strange particles production on the effective energy, showing the enhancement obtained from ZDC selection spectra, which covers a smaller $< n_{ch} >$

region. This plot shows an enhanced trend in particular when increasing the strangeness content in baryon composition.



(a)



(b)

Figure 4.16: Integrated yields normalized to Minimum Bias production and $< n_{ch} >$ as a function of the mean reference multiplicity for V0 (a) and ZDC (b) selection spectra. The error displayed are statistical.

## 4.3.2 Double differential analysis

The results presented in the previous sections show a good agreement with the expected enhanced strangeness production with multiplicity observed in [1] and shown in Fig. 4.1. Moreover, using pp data at $\sqrt{s} = 13$ TeV allows to extend the analysis to higher multiplicity regions as shown in Fig. 4.16 (a), and to explore the dependence of strange particle production on effective energy (Fig. 4.16 (b)). However, the final purpose of this thesis was not only to perform a study of strangeness enhancement as a function of these two quantities singularly. As it was mentioned, given the strong correlation between charged particle multiplicity and the energy available for particle production, the origin of the strangeness enhancement with multiplicity may be related either to the final state of the interaction (i.e. multiplicity) or to the initial phase of the collision (i.e. effective energy). In order to resolve this ambiguity, this thesis proposes a double differential analysis of the observed enhancement as a function of both multiplicity and effective energy. Some preliminary observations can be already made by analysing the strange baryons production, normalized to MB and mean reference multiplicity, as a function of the two estimators: $ZDC$ and $V0$ $percentile$. In this stage of the analysis, in order to be able to compare the V0 and ZDC selection classes, the corrected spectra were computed in equal $V0$ and $ZDC$ $percentile$ selections, which are summarised in Table 4.4.

| Baryon | ZDC and $V0$ $percentile$ classes (%) |
|:---:|:---:|
| $\Lambda$ and $\Xi$ | [0-10], [10-20], [20-30],[30-40], [40-50], [50-60], [60-70], [70-80], [80-90], [90-100] |
| $\Omega$ | [0-10], [10-30], [30-50], [50-100] |

Table 4.4: Multiplicity (V0) and effective energy (ZDC) classes used for each particle in this part of the analysis.

Figure 4.17 shows the normalized strange baryons yields in different percentile selections of V0 and ZDC. Both estimators are anticorrelated with the strange particle production as expected, since low percentiles correspond to high multiplicity and effective energy, while, as it was shown, strangeness production increases with multiplicity. The anticorrelation is however much stronger when considering $V0$ $percentile$ (red plot) with respect to $ZDC$ $percentile$ (blue plot). This observation gives already a hint that the strangeness enhancement may be mainly due to a final state effect and may not be influenced by the

effective energy. Even though the blue plot shows a visible, although weak, dependence on the *ZDC percentile*, this observation might be related to the correlation between effective energy and multiplicity, which may play an important role on this trend.
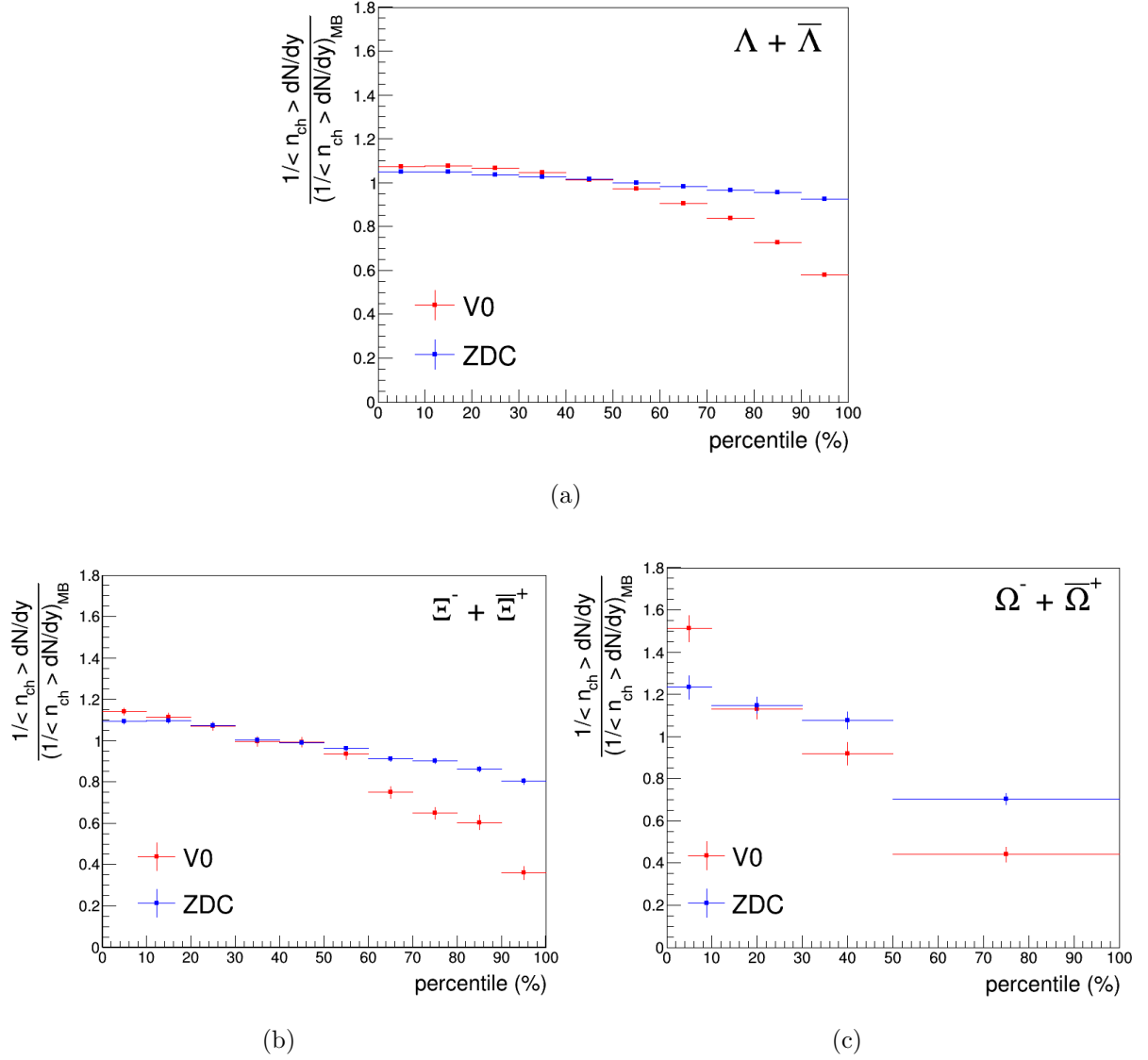


(a)



(b)



(c)

Figure 4.17: $\Lambda$ (a) $\Xi$ (b) and $\Omega$ (c) particle production normalized to MB and $< n_{ch} >$ for different percentile selections in V0 and ZDC. The error displayed are statistical.

In order to perform the double differential analysis proposed, the strange particles production is then analysed in two selected ranges of effective energy (by using the estimator *ZDC percentile*):

- High effective energy and low energy deposit in the ZDC:
  0 % < *ZDC percentile* < 30 %;

- Low effective energy and high energy deposit in the ZDC:
  70 % < *ZDC percentile* < 100 %.

The steps explained in the previous sections are repeated in these energy ranges, obtaining the corrected spectra and the integrated yields normalized to MB.
Then the strangeness production is analysed in two selected ranges of multiplicity (by using the estimator *V0 percentile*):

- High charged-particle multiplicity production:
  0 % < *V0 percentile* < 30 %;

- Low charged-particle multiplicity production:
  70 % < *V0 percentile* < 100 %.

In these multiplicity ranges the corrected spectra are computed and the integrated yields normalized to MB are extracted.

**Effective energy selection**

In both *ZDC percentile* selection regions, the statistics allows to use mostly the same fit ranges and extrapolation regions summarized in Table 4.3 on the corrected spectra. The dependence of strange particle production for $\Lambda + \bar{\Lambda}$, $\Xi^- + \bar{\Xi}^+$ and $\Omega^- + \bar{\Omega}^+$ is shown in different *V0 percentile* classes in Fig. 4.18. As can be inferred from these plots, the selections on effective energy do not have a strong influence on the observed trend. Even when considering the dependence of strangeness production on the mean reference multiplicity, the selections on effective energy do not play an important role in the enhanced trend, as shown in Fig. 4.19. This plot also displays the observed dependence selecting the Minimum Bias range on ZDC (0 % < *ZDC percentile* < 100 %).

(a)



(b)



(c)
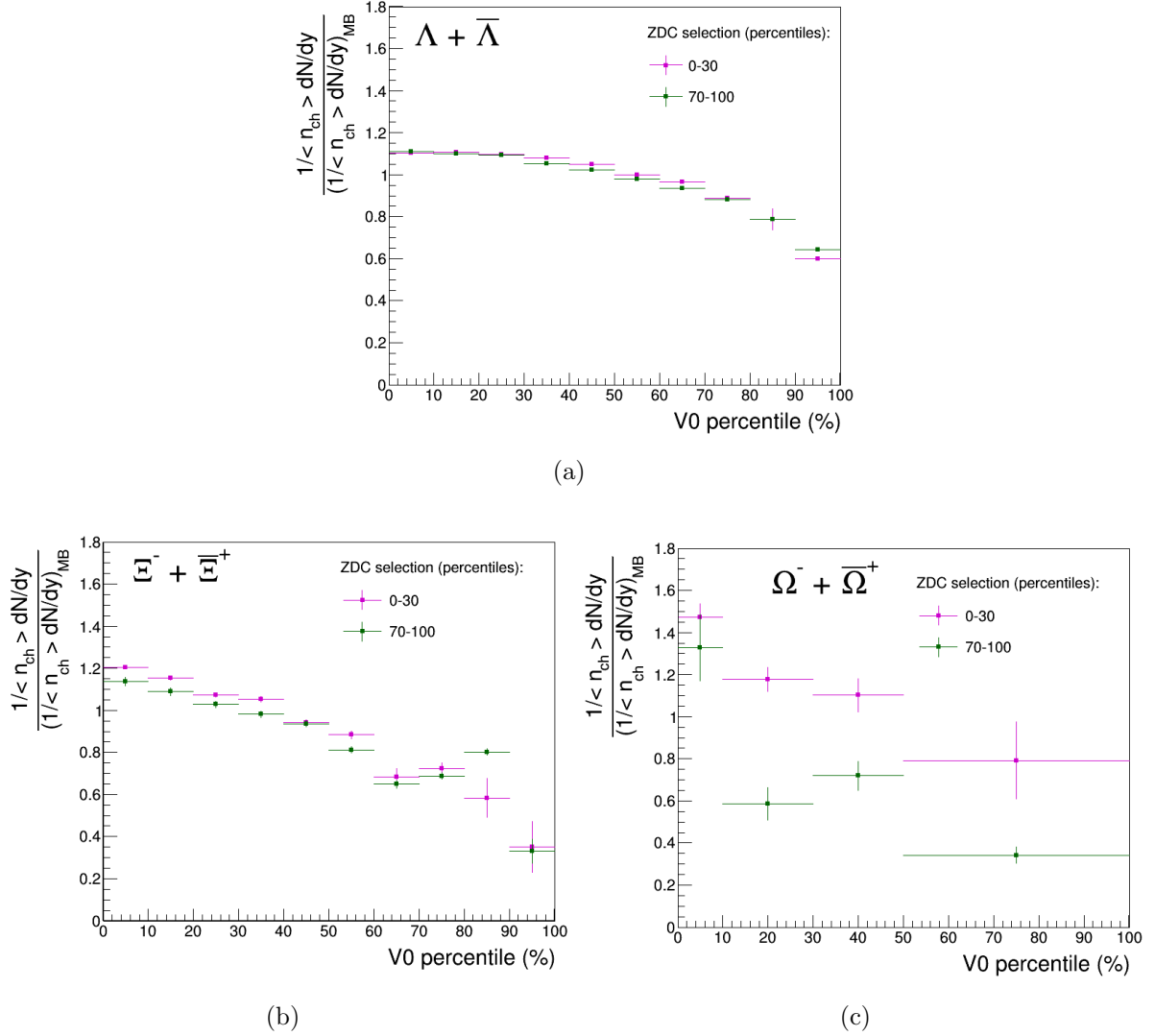
Figure 4.18: $\Lambda$ (a) $\Xi$ (b) and $\Omega$ (c) integrated yields normalized to MB and $< n_{ch} >$ in different $V0$ *percentile* classes for low (green) and high (purple) effective energy selections. The error displayed are statistical.

(a)



(b)



(c)
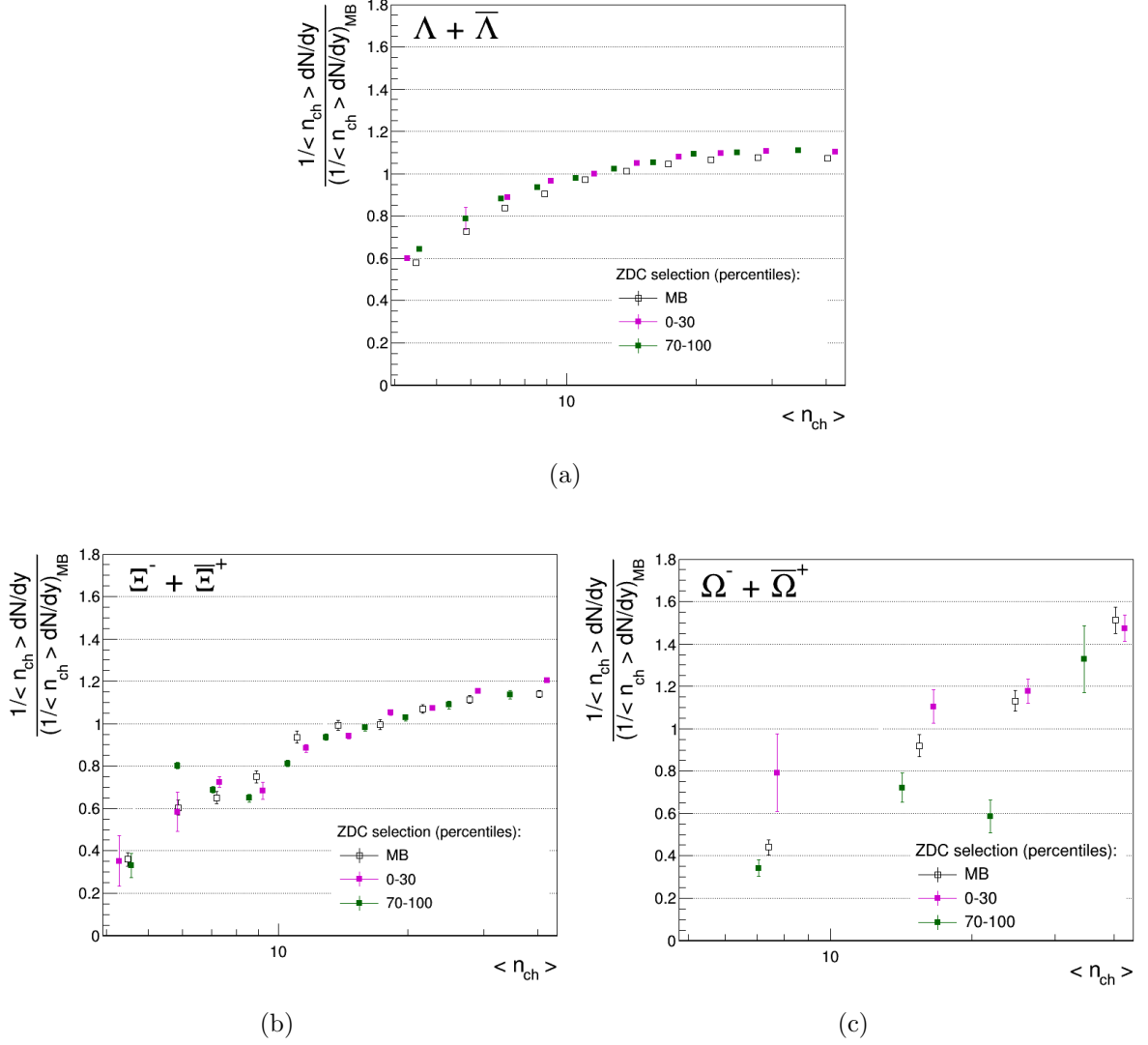
Figure 4.19: $\Lambda$ (a) $\Xi$ (b) and $\Omega$ (c) integrated yields normalized to MB and $< n_{ch} >$ as a function of the reference multiplicity obtained from V0 classes selected spectra, for low (green) and high (purple) effective energy selections. The error displayed are statistical.

87

## Multiplicity selection

The selection on $V0$ *percentile* has a strong influence on the statistics of the corrected spectra, in particular when considering the low multiplicity region. Therefore in this $V0$ *percentile* range [70, 100]%, in order to accomplish the best quality parametrization of the spectra, the fit ranges and the extrapolation regions are modified with respect to the selections in Table 4.3 to the ones in Table 4.5. Moreover the low statistics in this region does not allow to cover all ZDC energy classes for $\Omega$ baryons, but requires a high energy deposit in the ZDC to be visible. Therefore in this section the $\Omega$ candidates are analysed for $ZDC$ *percentile* $> 30$ %. The dependence of strange particles production

| Baryon | Fit range in $p_{\mathrm{T}}$ (GeV/$c$) | Extrapolation range (GeV/$c$) |
|:------:|:---------------------------------------:|:-----------------------------:|
| $\Lambda$ | [0.7 - 10.0] | $p_{\mathrm{T}} > 10.0$, $p_{\mathrm{T}} < 0.7$ |
| $\Xi$ | [0.9 - 5.0] | $p_{\mathrm{T}} > 5.0$, $p_{\mathrm{T}} < 0.9$ |
| $\Omega$ | [1.0 - 4.0] | $p_{\mathrm{T}} > 4.0$, $p_{\mathrm{T}} < 1.0$ |

Table 4.5: Fit range and extrapolation range for the corrected particle spectra selected in the low multiplicity region ($V0$ *percentile* range [70, 100]%).

for $\Lambda + \bar{\Lambda}$, $\Xi^- + \bar{\Xi}^+$ and $\Omega^- + \bar{\Omega}^+$ normalized to MB and $< n_{ch} >$ on $ZDC$ *percentile* is shown in the selected multiplicity ranges in Fig. 4.20. As can be inferred from these plots, the dependence of strangeness production on the $ZDC$ *percentile* ranges is weak, but the selection on V0 produces a shift reaching higher particle yields for higher multiplicities. These observations show that the effect of multiplicity in strange particle production is predominant and has a strong influence on the trend. Even when considering the dependence of strangeness production on the reference multiplicity, it is clear that the selection on $V0$ *percentile* plays a crucial role in the enhanced trend, as shown in Fig. 4.21. In the high multiplicity selection region the purple points show an increasing trend, while in the low multiplicity region the green points show no correlation with $< n_{ch} >$. This observation is a consequence of the correlation between effective energy and multiplicity shown in Fig. 4.3, the latter responsible for the enhancement at high multiplicities (purple region). At lower multiplicity selections, the effect of the correlation is weaker and the enhanced trend disappears. All these observations are in agreement with the conclusion that the strangeness enhancement visible in pp interactions is related to a final state effect. Considering the effective energy correlation with the final charged particle

multiplicity produced in the event, the observed increased strangeness production as a function of the available energy can be expected.



(a)



(b)                                                    (c)
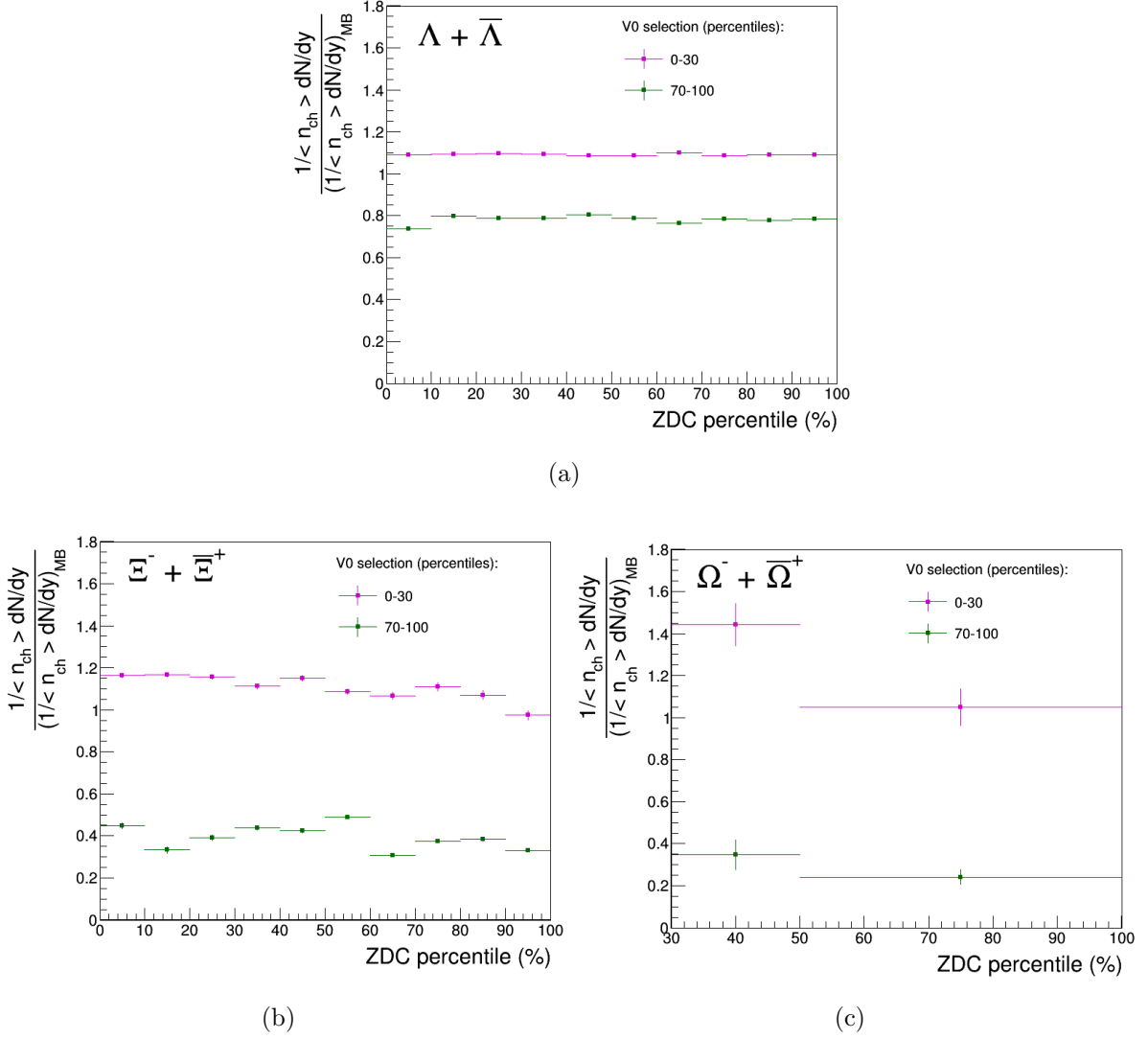
Figure 4.20: $\Lambda$ (a) $\Xi$ (b) and $\Omega$ (c) integrated yields normalized to MB and $< n_{ch} >$ in different *ZDC percentile* classes for low (green) and high (purple) multiplicity selections. The error displayed are statistical.

(a)



(b)



(c)
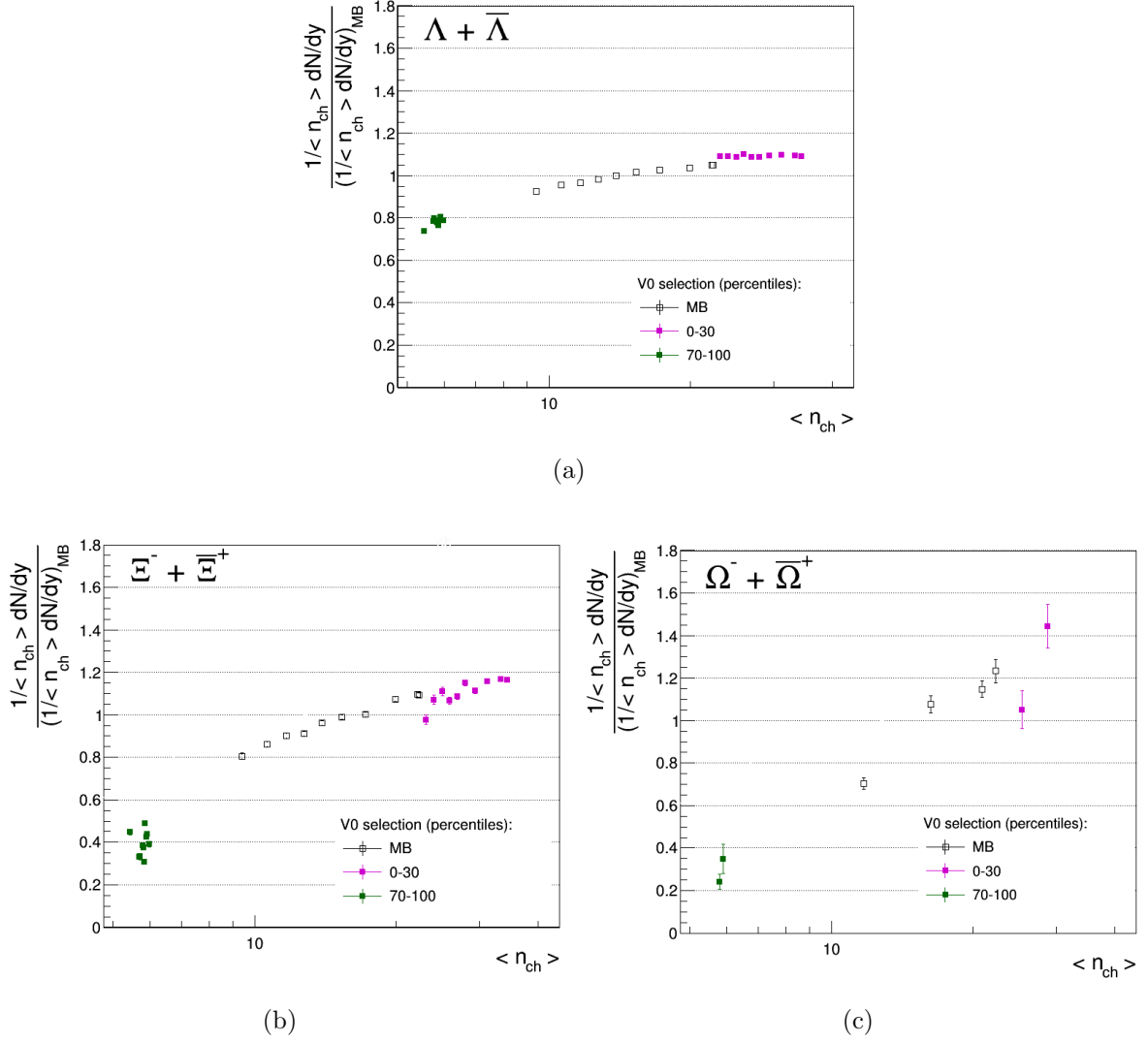
Figure 4.21: $\Lambda$ (a) $\Xi$ (b) and $\Omega$ (c) integrated yields normalized to MB and $< n_{ch} >$ as a function of the reference multiplicity obtained from ZDC classes selected spectra, for low (green) and high (purple) multiplicity selections. The error displayed are statistical.

# Conclusions

The purpose of this thesis is to better understand the particle production mechanisms involved in pp collisions, which are ruled by QCD in the non-perturbative regime. In particular, this study focuses on strangeness production in pp collisions at $\sqrt{s} = 13$ TeV as a function of the effective energy available in the initial phase of the interaction and of the charged multiplicity produced in the final state. This thesis introduced for the first time in the ALICE environment a new variable which allows to estimate the energy available for particle production in each event. This was done by exploiting the ability of ALICE Zero Degree Calorimeters to cover the most forward rapidity particles, candidates for leading baryons.

Through this energy estimator it was possible to explore for the first time the dependence of strange particles production on the effective energy, showing an enhanced trend in particular when increasing the strangeness content in baryon composition.

Moreover this analysis allowed to extend the multiplicity regions in the search of strangeness enhancement in pp collisions, by selecting an increased center of mass energy of the interactions analysed from $\sqrt{s} = 7$ TeV to $\sqrt{s} = 13$ TeV. The dependence of the observed phenomenon on multiplicity, studied in this thesis, confirms that the enhanced trend continues even at higher multiplicities, being mostly compatible with the previous results in the respective multiplicity regions. For $\Lambda$ and $\bar{\Lambda}$ hadrons the enhancement shows a slowdown at high multiplicities, the understanding of this observation might be more clear after taking into account systematics and possible pile-up effects.

Once established the dependence of the observed phenomenon with multiplicity and effective energy, through a double differential study this thesis allowed to conclude that the strangeness enhancement visible in pp interactions is related to a final state effect. Considering the effective energy correlation with the final charged particle multiplicity produced in the event, the observed increased strangeness production as a function of the available energy can be expected.

# Appendices

# Appendix A

# Topological Selections on V0s and Cascades

Table A.1 and A.2 summarize the restrictions on the topology of V0s and Cascades decays chosen to select candidates in this analysis, together with few more general selections on rapidity and psudorapidity. Besides these selection cuts, a set of track quality requirements on the TPC detector is applied, in order to ensure that only high-quality candidates are selected.

| V0s | |
|---|---|
| **Topological variable** | **Cut** |
| V0 transv. decay radius | $> 0.50$ cm |
| DCA Negative Track to PV | $> 0.06$ cm |
| DCA Positive Track to PV | $> 0.06$ cm |
| V0 Cosine of Pointing Angle | $> 0.995$ |
| DCA V0 Daughters | $< 1.0\ \sigma$ |
| **Other selections** | **Cut** |
| Rapidity Interval $|y|$ | $< 0.5$ |
| Daughter Track Pseudorapidity Interval $|\eta|$ | $< 0.8$ |

Table A.1: Selections applied to $\Lambda$ and $\bar{\Lambda}$ candidates.

| Cascades | |
| --- | --- |
| **Topological variable** | **Cut $\Xi$ ($\Omega$)** |
| Cascade transv. decay radius $R_{2D}$ | $> 0.6$ (0.5) cm |
| V0 transv. decay radius | $> 1.2$ (1.1) cm |
| DCA bachelor - PV | $> 0.04$ cm |
| DCA V0 - PV | $> 0.06$ cm |
| DCA meson V0 track - PV | $> 0.04$ cm |
| DCA baryon V0 track - PV | $> 0.03$ cm |
| DCA V0 tracks | $< 1.5$ $\sigma$ |
| DCA bach - V0 | $< 1.3$ cm |
| cascade $\cos(\theta_{pointing})$ | $> 0.97$ |
| V0 $\cos(\theta_{pointing})$ | $> 0.97$ |
| **Other selections** | **Cut** |
| Rapidity Interval $|y|$ | $< 0.5$ |
| Daughter Track Pseudorapidity Interval $|\eta|$ | $< 0.8$ |

Table A.2: Selections applied to $\Xi$, $\bar{\Xi}$, $\Omega$ and $\bar{\Omega}$ candidates.

# Bibliography

[1] ALICE Collaboration, *Nature Phys.* 13 (2017) 535-539.

[2] S. Bethke. *Experimental Tests of Asymptotic Freedom*. Max-Planck-Institut für Physik, Munich, Germany. February 5, 2008.

[3] Volker Koch (LBL Berkeley), *Introduction to Chiral Symmetry*, Dec 1995, 52 pp. arXiv:nucl-th/9512029.

[4] K.G. Wilson, *Phys. Rev.* D 10, (1974) 2445.

[5] Kohsuke Yagi, Tetsuo Hatsuda and Yasuo Miake, *Quark-Gluon Plasma: From Big Bang to Little Bang*, Cambridge University Press, 2005.

[6] ALICE Collaboration. *Phys. Rev.* C 88 (2013) 044909.

[7] M. Miller, K. Reygers, S. J. Sanders, and P. Steinberg, *Ann. Rev. Nucl. Part. Sci.* 57, 205 (2007), arXiv:nucl-ex/0701025.

[8] C. Gale, S. Jeon, and B. Schenke, *Int. J. Mod. Phys* A28, 1340011 (2013).

[9] G. Aad et al. (ATLAS Collaboration), *Phys. Lett.* B 710, 363 (2012).

[10] S. Chatrchyan et al. (CMS Collaboration), *J. High Energy Phys.* 08 (2011) 141.

[11] I. G. Bearden et al. (BRAHMS Collaboration), *Phys. Rev. Lett.* 88, 202301 (2002).

[12] ALICE Collaboration, *Phys. Rev. Lett.* 116, (2016), 222302.

[13] ALICE Collaboration, *JHEP* 1811 (2018) 013.

[14] ALICE, J. Adam et al., *Phys. Rev. Lett.* 116, (2016) 132302.

[15] J. Rafelski and B. Müller. *Physical Review Letters* 48, (1982) p.1066-1069.

[16] Domenico Colella. *Study of multi-strange baryon production with ALICE at the LHC energies.*. PhD thesis, Università degli Studi di Bari "Aldo Moro", 2014.

[17] Antinori F. et al. (NA57 Colaboration), *J. Phys.* G 32, 427-441 (2006).

[18] Abelev B. et al. (STAR Colaboration), *Phys. Rev.* C 77, 044908 (2008).

[19] O. S. Broning et al., *LHC Design Report*, (2004).

[20] Michal Šefčík, for the ALICE Collaboration *EPJ Web of Conferences* 171, 13007 (2018).

[21] A.Zichichi, *Multiparticle hadronic systems produced in high-energy (pp) interactions, and comparison with ($e^+e^-$).* Proceedings of the EPS International Conference on "High-Energy Physics", Lisbon, Portugal, 9-15 July 1981 (EPS, Geneva, 1982), 1133.

[22] E. Barate et al. (ALEPH), *Phys. Rep.* 294, 1 (1998).

[23] P. Abreu et al. (DELPHI), *Eur. Phys. J.* C6, 19 (1999).

[24] B. Adeva et al. (L3), *Phys. Lett.* B259, 199 (1991).

[25] G. S. Abrams et al. (MARK-II), *Phys. Rev. Lett.* 64, 1334 (1990).

[26] D. Buskulic et al. (ALEPH), *Z. Phys.* C73, 409 (1997).

[27] R. Akers et al. (OPAL), *Z. Phys.* C72, 191 (1996).

[28] K. Akerstaff et al. (OPAL), *Z. Phys.* C75, 193 (1997).

[29] G. Abbiendi et al. (OPAL), *Eur. Phys. J.* C16, 185 (2000).

[30] Yuri E. Zamora Garcia., *The Production of Leading Protons at HERA. A measurement of its properties using the LPS of ZEUS.* PhD Thesis, University of Geneva, 1999.

[31] J. Benecke, *Nucl. Phys.* B76, 29 (1976).

[32] W. M. Morse, *Phys. Rev.* D15, 66 (1977).

[33] A. Breakstone, *Phys. Rev.* D30, 528 (1984).

[34] G. J. Alner et al. (UA5), *Phys. Lett.* B167, 476 (1986).

[35] R. E. Ansorge et al. (UA5), *Z. Phys.* C43, 357 (1989).

[36] M. Basile et al., *Phys. Lett.* B 92 (1980) 367.

[37] M. Basile et al., *Phys. Lett.* B 95 (1980) 311.

[38] M. Basile et al., *Nuovo Cim.* A 67 (1982) 244.

[39] M. Basile et al., *Nuovo Cim.* A 79 (1984) 1.

[40] ALICE Collaboration, *Eur.Phys.* J.C50 (2007) 341-352.

[41] LENA Collaboration, *Z. Phys.* C9 (1981) 1.

[42] CLEO Collaboration, *Phys. Rev. Lett.* 49 (1982) 357.

[43] JADE Collaboration, *Z. Phys.* C20 (1983) 187.

[44] G. S. Abrams et al., *Phys. Rev. Lett.* 64 (1990) 1334.

[45] M. Derrick et al., *Phys. Rev.* D 34 (1986) 3304.

[46] TPC/Two Gamma Collaboration, *Phys. Lett.* B 184 (1987) 299.

[47] AMY Collaboration, *Phys. Rev.* D 42 (1990) 737.

[48] M. Basile et al., *Nuovo Cim.* 66A N.2 (1981).

[49] M. Basile et al., *Nuovo Cim.* A 73 (1983) 329.

[50] M. Basile et al., *Lett. Nuovo Cim.* 38 (1983) 359.

[51] M. Basile et al., *Phys.Lett.* 92B, 367, (1980).

[52] TASSO Collaboration, *Phys.Lett.* 89B, 418, (1980).

[53] G. Wolf, DESY Report, 80/85 (1980).

[54] M. Basile et al., *Nuovo Cim. Lett.* 31 273 (1981).

[55] A. Zichichi *Il Nuovo Saggiatore* 27 N3-4, 48-56, (2011).

[56] PHOBOS Collaboration, *arXiv:nucl-ex/0301017.*

[57] J. Klay, U.C. Davis PhD. Thesis (2001).

[58] S. V. Afanasiev et al., *Phys. Rev.* C 66, 054902 (2002).

[59] ALICE *Technical Design Report of the Inner Tracking System.* CERN / LHCC 99-12 ALICE TDR 4, 18 June 1999.

[60] ALICE *Technical Design Report of the Time Projection Chamber.* CERN/LHCC 2000-001, ALICE TDR 7, 7 January 2000.

[61] ALICE *Technical Design Report of the Transition Radiation Detector.* CERN / LHCC 2001-021, ALICE TDR 9, 3 October 2001.

[62] ALICE *Technical Design Report of the Transition Radiation Detector*. CERN / LHCC 2000-12 ALICE TDR 8, 16 February 2000.

[63] F. Carnesecchi (on behalf of the ALICE Collaboration), *Performance of the ALICE Time-Of-Flight detector at the LHC*, arXiv:1806.03825 [physics.ins-det].

[64] P. Crochet for the ALICE collaboration. *The ALICE Forward Muon Spectrometer*. ALICE-PUB-2001-58 version 1.0 2001-12-13.

[65] ALICE *Technical Design Report on Forward Detectors: FMD, T0 and V0*. CERN-LHCC-2004-025 ALICE-TDR-011, 10 September 2004.

[66] ALICE Collaboration. *Centrality determination in heavy ion collisions*. ALICE-PUBLIC-2018-011.

[67] Anticic et al., *Phys. Rev.* C 86, 054903 (2012).

[68] R. Albrecht et al., *Phys. Rev. Lett.* 76 (1996) 3506.

[69] M.C. Abreu et al. (NA50 Collaboration), *Phys. Lett.* B410 (1997) 327.

[70] ALICE *Technical Design Report of the Zero Degree Calorimeter (ZDC)*. CERN / LHCC 99–5, ALICE TDR 3, 5 March 1999.

[71] ALICE Collaboration 2006 ALICE: Physics Performance Report, Volume II *J. Phys. G: Nucl. Part. Phys.* 32 1295–2040.

[72] M. Tanabashi et al. (Particle Data Group), *Phys. Rev.* D 98, 030001 (2018).

[73] ALICE Collaboration, *Eur. Phys. J.* C 71 (2011) 1594. DOI:10.1140/epjc/s10052-011-1594-5

[74] ALICE Collaboration, *Phys. Lett.* B 712 (2012) 309. DOI:10.1016/j.physletb.2012.05.011